Excitons in Strongly Confined Halide Perovskite Nanoplatelets

Moritz Gramlich

München, 2022

Exzitonen in stark beschränkten Halid-Perowskit Nanoplättchen

Dissertation

zur Erlangung des Doktorgrades der Naturwissenschaften (Dr. rer. nat.)

an der Fakultät für Physik

der Ludwig-Maximilians-Universität München

vorgelegt von

Moritz Gramlich

aus Dachau

München, 22. April 2022

Promotionskommission

Erstgutachter:	Prof. Dr. Alexander Urban
Zweitgutachter:	Prof. Dr. Alexander Högele
Vorsitzender:	Prof. Dr. Dieter Braun
Beisitzer:	Prof. Dr. Jan von Delft
Tag der mündlichen Prüfung:	03. Juni 2022

dedicated to my parents

Publications and Conferences

Scientific Publications of Results Presented in This Work

- M. Gramlich, M. W. Swift, C. Lampe, J. L. Lyons, M. Döblinger, A. L. Efros, P. C. Sercel, A. S. Urban
  Dark and Bright Excitons in Halide Perovskite Nanoplatelets
  Advanced Science 9(5): 2103013 (2022)

- M. Gramlich, C. Lampe, J. Drewniok, A. S. Urban
  How Exciton–Phonon Coupling Impacts Photoluminescence in Halide Perovskite Nanoplatelets
  The Journal of Physical Chemistry Letters 12(46): 11371-11377 (2021)

- M. Gramlich, B. J. Bohn, Y. Tong, L. Polavarapu, J. Feldmann, A. S. Urban
  Thickness-Dependence of Exciton–Exciton Annihilation in Halide Perovskite Nanoplatelets
  The Journal of Physical Chemistry Letters 11(13): 5361-5366 (2020)

- A. Singldinger, M. Gramlich, C. Gruber, C. Lampe, A. S. Urban
  Nonradiative Energy Transfer between Thickness-Controlled Halide Perovskite Nanoplatelets
  ACS Energy Letters 5(5): 1380-1385 (2020)

Additional Publications

- S. Wang, M. Dyksik, C. Lampe, M. Gramlich, D. K. Maude, M. Baranowski, A. S. Urban, P. Plochocka, A. Surrente
  Thickness-Dependent Dark-Bright Exciton Splitting in $CsPbBr_3$-based Nanoplatelets Revealed via Magneto-Optical Spectroscopy
  Nano Letters submitted (2022)

- Q. Xue, C. Lampe, T. Naujoks, K. Franke, M. Gramlich, M. Schoger, W. Vanderlinden, P. Reisbeck, B. Nickel, W. Brütting, A. S. Urban
  Doubly Stabilized Perovskite Nanocrystal Luminescence Downconverters
  Advanced Optical Materials accepted (2022)

- K. Bramhaiah, R. Bhuyan, S. Mandal, S. Kar, R. Prabhu, N. S. John, M. Gramlich, A. S. Urban, S. Bhattacharyya
  Molecular, Aromatic, and Amorphous Domains of N-Carbon Dots: Leading toward the Competitive Photoluminescence and Photocatalytic Properties
  The Journal of Physical Chemistry C 125(7): 4299-4309 (2021)

- V. A. Hintermayr, C. Lampe, M. Löw, J. Roemer, W. Vanderlinden, M.Gramlich, A. X. Böhm, C. Sattler, B. Nickel, T. Lohmüller, A. S. Urban
  Polymer Nanoreactors Shield Perovskite Nanocrystals from Degradation
  Nano Letters 19(8): 4928-4933 (2019)

- B. J. Bohn, T. Simon, M. Gramlich, A. F. Richter, L. Polavarapu, A. S. Urban, J. Feldmann
  Dephasing and Quantum Beating of Excitons in Methylammonium Lead Iodide Perovskite Nanoplatelets
  ACS Photonics 5(2): 648-654 (2018)

- B. J. Bohn, Y. Tong, M. Gramlich, M. L. Lai, M. Döblinger, K. Wang, R. L. Z. Hoye, P. Müller-Buschbaum, S. D. Stranks, A. S. Urban, L. Polavarapu, J. Feldmann
  Boosting Tunable Blue Luminescence of Halide Perovskite Nanoplatelets through Postsynthetic Surface Trap Repair
  Nano Letters 18(8): 5231-5238 (2018)

Contributions to Conferences and Workshops

- *AMOLF-LMU Workshop* (Talk)
  Munich, Germany, November 2021
- *QD2020 (Quantum Dot) Conference* (Poster)
  Munich/Online, Germany, December 2020
- *8th International SolTech Conference* (Poster)
  Nuremberg, Germany, October 2019
- *e-conversion Kickoff Conference* (Poster)
  Venice, Italy, September 2019
- *MRS Fall Meeting* (Talk)
  Boston, USA, November 2018
- *7th International SolTech Conference* (Poster)
  Würzburg, Germany, October 2018
- *34th International Conference on the Physics of Semiconductors: ICPS 2018* (Poster)
  Montpellier, France, August 2018

Zusammenfassung

Kolloidale Halbleiter-Nanokristalle und insbesondere ihre von der Kristallgröße abhängigen Eigenschaften werden seit den frühen 1980er Jahren untersucht. In jüngster Zeit haben sich zu den zahlreichen Zusammensetzungen und Formen, die mittlerweile existieren, auch Bleihalogenid-Perowskit Nanoplättchen gesellt, die aufgrund einer kostengünstigen und unaufwendigen Synthese und der daraus resultierenden hohen Photolumineszenz-Quantenausbeute im blauen Spektralbereich viel Aufmerksamkeit auf sich ziehen. Die präzise Variation der Nanoplättchen-Dicke bei der Synthese ermöglicht nicht nur den Gebrauch in optoelektronischen Anwendungen, sondern auch die sehr genaue Untersuchung des Einflusses der starken Quantenbeschränkung auf zahlreiche Halbleitereigenschaften. Eine der Eigenschaften, die sich aus der Quantenbeschränkung ergibt, ist eine deutlich erhöhte Exzitonen-Bindungsenergie. Exzitonen, also gebundene Elektron-Loch-Paare, dominieren daher das Emissionsverhalten von Bleihalogenid-Perowskit Nanoplättchen und stehen im Mittelpunkt dieser Arbeit. Einblicke in ihre Eigenschaften und ihr Verhalten werden durch verschiedene spektroskopische Techniken bei Temperaturen bis zu 5 K sowie durch zeitaufgelöste Messungen der Exzitonenpopulation ermöglicht.

Zuerst wird die Feinstruktur der exzitonischen Zustände in den Nanoplättchen bestimmt, deren energetisch niedrigster Exzitonzustand einen dunklen oder optisch inaktiven Zustand darstellt. Um den energetischen Abstand dieses Niveaus zu den drei hellen Zuständen darüber zu beschreiben, wird ein neues theoretisches Modell entwickelt, das auch auf andere anisotrop geformte Nanokristalle übertragbar ist. In Experiment und Modell wird eine zunehmende energetische Aufspaltung mit abnehmender Dicke festgestellt, die in den dünnsten Nanoplättchen eine Hell-Dunkel-Aufspaltung von 32.3 meV erreicht und somit den größten Wert darstellt, der bisher in einem Halbleiter-Nanokristall beobachtet wurde. Zweitens wird die Dickenabhängigkeit der Exziton-Phonon-Wechselwirkung untersucht und ein abweichendes Verhalten der dünnsten Nanoplättchen beobachtet, das wahrscheinlich mit der zuvor untersuchten Exzitonen-Feinstruktur zusammenhängt. Drittens wird die Exziton-Exziton-Wechselwirkung, die in diesem System zu einer schnellen Exziton-Exziton-Annihilation führt, quantifiziert. Hier wird festgestellt, dass die 1/e-Lebensdauer von zwei Exzitonen in einem Nanoplättchen einem Potenzgesetz in Bezug auf die Nanoplättchen-Dicke d folgt, also $\tau_2 \propto d^{5.3}$. Schließlich wird noch die Wechselwirkung zwischen verschiedenen Nanoplättchen betrachtet und die Effizienz des Exzitonentransfers von einem dünneren auf ein dickeres Nanoplättchen gemessen. Der Prozess geschieht über Förster-Resonanzenergietransfer und erreicht bis zu 69 % Effizienz.

Alle Ergebnisse dieser Arbeit zusammengenommen stellen einen Beitrag zur Entschlüsselung der Mechanismen dar, die den größen- und materialabhängigen Eigenschaften von Halbleiter-Nanokristallen zugrunde liegen. Damit können diese Erkenntnisse nicht nur zur Verbesserung der Bleihalogenid-Perowskit Nanoplättchen im Speziellen, sondern auch bei der Suche nach weiteren vielversprechenden Nanokristallsystemen berücksichtigt werden.

Abstract

Colloidal semiconductor nanocrystals and in particular their size-dependent properties have been investigated since the early 1980s. Recently, lead halide perovskite (LHP) nanoplatelets (NPLs) have joined the vast amount of compositions and shapes existing by now and attracted attention due to their cheap and easy synthesis resulting in high photoluminescence quantum yields in the blue spectral range. Besides their potential towards optoelectronic application, their precise thickness tunability enables in-depth investigations of the effects of strong quantum confinement in one dimension on numerous semiconductor properties. One of the properties resulting from the confinement is a substantially increased exciton binding energy. Thus, excitons, i.e., bound electron-hole pairs dominate the emissive behavior of LHP NPLs and are in the focus of this thesis. Insights into their properties and behavior are mainly gained through various spectroscopic techniques at temperatures down to 5 K as well as time-resolved measurements of the excitonic population.

First, the fine structure of the excitonic states inherent to the NPLs is determined to posses a lowest dark or optically inactive level below three bright levels. To describe the energetic splitting of these levels, a novel theoretical model is developed, which is also applicable to other anisotropically shaped nanocrystals. In experiment and model an increasing energetic splitting with decreasing thickness is observed, which reaches a dark-bright splitting of 32.3 meV in the thinnest NPLs, the largest value observed to date in a semiconductor nanocrystal. Second, the thickness dependence of exciton-phonon interaction is examined and a diverging behavior of the thinnest NPLs is detected, which is likely connected to the exciton fine structure explored before. Third, the exciton-exciton interaction, which results in fast exciton-exciton annihilation in this system, is quantified and the 1/e lifetime of two excitons in one NPL is found to obey a power law in terms of the NPL thickness d, i.e. $\tau_2 \propto d^{5.3}$. Lastly, the interaction between different NPLs is taken under consideration and the efficiency of the exciton transfer from a thinner to a thicker NPL via Förster resonance energy transfer is found to reach 69 %.

All results of this thesis combined represent a contribution to unraveling the mechanisms governing the size- and material-dependent properties of semiconductor nanocrystals. Thus, these findings can be taken into account not only for improving the LHP NPLs in particular but also in the search for further promising nanocrystal systems.

Table of Contents

Zusammenfassung vii

Abstract ix

1 Introduction 1

2 Fundamentals 3

2.1 Semiconductors and Excitons . . . 4

2.1.1 The Electronic Structure of Crystalline Solids . . . 4

2.1.2 Semiconductors . . . 6

2.1.3 Excitons . . . 7

2.1.4 Trions and Biexcitons . . . 9

2.1.5 Confined Semiconductors . . . 9

2.2 Interband Transitions . . . 13

2.2.1 Optical Excitation . . . 13

2.2.2 Radiative Recombination . . . 15

2.2.3 Non-Radiative Recombination . . . 17

2.2.4 Exciton-Exciton Annihilation . . . 19

2.2.5 Broadening of Optical Transitions . . . 21

2.3 Energy Transfer . . . 23

2.4 Lead Halide Perovskite Nanocrystals . . . 24

2.4.1 Lead Halide Perovskites . . . 24

2.4.2 Lead Halide Perovskite Nanoplatelets . . . 27

3 Materials and Methods 33

3.1 Nanocrystal Synthesis and Characterization . . . 34

3.1.1 $CsPbBr_3$ Nanoplatelets . . . 34

3.1.2 $CsPbBr_3$ Nanocubes . . . 35

3.1.3 Film Formation . . . 35

3.1.4 Electron Microscopy . . . 35
3.1.5 Optical Characterization . . . 37
3.2 Temperature-Dependent Photoluminescence . . . 39
3.2.1 Excitation Source . . . 39
3.2.2 Steady-State Photoluminescence . . . 40
3.2.3 Time-Resolved Photoluminescence . . . 42
3.3 Transient Absorption Spectroscopy . . . 44

4 Exciton Fine Structure 47
4.1 Temperature-Dependent Photoluminescence . . . 48
4.2 2D Exciton in Perovskite Nanoplatelets . . . 51
4.3 Spectroscopically Determined Bright-Dark Splitting . . . 53
4.4 Exciton Lifetimes . . . 58
4.5 Summary and Discussion . . . 66

5 Exciton-Phonon Coupling 69
5.1 Temperature Influence on Photoluminescence . . . 70
5.2 Temperature-Dependent Linewidth . . . 72
5.3 Temperature-Dependent Photoluminescence Peak Position . . . 74
5.4 Summary and Discussion . . . 78

6 Exciton-Exciton Annihilation 79
6.1 Differential Transmission Spectra . . . 80
6.2 Determination of Initial Exciton Density . . . 81
6.3 Exciton-Exciton Annihilation Lifetime . . . 85
6.4 Summary and Discussion . . . 88

7 Energy Transfer 89
7.1 Mixing of Dispersions . . . 90
7.2 Donor-Acceptor Heterolayers . . . 93
7.3 Summary and Discussion . . . 96

8 Conclusion and Outlook 99

References I

List of Figures VII

List of Tables **IX**

List of Abbreviations **XI**

Acknowledgments **XIII**

1

Introduction

Semiconductor structures with a size on the nanometer scale are at the forefront of technological advance in the past decades. Mainly driven by decreasing transistor size, which enables increased computing power on a small microprocessor, more and more elaborate techniques have been established already resulting in semiconductor structures of a few nanometers. Besides such top-down fabrication techniques, however, solution-based syntheses yielding semiconductor nanocrystals with a diameter of only a few nanometers have already emerged in the 1980s.[1–3] While the application of such colloidal nanocrystals (often referred to as quantum dots) had been limited to fluorescent labeling in the biological or biomedical sector for a long time, they have found their way into lighting and display applications in the past ten years - the most notable technology being so-called quantum-dot TVs.[4]

A comparably new player in the field of colloidal semiconductor nanocrystals are lead halide perovskite (LHP) nanocrystals. In 2009 the first working solar cell based on LHP in its bulk morphology was reported, which sparked interest in the material and its optoelectronic potential.[5] In the following years record efficiencies of perovskite solar cells quickly surpassed one another and research interest grew rapidly.[6] As the term perovkite is loosely applied to all materials crystallizing in the so-called perovskite structure, research quickly spread to different perovskite compositions and in 2015 the first synthesis yielding colloidal LHP nanocrystals was reported.[7] These nanocrystals received considerable attention due to their exceptionally high photoluminescence quantum yields approaching unity. Since these high quantum yields were exclusive to the red and green ranges of the visible spectrum, however, the need for an efficient blue LHP-based light emitter lead to the development of LHP nanoplatelets (NPLs).[8–10] Through strong quantum confinement in one dimension the NPLs are able to blue-shift the otherwise green emission of the perovkite $CsPbBr_3$ incrementally by reducing the number of crystal layers to a wavelength of 432 nm reached for two layers of unit cells.

On the one hand, those LHP NPLs are an interesting candidate for efficient blue light emission, provided their stability can be improved. On the other hand and equally as important, however, their precise thickness tunability on the order of atomic crystal layers allows for fundamental research on the influence of quantum confinement on many semiconductor properties. Although a significant amount

of research has already advanced our understanding of semiconductor nanocrystals since the 1980s, a large portion of those studies focused on spherical or cubic nanocrystals of II-VI or III-V compound semiconductors. To further unravel the fundamental physics on these length scales, detailed studies on anisotropically confined nanocrystals of new semiconductor classes are, thus, of interest.

Against this background, the following chapters investigate some of the fundamental optoelectronic properties of LHP NPLs. More specifically, excitons, the main source of light emission from these NPLs, are investigated in depth with a focus on how a reduction of the NPL thickness affects them. First, however, the theoretical background concerning semiconductors and excitons as well as their interaction with light in general and LHPs in particular are intoduced in Chapter 2. Furthermore, the different spectroscopic methods employed throughout the thesis are covered in Chapter 3.

The findings presented in this work are divided into four chapters, the results of which have each also been published in four different articles. The first of those, Chapter 4, concerns the exciton fine structure of the LHP NPLs. The experimental results on this property are combined with a theoretical model contributed by Alexander L. Efros, who is one of the pioneers in the field of quantum dots and was the first to describe them theoretically in 1982.[3] Upon this fundamental characterization of the excitonic states, the interaction of those excitons with the crystal lattice, i.e., phonons is quantified in Chapter 5. Then, multiple excitons in one NPL are considered and exciton-exciton annihilation in this system is analyzed in Chapter 6. Finally, the last results chapter, Chapter 7, looks towards possible applications of the LHP NPLs and studies the exciton transfer between neighboring NPLs of different band gaps via Förster resonance energy transfer (FRET).

The thesis concludes with a summary of the findings and an outlook on the future of LHP NPLs in particular and semiconductor nanocrystals in general.

2

Fundamentals

All results presented in this thesis revolve around excitons and their interactions in semiconductors, or more specifically, excitons in lead halide perovskite nanocrystals. Accordingly, this chapter first introduces the theory behind semiconductors and excitons in general. In particular, the concept of quantum confinement, which is fundamental to the properties of nanocrystals, is established. Second, the interactions of excitons with light, lattice vibrations, and other excitons are discussed. Third, energy transfer between nanocrystals is briefly introduced, since this mechanism is highly relevant in part of the results. Fourth, some background on the current research concerning lead halide perovskite nanocrystals is presented, which in combination with the theoretical background constitutes the foundation on which the research in this thesis is based.

2.1 Semiconductors and Excitons

Lead halide perovskites belong to the material class of crystalline semiconductors. Thus, starting from the broad topic of crystalline solids and their electronic properties, this section covers the theory behind semiconductors and the role of electrons and holes as fundamental excitations in this material class. The theoretical background given here on crystals in general and semiconductors in particular is far from exhaustive, as this would go beyond the scope of this thesis, and instead focuses on the most important concepts for the following chapters. These concepts include the effect of quantum confinement and its impact on some important semiconductor properties highly relevant for nanocrystals.

2.1.1 The Electronic Structure of Crystalline Solids

The theory behind crystalline solids acts in large parts as a connection between their macroscopic properties, like electrical or thermal conductivity, and their microscopic properties. Importantly, the microscopic structure is also the defining property of a crystal: The building blocks, namely the atoms (or molecules in some cases), arrange highly ordered and periodically on this scale, leading to translational symmetries along specified axes. The smallest possible volume, which spans the whole crystal without voids or overlaps when translated by all possible vectors described by $\mathbf{R}$, is a primitive unit cell. Here, the translation operation $\mathbf{R}$ is given by a linear combination ($n_i \in \mathbb{Z}$) of the so-called primitive translation vectors $\mathbf{a}_i$:[11,12]

$$\mathbf{R} = n_1\mathbf{a}_1 + n_2\mathbf{a}_2 + n_3\mathbf{a}_3 \tag{2.1}$$

All points in space described by all possible linear combinations of these vectors are called lattice points. If the translation vectors $\mathbf{a}_i$ are orthogonal, of equal length and every lattice point is only occupied by one atom, the resulting crystal is termed a simple cubic crystal with a 1-atom basis. Figure 2.1 illustrates such a crystal schematically.

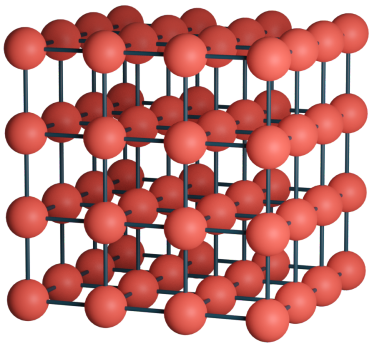

Figure 2.1: Simple Cubic Crystal Lattice. Schematic representation of a simple cubic lattice with one atom at each lattice point. The rods connecting the atoms indicate the primitive translation operations.

In order to describe the electronic structure of a crystal, the one-electron or mean field approximation is applied. In this approximation many body interactions, i.e., electron-electron interactions are neglected and a single electron in a periodic potential is modeled. This leads to independently solvable

eigenvalue problems and simplifies the Schrödinger equation describing an electron in this system drastically:[11,13,14]

$$\left[\frac{\mathbf{p}^2}{2\,m_\mathrm{e}} + V(\mathbf{r})\right]\psi_{\mathrm{n},\mathbf{k}}(\mathbf{r}) = E_\mathrm{n}(\mathbf{k})\,\psi_{\mathrm{n},\mathbf{k}}(\mathbf{r}) \tag{2.2}$$

Here, $\mathbf{p} = -i\hbar\nabla$ represents the momentum operator, m_e the electron mass and $V(\mathbf{r}) = V(\mathbf{r}+\mathbf{R})$ the periodic effective potential induced by the atomic cores. The wave functions $\psi_{\mathrm{n},\mathbf{k}}(\mathbf{r})$ solving this Schrödinger equation are given by Bloch's theorem.[15] These wave functions can be written as a plane wave $e^{i\mathbf{kr}}$ modulated by a periodic function $u_{\mathrm{n},\mathbf{k}}(\mathbf{r})$, which represents the crystal symmetry and, thus, satisfies $u_{\mathrm{n},\mathbf{k}}(\mathbf{r}) = u_{\mathrm{n},\mathbf{k}}(\mathbf{r}+\mathbf{R})$:

$$\psi_{\mathrm{n},\mathbf{k}}(\mathbf{r}) = e^{i\mathbf{kr}} \cdot u_{\mathrm{n},\mathbf{k}}(\mathbf{r}) \tag{2.3}$$

The corresponding energy eigenvalues $E_\mathrm{n}(\mathbf{k})$ in Equation 2.2 connect the energy of an electronic state with its wave vector $\mathbf{k}$ and represent the so-called dispersion relation of an electron in a periodic crystal potential. At this point, the wave vector $\mathbf{k}$ has to be addressed. Simply put, it is a vector in reciprocal space, also called k-space. If a crystal lattice in real space is described by the primitive lattice vectors $\mathbf{a}_i$, a reciprocal lattice in k-space exists, which is described by the primitive reciprocal lattice vectors $\mathbf{b}_i$, and can be obtained by a Fourier transformation of the crystal lattice. Analogously to dividing the real space into primitive unit cells containing only one lattice point, k-space is also subdivided into primitive cells called Brillouin zones. Importantly, the electron wave functions $\psi_{\mathrm{n},\mathbf{k}}(\mathbf{r})$ and corresponding energies $E_n(\mathbf{k})$ remain unchanged when replacing $\mathbf{k}$ by $\mathbf{k}' = \mathbf{k} + \mathbf{G}$ with $\mathbf{G} = m_1\mathbf{b}_1 + m_2\mathbf{b}_2 + m_3\mathbf{b}_3$, which would mean translating $\mathbf{k}$ to the same point in another Brillouin zone. It follows that all states an electron could occupy can be described within the first Brillouin zone.[11,12] Figure 2.2 schematically displays the first Brillouin zone and some high symmetry points, which will be addressed later, for a simple cubic lattice.

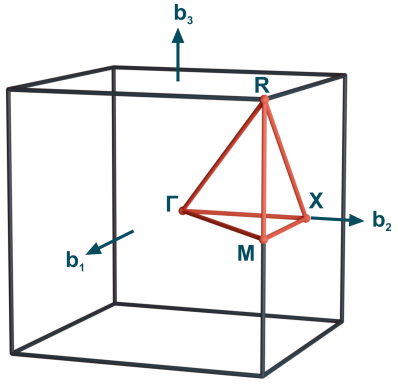

Figure 2.2: First Brillouin Zone. The first Brillouin zone of a simple cubic lattice with its high symmetry points Γ, M, R and X. Adapted from [16].

The electronic dispersion relation $E_\mathrm{n}(\mathbf{k})$ describes the energies of the different electronic states, which exist at a given wave vector $\mathbf{k}$ and labels them with the discrete index n, termed band index. For infinitely large crystals $E_\mathrm{n}(\mathbf{k})$ evolves smoothly with $\mathbf{k}$ for a given n and is therefore called a band and the complete electronic dispersion relation $E_\mathrm{n}(\mathbf{k})$ of a crystal within the first Brillouin zone is defined as the band structure. Illustrating the whole band structure over the first Brillouin zone would

mean plotting $E_n(\mathbf{k})$ for different n against k_x, k_y and k_z, a four-dimensional problem. Therefore, band structures are mostly displayed along a defined path in k-space, which connects different high symmetry points. Lastly, it shall be noted here that if dispersion is neglected and only the energy of all possible states independent of their $\mathbf{k}$ is of interest, the density of states (DOS) can be employed:

$$D(E) = \frac{1}{V} \sum_{n,\mathbf{k}} \delta(E - E_n(\mathbf{k})) \tag{2.4}$$

Then, $D(E)\mathrm{d}E$ returns the number of states in an energetic interval of width $\mathrm{d}E$.[17,18]

2.1.2 Semiconductors

The last section introduced the band structure of crystalline solids. The electronic states defined by this band structure, however, describe all the states an electron can occupy and not all states that are actually occupied. As electrons are fermions and obey the Pauli exclusion principle, each state described by a set of quantum numbers can only be occupied by one electron. At T = 0 K the electrons occupy all states up to an energy E_F, the Fermi energy, and none of the states above. Here, two fundamentally different cases arise: First, E_F can lie within an energetic range covered by a band and, second, E_F can lie in a so-called band gap, an energetic interval in which no electronic states exist. If the former is the case, the material is called a metal, and if the latter is the case, the material is called a semiconductor or an insulator, depending on the energetic width of the band gap. Analogous to valence electrons in atoms, the energetically highest filled band is defined as the valence band (VB), while the energetically lowest empty band is defined as the conduction band (CB). Now, the band gap energy E_G of the semiconductor or insulator can be defined as the difference in energy between the valence band maximum (VBM) and the conduction band minimum (CBM). Whether the VBM and CBM are located at the same point in k-space or not, determines whether the band gap is direct or indirect (see Figure 2.3).[11,12]

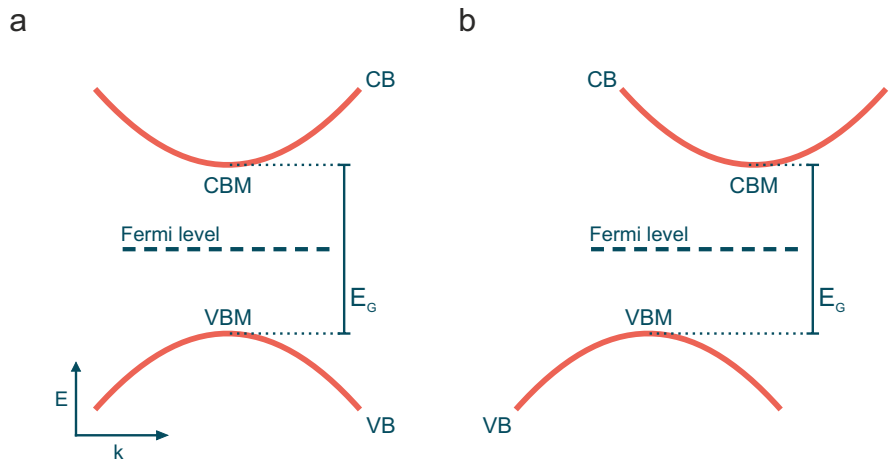

Figure 2.3: Direct and Indirect Band Gap. a) If the VBM and the CBM are located at the same $\mathbf{k}$ value in the Brillouin zone, the band gap is termed direct. **a)** If they are located at different $\mathbf{k}$ values, the band gap is termed indirect.

Thus far, in terms of level occupation only the T = 0 K limit was discussed. Once finite temperatures are considered, thermal energy enables electrons to occupy states above the Fermi level. Their energetic

distribution then deviates from a step function and is described by Fermi-Dirac statistics still obeying the Pauli exclusion principle:[19,20]

$$f(E,T) = \frac{1}{\exp\left(\frac{E-E_F}{k_B T}\right)+1} \tag{2.5}$$

Here, f is the occupation probability at temperature T for a state at an energy E with k_B being the Boltzmann constant. As mentioned above, in metals the Fermi level is located within a band. Thus, this band is only partially filled and responsible for metals being good electrical conductors. Generally speaking, fully filled bands do not contribute to electrical conduction causing semiconductors at T = 0 K to be insulating. In contrast to insulators, however, E_G is small enough in semiconductors that following Equation 2.5 a significant number of electrons overcome the band gap at room temperature, occupy CB states and contribute to electrical conduction. Naturally, this process also leads to unoccupied states in the VB, which is therefore not fully filled anymore. Instead of considering all of the states still occupied by electrons in the VB, however, it is more practical to describe the unoccupied states as electron holes and treat them as positively charged quasi-particles. In undoped semiconductors their number equals the number of electrons in the CBs and they behave similar to these electrons. In particular, they also contribute to electrical conduction.

In the vicinity of energetic extrema the energy bands can be approximated by parabolas, similar to the dispersion relation of a free electron $E(\mathbf{k}) = \frac{\hbar^2\mathbf{k}^2}{2m_e}$, by replacing m_e with an effective electron mass m_e^*. Thus, to describe the behavior of electrons/holes accumulating at the CBM/VBM, their effective masses can be calculated by differentiating the quadratic dispersion relation twice:[11,21]

$$\frac{1}{m_{e/h}^*} = \frac{1}{\hbar^2}\left|\frac{d^2 E_{CB/VB}(\mathbf{k})}{d\mathbf{k}^2}\right| \tag{2.6}$$

In other words, the effective masses of electrons and holes are related to the curvature of the respective band. Importantly, the concept of effective masses allows for a convenient description of the reaction a (quasi-)particle shows when an external field (e.g., an electric field) is applied.

2.1.3 Excitons

Since free electrons and holes as well as their effective masses in a semiconductor have been established, their Coulomb interaction is taken under consideration in this section. As both particles are electrically charged, the interaction between an electron and a hole can lead to a bound state. The neutral quasiparticle consisting of this bound pair is called an exciton. If an exciton moves within the crystal, it transports energy stored in the excited state without transporting net electric charge. Depending on the average spatial separation between electron and hole, one differentiates tightly bound excitons, termed Frenkel excitons, which are often characterized by binding energies of around 1 eV, from weakly bound excitons, termed Wannier-Mott excitons. While Frenkel excitons possess a radius comparable to the unit cell size or smaller, Wannier-Mott excitons extend over many lattice sites. Thus, in the latter case the effect of the atoms in between electron and hole on their interaction can be summarized in an effective screening described by the permittivity $\epsilon = \epsilon_0\epsilon_r$ of the material.[18] Figure 2.4 a depicts a

Wannier-Mott exciton schematically. As this type of exciton is commonly accepted to be present in the materials investigated in this thesis,[22] its theory is introduced in more detail in the following.

To describe the exciton states, a reduced mass m_{ex} and an exciton wave vector $\mathbf{K} = \mathbf{k}_e + \mathbf{k}_h$ are defined. The reduced mass m_{ex} is given by the reduced masses of electron and hole:

$$m_{\mathrm{ex}} = \left[\frac{1}{m_{\mathrm{e}}^*} + \frac{1}{m_{\mathrm{h}}^*}\right]^{-1} \tag{2.7}$$

If we assume the bands to be parabolic, the excitonic dispersion relation is also parabolic with respect to the total wave vector $\mathbf{K}$:[13]

$$E_{\mathrm{n}}(\mathbf{K}) = E_{\mathrm{G}} - E_{\mathrm{n}}(0) + \frac{\hbar^2}{2(m_{\mathrm{e}}^* + m_{\mathrm{h}}^*)}\mathbf{K}^2 \tag{2.8}$$

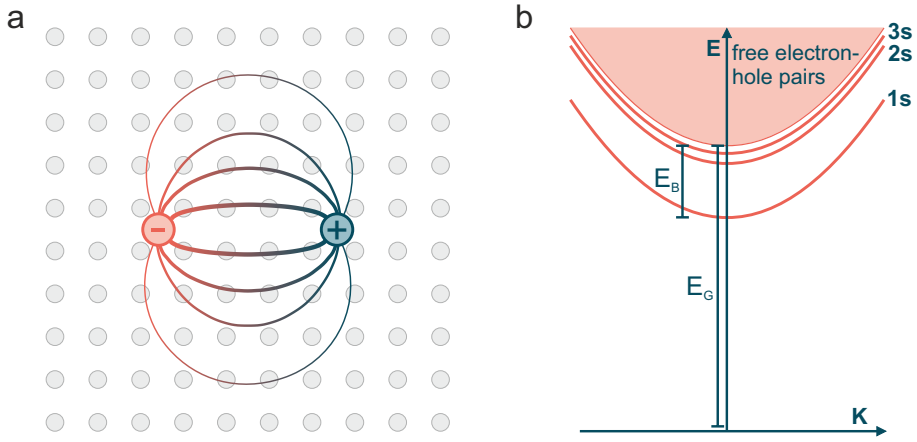

Figure 2.4: Wannier-Mott Exciton. a) Schematic representation of a Wannier-Mott exciton in a crystal lattice. The Coulomb interaction between the electron and hole is indicated by the connecting paths. **b)** The energy of an electron-hole pair plotted against their combined wave vector $\mathbf{K}$. In this representation the states associated with free electron-hole pairs form a continuum above the band gap. Below this continuum additional states exist, which represent bound states between electrons and holes, so called excitons. The energy difference between the continuum and the energetically lowest exciton state (1s) is defined as the exciton binding energy E_{B}.

Here, $E_{\mathrm{n}}(0)$ (from now on only called E_{n}) separates the exciton levels labeled by the quantum number n from the continuum of free electron-hole pairs and is thus the binding energy of the respective excitonic level. As this binding is similar to the binding in a hydrogen atom, the binding energies can be expressed in terms of the exciton Rydberg energy R_{y}^*:[17]

$$E_{\mathrm{n}} = R_{\mathrm{y}}^* \frac{1}{n^2} = \frac{m_{\mathrm{ex}} e^4}{32\,\pi^2 \epsilon_0^2 \epsilon_{\mathrm{r}}^2 \hbar^2} \frac{1}{n^2} \tag{2.9}$$

In this thesis the exciton Rydberg energy will be simply termed the exciton binding energy E_{B}. In addition, the so-called exciton Bohr radius a_{ex}, which represents the typical spatial extension of an exciton, is of importance and is defined as:

$$a_{\mathrm{ex}} = \frac{4\,\pi \epsilon_0 \epsilon_{\mathrm{r}} \hbar^2}{m_{\mathrm{ex}} e^2} \tag{2.10}$$

Since an exciton comprises an electron and a hole and its energy is related to their combined wave vector **K**, it can not be displayed in the standard band structure plot also termed one-particle picture. Therefore, the two-particle picture is introduced, which displays the energy of excited electron-hole pairs as a function of **K**. In this representation the excitonic levels appear as parabolas below a continuum of states describing free electron-hole pairs (see Figure 2.4 b).[21]

To which degree excitons are present in a semiconductor depends strongly on how E_B compares to the thermal energy $E_{th} = k_B T$ (around 26 meV at 300 K) for the temperature of the system. If neither E_B nor E_{th} dominates, an equilibrium between excitons and free charge carriers will form. Additionally, the charge carrier density influences exciton formation, since it increases the probability of an electron and a hole to be in the vicinity of each other. The fraction of electron-hole pairs residing in a bound excitonic state can be quantitatively described by the Saha equation.[23]

As an additional note, an excitonic state can split up further into multiple sub-levels called the exciton fine structure. This can be caused by a degenerate VBM or CBM, which would introduce different types of holes or electrons available at the band edge. Even with non-degenerate band edges, however, the hole and the electron comprising the exciton can be spin-up or spin-down particles, which also introduces a fine structure of an excitonic level. Whether these sub-levels introduced by the fine structure are degenerate or not depends on the system, which is an integral part of the results presented in this thesis.

2.1.4 Trions and Biexcitons

If E_B is sufficiently large and the excitation density high, bound states between more than two charge carriers become more likely. While these prerequisites are in most cases not satisfied in bulk semiconductors, they can be in confined structures and are therefore mentioned here.

Trion: An exciton that is bound to an additional electron or hole is termed a negative or positive trion, respectively. Such trions can often be observed in confined nanostructures at low temperatures, especially if charged nanocrystals, which possess an excess electron or hole, are an issue.[21]

Biexciton: If two excitons form a bound state similar to a hydrogen molecule, one speaks of a biexciton. The binding energy of a biexciton is higher than that of a trion and typically on the order of 10 - 20 % of E_B.[24]

2.1.5 Confined Semiconductors

The last section covered fundamental concepts regarding semiconductors and basically ignored the finite size of real crystals. The research conducted in the scope of this thesis, however, concerns semiconductor nanocrystals with edge lengths of a few nanometers. And since the size of these nanocrystals in at least one dimension is on the order of the exciton Bohr radius, quantum confinement is induced and the properties of the semiconductor are affected. These quantum confinement effects (for convenience only termed confinement effects in some cases) are discussed here.

Particle in a Box

The particle in a box is a classical quantum mechanics textbook example describing a particle trapped between two infinitely high potential barriers. However, it is very useful to demonstrate the effect quantum confinement induces on an electron or hole in a semiconductor. The potential describing a particle in a one-dimensional box can be written as:

$$V(z) = \begin{cases} 0 & 0 \leq z \leq L \\ \infty & \text{otherwise} \end{cases} \tag{2.11}$$

Solving the Schrödinger equation of this system, while satisfying the boundary conditions $\psi_n(z = 0) = \psi_n(z = L) = 0$, produces the wave functions:[25]

$$\psi_n(z) = \begin{cases} A_n \sin\left(\frac{n\pi z}{L}\right) & 0 \leq z \leq L \\ 0 & \text{otherwise} \end{cases} \tag{2.12}$$

The corresponding energy eigenvalues can be written as:

$$E_n = \frac{n^2\pi^2\hbar^2}{2\,mL^2} \tag{2.13}$$

The important relation here is $E_n \propto L^{-2}$. And while colloidal nanocrystals may be better approximated by a two-step finite well due to the ligand layer attached to their surface, this still demonstrates that the discrete energy levels of a particle in a box increase strongly as its spatial freedom is limited. Whereas discrete energy levels replace the continuous bands only in semiconductor nanocrystals strongly confined in all three dimensions, an increase of the continuum onset $E_C = E_G + E_e + E_h$ can already be observed once the spatial extent of one crystal dimension approaches the exciton Bohr radius. Here, E_e and E_h denote the confinement energies of the electrons and the holes, respectively.[18] Notably, in literature one often differentiates between weak confinement ($L \geq a_{ex}$) and strong confinement ($L < a_{ex}$). This distinction is, however, not precisely defined, as the properties of the semiconductor evolve smoothly with size and the size dependence only becomes significantly larger for smaller sizes.

Confined Excitons

In Subsection 2.1.3 it was mentioned that the occurrence of excitons is coupled to the ratio between E_B and k_BT. In many nanocrystal systems E_B is strongly increased compared to the respective bulk material and excitonic effects therefore strongly affect a number of optoelectronic properties. The reasons for this increase in E_B are examined here for confinement in one dimension, since this type of structure is highly relevant for the results of this thesis.

The effect confinement induces on E_B can be divided into two main contributions. The first contribution is the restriction of the position of electron and hole in respect to the exciton center of mass. By decreasing the degree of freedom to move from 3D to 2D, E_B already increases four-fold:[18]

$$E_B^{2D} = 4E_B^{3D} \tag{2.14}$$

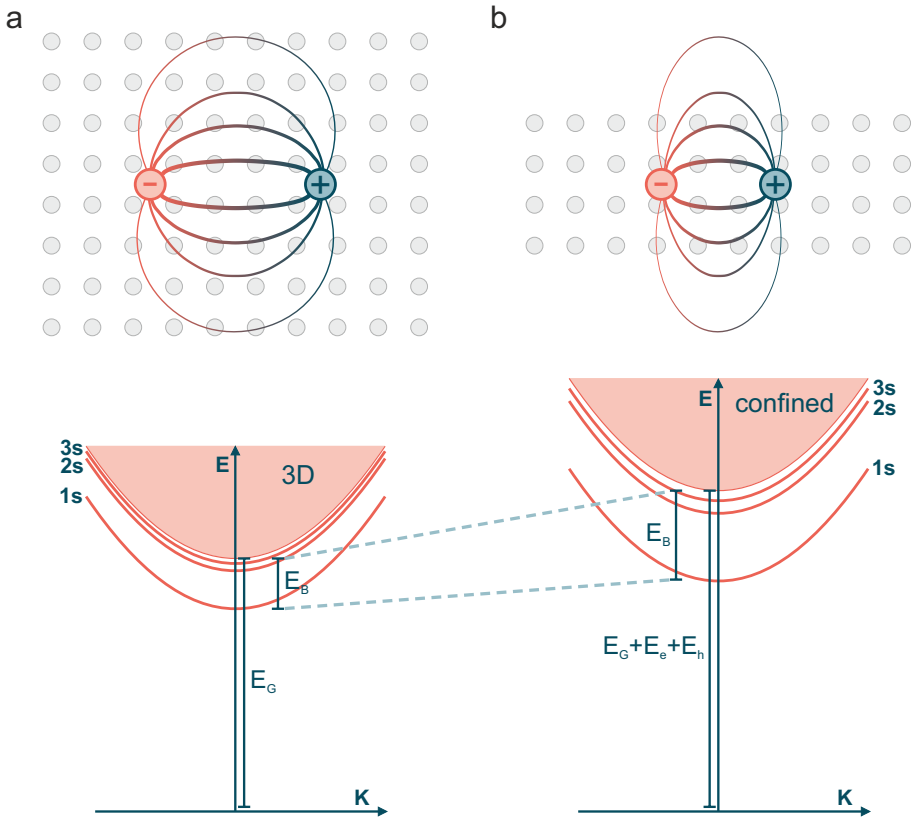

Figure 2.5: Confined Exciton. a) An exciton in a bulk crystal with its electron-hole states in the two particle picture. **b)** Confining the exciton in one dimension increases E_B as well as the continuum onset $E_\mathrm{C} = E_\mathrm{G} + E_\mathrm{e} + E_\mathrm{h}$ by the confinement energies of the electron and the hole.

The second contribution is depicted in the scheme in Figure 2.5 b and often termed dielectric confinement. The Coulomb interaction between electron and hole is a spatial effect and the corresponding field lines partially extend outside of the crystal. In essence, the dielectric screening of the interaction stemming from the crystal atoms is reduced in sufficiently small crystals and the permittivity $\epsilon = \epsilon_0\epsilon_\mathrm{r}$ of the surrounding becomes relevant. This further increases E_B and the resulting E_B often exceeds the limit given by the first effect.[10,26]

Figure 2.5 summarizes the confinement effects introduced so far schematically. It should be noted that the increase in the continuum onset is sometimes simply referred to as an increase in band gap energy E_G in the results part of this thesis.

Effect on Density of States

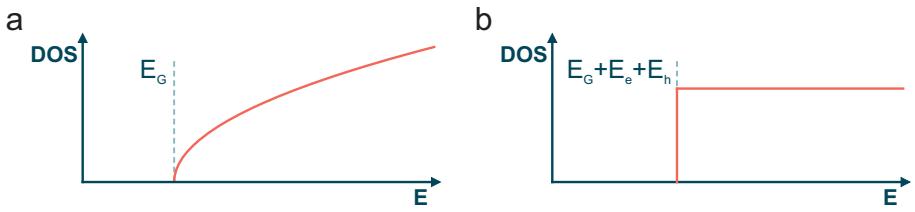

Figure 2.6: Density of States. The density of states as a function of E for **a)** a 3D semiconductor and **b)** a 2D semiconductor.

Reducing the dimensionality of a system furthermore changes the DOS introduced in Equation 2.4. Whereas in 3D bulk crystals the DOS within a band shows a $\propto E^{1/2}$ dependence, in 2D quantum wells

this becomes a $\propto E^0$ dependence and in 1D quantum wires a $\propto E^{-1/2}$ dependence. Furthermore, in 0D quantum dots energy levels become discrete, which can lead to atom-like properties.[13] As the DOS affects some optical properties introduced later, it is plotted in Figure 2.6 for the 3D and 2D cases, which are the most relevant for this thesis.

2.2 Interband Transitions

Many of the nanocrystal properties investigated in this thesis are of optical nature or probed employing optical techniques. In semiconductors interband transitions are responsible for many aspects of light-matter interaction and, thus, introduced in detail. In addition, non-radiative interband transitions are discussed, since they affect the results acquired with optical methods and the performance of optoelectronic devices. Lastly, different contributions to the width of photon emission spectra are covered.

2.2.1 Optical Excitation

In Subsection 2.1.2 the process of thermal excitation and generation of electron-hole pairs at finite temperatures was already discussed. The excitation density at thermodynamic equilibrium at room temperature, however, is generally rather low. Further possibilities for excitation include impact ionization or charge carrier injection through electrical contacts.[27,28] The excitation mechanism exploited in all experiments in this thesis for generating an exciton population, however, is optical excitation. If an incident photon possesses an energy $E_{\mathrm{ph}} = \hbar\omega \geq E_{\mathrm{G}}$, there is a probability that it is absorbed and an electron-hole pair is generated. Such a transition between an initial state $|\,i\,\rangle$ and a final state $|f\rangle$ under a perturbation H' stemming from the incident electromagnetic wave is generally described by Fermi's golden rule:[17,29]

$$\Gamma_{\mathrm{i}\to\mathrm{f}} = \frac{2\,\pi}{\hbar} \cdot |\langle f|H'|\,i\,\rangle|^2 \cdot D_{\mathrm{j}}\,(\hbar\omega) \tag{2.15}$$

Notably, the transition rate $\Gamma_{\mathrm{i}\to\mathrm{f}}$ has two main contributions: The first is the matrix element $|\langle f|H'|\,i\,\rangle|^2$ describing the probability of the transition. This element can also be zero, if a quantum mechanical selection rule is not satisfied by the transition. Such a transition is then termed forbidden. The second contribution to $\Gamma_{\mathrm{i}\to\mathrm{f}}$ is the joint density of states (JDOS) $D_{\mathrm{j}}\,(\hbar\omega)$:

$$D_{\mathrm{j}}\,(\hbar\omega) = \frac{2}{8\,\pi^3} \int \delta[E_{\mathrm{f}}(\mathbf{k}) - E_{\mathrm{i}}(\mathbf{k}) - \hbar\omega]\,\mathrm{d}^3\mathbf{k} \tag{2.16}$$

This is basically a counter of how many combinations of initial and final states in $\mathbf{k}$-space match the photon energy with their energetic spacing. Since this accounts for energy conservation and assumes the momentum of a photon to be zero, momentum conservation has to be examined next. The wavevector $\mathbf{k}$ and the momentum a photon carries are small compared to the size of the first Brillouin zone of a crystal. Therefore, optical transitions are generally depicted as vertical in band structure schemes. If the final state lies at a different point in k-space an additional quasiparticle, a phonon, has to be absorbed or emitted for the transition to take place.

It was stated above that E_{ph} has to at least match E_{G}. This is not completely correct, as the excitonic states introduced in Subsection 2.1.3 can also contribute to absorption and lead to the direct resonant generation of excitons. Due to the large E_{B} in nanocrystals this effect can be observed in the absorption spectra depicted in this thesis. Figure 2.7 illustrates this additional contribution to absorption.

Furthermore it is also possible for below band gap photons to be absorbed, if the energy of multiple photons is converted into one electron-hole pair. Vice versa can one photon generate multiple electron-

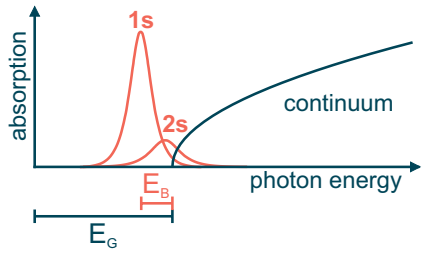

Figure 2.7: Excitonic Absorption. Direct excitation of the excitonic levels leads to an absorption of photons with $E_{\mathrm{ph}} < E_{\mathrm{G}}$. Absorption of the 1s exciton level plays the dominant role in this process. The continuum absorption in this example assumes the bulk DOS displayed in Figure 2.6.

hole pairs, if its energy is large enough.[30] For these effects to occur, however, large photon densities or photon energies are required, respectively. Thus, both of these effects play minor roles in the results part of this thesis, since these conditions are not fulfilled.

Intraband Processes

While this section focuses on the introduction of interband processes, which are a central aspect investigated in this thesis, intraband processes shall be briefly mentioned here. Upon excitation with a laser pulse different mechanisms can influence the population of excited carriers prior to recombination. To be able to exclude that these processes influenced the results obtained within this thesis markedly, the timescale on which they occur is discussed here.

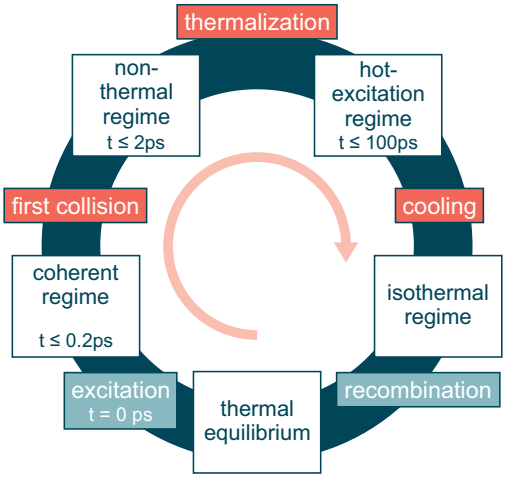

Figure 2.8: Inter- and Intraband Processes. The different processes following photoexcitation can be divided into two categories: First, excitation (discussed in Subsection 2.2.1) and recombination (discussed in Subsection 2.2.2 and Subsection 2.2.3) are termed interband processes (blue boxes), as an electron transfers into a different band. Second, multiple processes in which an excited (quasi-)particle stays within the same band are termed intraband processes (red boxes).

Figure 2.8 schematically depicts different processes following excitation with a laser pulse. Importantly, the order presented here is merely the most probable one due to the timescales on which the processes generally occur. In reality the regimes overlap and single recombination events can for example take place prior to carrier cooling. In many systems, however, the majority of excited carriers follows this scheme, which is described in the following.

At t = 0 ps the system is excited with a coherent laser pulse. In the experiment the laser pulse naturally has a finite temporal extent ranging from 200 fs to 200 ps in this thesis depending on the experiment. Furthermore, the excitation is always non-resonant with respect to the excitonic levels or the continuum onset and thus generates free electron-hole pairs with excess energy compared to the band edges in all of the experiments. Upon generation with a coherent laser pulse, a carrier is in coherence with the other carriers up until its first scattering event. Due to the laser pulse in the experiments being spectrally (i.e., energetically) narrow, the initial energetic distribution of the excited electrons and holes is narrow as well. Through carrier-carrier scattering, however, the electron and hole populations each approach a Maxwell-Boltzmann distribution and can then be characterized by a temperature. This process is termed thermalization. The carriers then relax (or cool) towards the band edges primarily via scattering events and the emission of phonons. The relaxation via phonon emission, first mainly involving optical and later acoustic phonons, is schematically depicted in Figure 2.9 for electron-hole pairs in the two-particle picture. In this representation, another important process within the scope of this thesis, namely the formation of excitons can be illustrated. For an electron-hole pair to form this bound state it has to transfer into one of the excitonic states described by the parabolas below the continuum. Subsequently, the formed exciton can further relax towards the minimum of the excitonic dispersion relation. All of the processes up to this point are called intraband processes.[31]

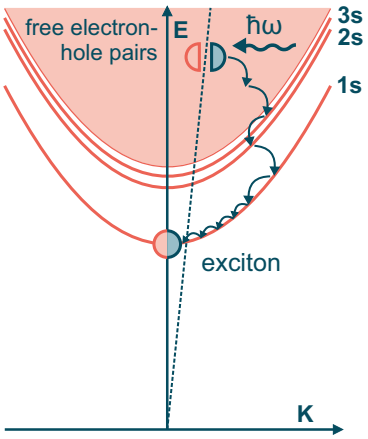

Figure 2.9: Carrier Cooling. Electron-hole states are displayed in the two-particle picture. The linear dispersion relation of photons is shown as a dashed line. Upon generation of an electron-hole pair via the absorption of a photon, the electron-hole pair relaxes into the excitonic 1s state via the subsequent emission of multiple phonons.

Recombination takes place primarily in the so-called isothermal regime, which explains, why the photon energy of luminescence spectra can often be related to E_G or $E_G - E_B$ independent of the excitation photon energy. Since recombination is examined in depth in this thesis, it is introduced in the following subsections in detail.

2.2.2 Radiative Recombination

Efficient light emission is the main property, which sparked the research interest in perovskite nanocrystals. If the excitation of the semiconductor occured optically, as described in Subsection 2.2.1, the emitted light is termed photoluminescence (PL). Upon electrical or thermal excitation for example, the emitted light is termed electroluminescence or thermoluminescence, respectively. The process responsible for the emission of photons from a semiconductor, radiative recombination, is largely

independent of the excitation mechamism and is covered here. Since hot carrier cooling, introduced in the last section, is generally much faster than recombination processes, charge carriers relax via phonon emission to the lowest state available. Typically, this is considered to be the CBM/VBM, however, for materials with large E_B, this is the minimum of the excitonic 1s state.

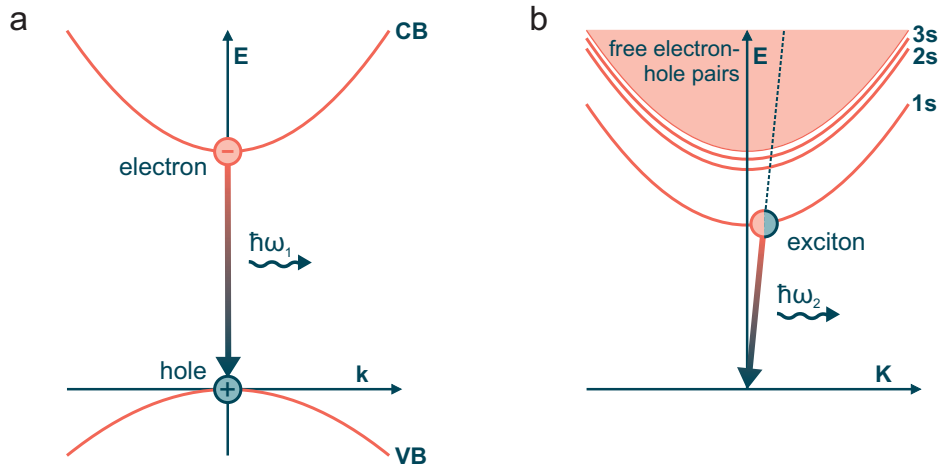

Figure 2.10: Radiative Recombination. a) The radiative recombination of an electron and a hole at the band edges is illustrated. The energy is emitted in the form of a photon. In the one-particle picture such a transition is generally depicted as vertical due to the relatively small momentum a photon with an energy comparable to the band gap energy E_G carries in respect to the size of the Brillouin zone in k-space. **b)** To illustrate the radiative recombination of an exciton, the two-particle picture has to be employed. Here, all recombination transitions have to end in the origin, which resembles the ground state. In this representation the linear dispersion relation of photons is often indicated (dashed line). Only states lying on this line can decay radiatively without the participation of an additional particle so that momentum conservation is satisfied.

Figure 2.10 a illustrates the radiative recombination process for a free electron and hole at the CBM and VBM, respectively. The photon emitted in such a process carries an energy close to E_G.[18] It cannot be exactly E_G, as a photon carries a small momentum. While the electron and hole have to differ slightly in $\mathbf{k}$ to satisfy momentum conservation, the transition is generally displayed vertical due to the negligible momentum of the photon.

Figure 2.10 b shows the same process for a 1s exciton in the two-particle picture. Here, the linear dispersion relation of the photon is added as a dashed line. Only electron-hole pairs occupying states on this line can decay radiatively to the ground state represented by the origin without participation of an additional particle.[13] In the case depicted, a photon with an energy close to $E_G - E_B$ is emitted.

Analogous to an optical excitation process via the absorption of a photon, which is covered in Subsection 2.2.1, the transition matrix element between the initial and the final state of an emission process also has to be taken into account. This is connected to the fact that additional conservation laws can apply. For the case of semiconductors with strong spin-orbit coupling, as investigated in this thesis, the total angular momentum J has to be conserved. Since a photon carries one unit of angular momentum, the initial and final state of a radiative recombination process have to differ by exactly this value to efficiently emit light.[32]

Furthermore, the dynamics describing the decay of $n(t)$ excited free charge carriers or $n_{ex}(t)$ excited excitons in a system, which allows for the particles to diffuse and encounter each other, differ. Since the probability for a collision of a free electron with a hole depends on the charge carrier density, the rate is proportional to $n(t)^2$ for an equal amount of free electrons and holes present ($n_e = n_h$). The

exponent of two stems from the fact that two unbound particles are involved in that process. Since an exciton can decay radiatively by itself, the decay rate of an excitonic population is simply proportional to the number of excitons $n_{ex}(t)$ at a given time t after excitation:

$$\text{Free electrons and holes} : \frac{dn(t)}{dt} = -k_r n(t)^2 \qquad \text{Excitons} : \frac{dn_{ex}(t)}{dt} = -k_{r/ex} n_{ex}(t) \tag{2.17}$$

These equation are of course only valid, if radiative decay is the only available decay channel and other recombination processes are negligible. In most cases, however, competing non-radiative decay channels cannot be neglected and affect the decay dynamics as well as the light emission efficiency. Therefore, these processes and their influence are introduced in the following section.

2.2.3 Non-Radiative Recombination

As mentioned in Subsection 2.2.1, multi-photon absorption or multiple exciton generation are negligible effects for the excitation parameters employed within this thesis. Thus, $n_{absorbed}$ absorbed photons generate $n_{ex}(t = 0) = n_{absorbed}$ electron-hole pairs in the material. The fraction of these excited electron-hole pairs, which has emitted photons, once the system is back in thermal equilibrium and all electron-hole pairs have recombined either radiatively or non-radiatively is called the photoluminescence quantum yield (PLQY):

$$PLQY = \frac{n_{emitted}}{n_{absorbed}} \left(= \frac{k_r}{k_r + k_{nr}} \right) \tag{2.18}$$

If the ratio between the radiative rate k_r and the total rate $k_r + k_{nr}$ is independent of the number of excited carriers and, thus, independent of t, it can also be used to calculate the quantum yield. This prerequisite is for example satisfied for a purely monomolecular decay of excitons meaning that each exciton decays without interaction with other excitons either radiatively or non-radiatively. Different non-radiative decay channels affecting the PLQY are discussed in the following.

Trap-Assisted Recombination

One property, which can facilitate a non-radiative decay via the emission of phonons, is the existence of trap states. These are introduced to the band structure by defects in the crystal structure such as vacancies, interstitials, line defects or planar defects. As nanocrystals possess a large surface to bulk ratio, especially point defects at the surface are of interest in this thesis.

The formed trap state is an additional state in the band structure, which a carrier is able to transfer into and out of, if the respective transfer is energetically possible. Depending on the energetic position of the formed trap in respect to the band gap, the corresponding state can affect excited charge carriers in different ways. If a trap state lies within the energetic range of a band, the dynamics of excited carriers are not affected strongly, as carriers can de-trap efficiently. Similarly, shallow traps, i.e., traps located within E_{th} of one of the bands, still allow for a de-trapping of the carriers. In contrast, so-called deep traps lying farther away from the CB and VB can result in a high non-radiative recombination rate k_{nr} and, following Equation 2.18, in a low PLQY. Figure 2.11 depicts a trap state within the band gap and a trapping process of an electron.[21]

Importantly, a trap-induced PLQY reduction is possible in systems, where free electrons and holes or excitons are the predominant species. Accordingly, traps states are also able to facilitate a non-radiative decay of excitons via the emission of phonons. Most likely, one of the constituents of an exciton is trapped in such a case, since many traps predominantly affect charged particles. Subsequently, both carriers relax separately via scattering into the ground state.

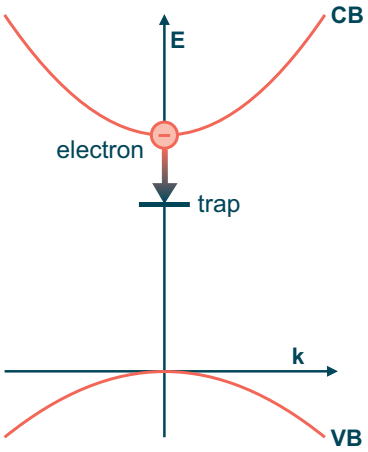

Figure 2.11: Trap-Assisted Recombination. A trap state within the band is depicted gap stemming from a defect in the crystal structure can lead to charge carriers being trapped. This process lowers the overall charge carrier mobility and facilitates non-radiative recombination.

Regardless of whether excitons or free electrons and holes are the predominant species, the rate equation for trap-assisted recombination can be written as:

$$\frac{dn(t)}{dt} = -k_{\text{trap}} n(t) \tag{2.19}$$

Auger Recombination

Another non-radiative decay mechanism, which becomes relevant at higher charge carrier densities is Auger recombination. In such a process, an electron recombines with a hole but instead of emitting a photon the energy is transfered to a third charge carrier, either an electron or a hole.[21] Naturally, an available state for the lifted electron or hole has to exist so that momentum and energy conservation are satisfied. Figure 2.12 a illustrates this. For excitons a similar process, called exciton-exciton annihilation, exists. Here, the energy released by the decay of an exciton is transferred to a second exciton lifting it into the continuum, as shown in Figure 2.12 b. In both cases the hot carriers relax quickly back down to the band edges or form an exciton again, respectively, in accordance with the processes described in Subsection 2.2.1. The rate equations governing the decay dynamics differ for free charge carriers and excitons, as three free carriers or two excitons are required:

$$\text{Free electrons and holes} : \frac{dn(t)}{dt} = -k_{\text{auger}} n(t)^3 \qquad \text{Excitons} : \frac{dn_{\text{ex}}(t)}{dt} = -k_{\text{EEA}} n_{\text{ex}}(t)^2 \tag{2.20}$$

Since exciton-exciton annihilation is an integral part of the results in this thesis, it is discussed in more detail in the following.

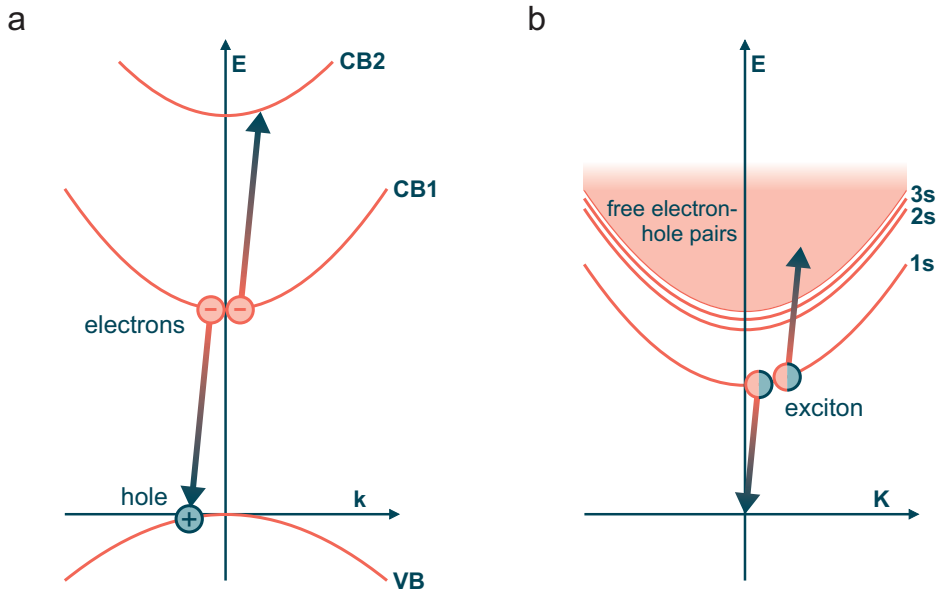

Figure 2.12: Auger Recombination and Exciton-Exciton Annihilation. a) An Auger recombination process involving two electrons and one hole in the one-particle picture is exemplified. The second electron is lifted into a higher CB. **b)** The two-particle picture is needed to illustrate an exciton-exciton recombination event. The second exciton is lifted into the continuum of states describing free electron-hole pairs.

2.2.4 Exciton-Exciton Annihilation

Within this thesis exciton-exciton annihilation (EEA) is investigated in an ensemble of non-interacting (spatially separated) nanocrystals. The situation differs strongly from a larger system, where a multi-particle process is generally described by a concentration-dependent lifetime or decay rate. In one small nanocrystal, however, the number of optically generated excitons is small, e.g. $N = 0, 1, 2, 3, 4...$, even at higher excitation densities. Therefore, the concentration dependence of the exciton-exciton annihilation lifetime becomes quantized and τ_2, τ_3, τ_4... can be assigned as the respective lifetimes.[33] Naturally, two excitons constitute the minimum required for EEA to take place. Figure 2.13 illustrates these processes and indicates that exciton-exciton-annihilation competes with the monomolecular recombination lifetime of the excitons τ_1. However, the monomolecular decay is generally much slower so that EEA dominates the dynamics until only one exciton in a nanocrystal is left.

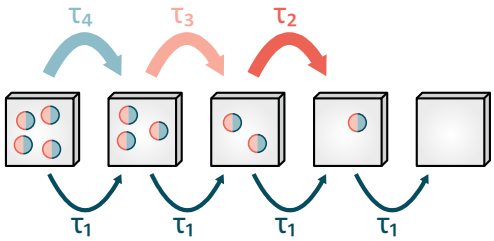

Figure 2.13: Exciton-Exciton Annihilation in a Single Nanocrystal. The quantized exciton-exciton annihilation lifetimes τ_2, τ_3, τ_4 are generally much shorter than the monomolecular lifetime τ_1. Accordingly, the decay dynamics are dominated by EEA processes until one exciton is left. As multi-particle processes depend on the exciton density, it follows that $\tau_2 > \tau_3 > \tau_4$.

Upon optical excitation of an ensemble of non-interacting nanocrystals, a number of excitons is generated, which is distributed over all nanocrystals in the excitation volume. Assuming that the absorption of one photon does not decrease the probability of the nanocrystal to absorb another

one, which is valid for the excitation densities in this thesis, the distribution of excitons over the nanocrystal ensemble can be described by Poisson statistics:[33]

$$P(\langle N\rangle, N) = \frac{\langle N\rangle^N}{N!} e^{-\langle N\rangle} \tag{2.21}$$

This formula delivers the probability for a nanocrystal to contain N photogenerated excitons depending on the average number of excitons generated per nanocrystal $\langle N\rangle$. Figure 2.14 illustrates some of the Poisson probabilities.

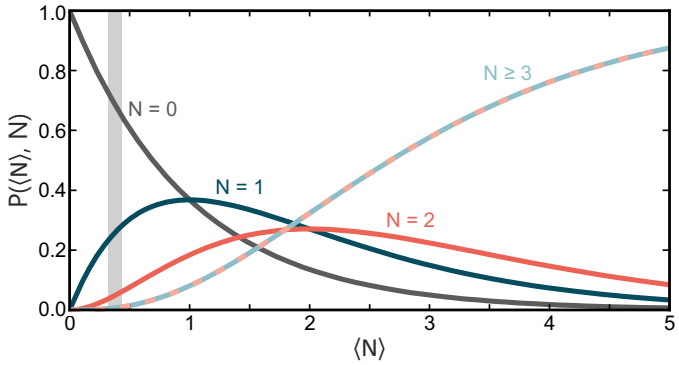

Figure 2.14: Poisson Statistics. The probability for a nanocrystal to contain N excitons upon excitation is plotted against the average number of excitons generated per nanocrystal $\langle N\rangle$. For a large ensemble this probability resembles the fraction of nanocrystals, which contains N excitons, for a given $\langle N\rangle$. If the relation between $\langle N\rangle$ and the optical excitation density is known, the fraction of nanocrystals containing multiple excitons and, thereby, the prevalence of EEA can be tuned. For excitation densities within the interval highlighted in grey for example, there is already a small probability for nanocrystals to contain two excitons initially, while three or more excitons are still unlikely to be generated in the same nanocrystal.

The size n of the total exciton population in a large nanocrystal ensemble at a certain time $t = t_1$ after excitation displays a saturation behavior in respect to excitation density. This is a result of the fast EEA, which has already taken place at time t_1 in all nanocrystals containing at least two excitons initially, while the number of monomolecular recombination events up until that time is negligible. It follows that at maximum only one exciton is left in a nanocrystal and $\langle N\rangle(t_1) \approx 1$ for high excitation densities. The exciton population $n(t_1)$, therefore, is equal to the number of nanocrystals excited at least once during excitation, which can be expressed by Poisson statistics:

$$n(t_1, \langle N\rangle) = 1 - P(\langle N\rangle, 0) = 1 - e^{\langle N\rangle} \tag{2.22}$$

To deduce the average number of excitons per nanocrystal, one needs the excitation density I_{ex}. These two values are connected via a proportionality constant C_{ex}, as per $\langle N\rangle = C_{ex} I_{ex}$. Once C_{ex} and thereby $\langle N\rangle$ are determined, the excitonic density can be chosen in such a way that $P(\langle N\rangle, N = 2)$ is quite high, while $P(\langle N\rangle, N \geq 3)$ is rather low. An appropriate interval ($0.3 \leq \langle N\rangle \leq 0.4$) is highlighted in grey in Figure 2.14. In this interval around 4.3 % of the nanocrystals contain two excitons upon excitation, while only 0.6 % contain more excitons. In that way, exciton-exciton annihilation is mainly characterized by τ_2 allowing for its extraction. The EEA lifetime can then be compared for different samples with τ_2 representing EEA in general. This is not possible, if it is unknown which τ_N has been measured for each sample.

Summing up, this mathematical description of EEA in an ensemble of non-interacting nanocrystals can be employed to extract the average number of excitons generated per nanocrystal for a given excitation density. Subsequently, this knowledge allows for the comparison of EEA in different nanocrystal samples by ensuring that the annihilation lifetime measured is related to nanocrystals containing exactly two excitons.

2.2.5 Broadening of Optical Transitions

Following the introduction of different excitation and recombination mechanisms in semiconductors, a more detailed description of the photons involved in radiative processes is presented here. An optical transition in a semiconductor is in theory well defined and characterized by the energetic spacing of the levels involved. Real emission or absorption spectra related to this transition, however, do not constitute delta functions but broadened distributions centered around this energetic spacing. The mechanisms responsible for the broadening can be divided into two groups: homogeneous broadening and inhomogeneous broadening. Since the spectral width of the emission of a semiconductor is an important property in many lighting applications, both contributions are introduced in the following.

Inhomogeneous Broadening

This type of broadening stems from imperfections or, as the name states, inhomogeneities of a real sample. While different types of bulk crystal defects are the main contributor in bulk crystals, shape and size differences, surface defects and variations in the dielectric environment mainly affect an ensemble of nanocrystals. Consequently, the energy related to a specific transition is subject to local variations leading to a broadening of the transition. Since these variations, e.g. in nanocrystal size, tend to follow a normal distribution, inhomogeneous broadening can generally be described by a Gaussian lineshape. Importantly, this type of broadening is temperature-independent.

Homogeneous Broadening

The first contribution to this type of broadening, the natural linewidth, is also temperature-independent. Even at T = 0 K and without inhomogeneous broadening the emission linewidth of any emitter does not represent a delta function due to this effect, which is rooted in Heisenberg's uncertainty principle.[34] In addition, carrier-carrier scattering can also broaden the optical transition already at T = 0 K. The main contribution to homogeneous broadening at room temperature, however, stems from carrier-phonon scattering and in some cases carrier-impurity scattering. Phonons have already been mentioned briefly in Subsection 2.2.2 in the context of indirect optical transitions. As their influence on homogeneous broadening is the subject of investigation in part of the results, they shall be introduced here.

The phonon, a quasiparticle, is an elementary vibrational motion of the atoms in the crystal lattice, characterized by a wave vector $\mathbf{k}$ and a frequency $\omega(\mathbf{k})$. Phonons can be divided into acoustic and optical phonons, while the latter only exist in crystals with at least two atoms in the primitive unit cell. These atoms oscillate out-of-phase for optical phonons inducing an oscillating electrical field in ionic crystals like lead halide perovskite. Notably, optical phonons possess a non-zero frequency and energy at the center of the Brillouin zone. The dispersion relations of acoustic and optical phonons in a 1D lattice with two alternating atom species are depicted in Figure 2.15.[11]

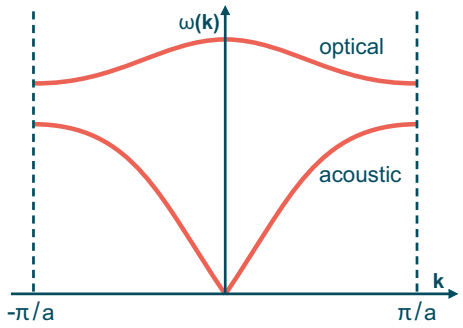

Figure 2.15: Phonon Dispersions in a Linear Diatomic Chain. In a crystal with at least two atoms in its primitive unit cell two types of phonons exist: Acoustic and optical phonons. In contrast to acoustic phonons, optical phonons possess a non-zero frequency at the center of the Brillouin zone. In an ionic crystal an optical phonon induces an oscillating electrical field, since the ionic cores in the unit cell move out-of-phase.

Since the number of phonons in the material is temperature-dependent, the contribution of exciton-phonon interaction to homogeneous broadening is as well. If exciton-phonon interaction is the main source of thermally induced broadening, the linewidth can be written as:[35]

$$\Gamma(T) = \Gamma_0 + \Gamma_{ac}(T) + \Gamma_{op}(T) = \Gamma_0 + \gamma_{ac}T + \frac{\gamma_{op}}{\exp\left(\frac{E_{op}}{k_B T}\right) - 1} \tag{2.23}$$

Here, $\Gamma_0 = \Gamma(T = 0)$ contains all temperature independent contributions to the linewidth. The other two terms $\Gamma_{ac}(T)$ and $\Gamma_{op}(T)$ contain the interaction with acoustic and optical phonons, respectively. Both of these terms combine a factor representing the strength of the interaction (γ_{ac} and γ_{op}) with the temperature-dependent size of the respective phonon population. While the number of acoustic phonons increases linearly with temperature, the population of optical phonons follows a Bose-Einstein distribution function $\frac{\gamma_{op}}{\exp\left(E_{op}/k_B T\right)-1}$ with E_{op} representing the weakly dispersive optical phonon energy. A purely homogeneously broadened sample would exhibit an emission spectrum with a Lorentzian shape. Due to non-negligible inhomogeneous broadening, however, the Lorentzian has to be convoluted with a Gaussian resulting in a so-called Voigt profile.[36]

2.3 Energy Transfer

For two nanocrystals in the vicinity of each other, the question arises, if an exciton is able to transfer between them. In particular, non-radiative transfer processes without the participation of an intermediate photon are of interest. As excitonic transfer via Förster resonance energy transfer (FRET) is the dominating mechanism, which can enable such a process for the nanocrystals and distances investigated in this thesis, it is introduced here.[37]

FRET is a dipole-dipole interaction strongly dependent on distance between an excited donor and an acceptor in the ground state. It is a resonant process and, thus, activates a vibronically excited acceptor state, which subsequently relaxes into the lowest vibronic state.[38] While the terminology already suggests that this initially described the interaction of molecular fluorophores, it was demonstrated that the concept can also be applied to semiconductor nanocrystals.[39] A plethora of studies has since observed FRET in various semiconductor nanocrystal systems and determined it to be the dominant transport mechanism for excitons between adjacent nanocrystals.[40,41] Since an excited donor nanocrystal has the possibility to decay without a FRET process with the rate $k_\mathrm{D} = k_\mathrm{r} + k_\mathrm{nr}$, as discussed in Subsection 2.2.3, the FRET rate k_FRET competes with k_D. A FRET efficiency η_FRET can, therefore, be defined, as:

$$\eta_\mathrm{FRET} = \frac{k_\mathrm{FRET}}{k_\mathrm{d} + k_\mathrm{FRET}} \tag{2.24}$$

The FRET rate k_FRET itself is described by a formula Theodor Förster derived and can be written as:[38]

$$k_\mathrm{FRET} = \frac{9c^4\kappa^2}{8\pi n^4 \tau_\mathrm{D} d^6} \int_0^\infty \frac{f_\mathrm{D}(\omega)\sigma_\mathrm{A}(\omega)}{\omega^4}\, d\omega \tag{2.25}$$

Here, c denotes the speed of light, κ the orientation factor encoding the donor-acceptor transition dipole orientation, n the refractive index of the surrounding medium and τ_D the lifetime of the pure donor. Furthermore, the distance d between donor and acceptor as well as the spectral overlap integral between the donor emission and the acceptor absorption, a vital prerequisite for FRET to occur, strongly affect the FRET rate. For simplicity, however, all quantities except τ_D and d are often represented by the so-called Förster radius R_0:

$$k_\mathrm{FRET} = \frac{1}{\tau_\mathrm{D}} \left(\frac{R_0}{d}\right)^6 \tag{2.26}$$

With this definition, the system-specific R_0 corresponds to the distance d for which the FRET efficiency is exactly 50 %, as $d = R_0$ yields $k_\mathrm{FRET} = \frac{1}{\tau_\mathrm{D}} = k_\mathrm{D}$. In many known donor-acceptor combinations R_0 assumes a value between 2 nm and 10 nm and, as a rule of thumb, it is, thus, often stated that FRET plays a role at distances below 10 nm.

2.4 Lead Halide Perovskite Nanocrystals

All systems investigated within this thesis can be assigned to this material class. First, bulk lead halide perovskites and their properties are introduced before presenting nanocrystals of the same crystal structure. Different nanocrystal shapes and features like the temperature-dependence of the band gap or phase transitions are discussed. Throughout the section, recent findings concerning this material class are referenced, which form an important basis for the results part of this thesis.

2.4.1 Lead Halide Perovskites

While the term perovskite initially referred to the mineral calcium titanate $CaTiO_3$, it is now generally applied to any material exhibiting the same ABX_3 crystal structure. The binding in these compounds is typically of ionic nature and all perovskites investigated within this thesis contain a monovalent A-cation, a divalent B-cation, and a monovalent X-anion. Figure 2.16 depicts the perovskite crystal structure.

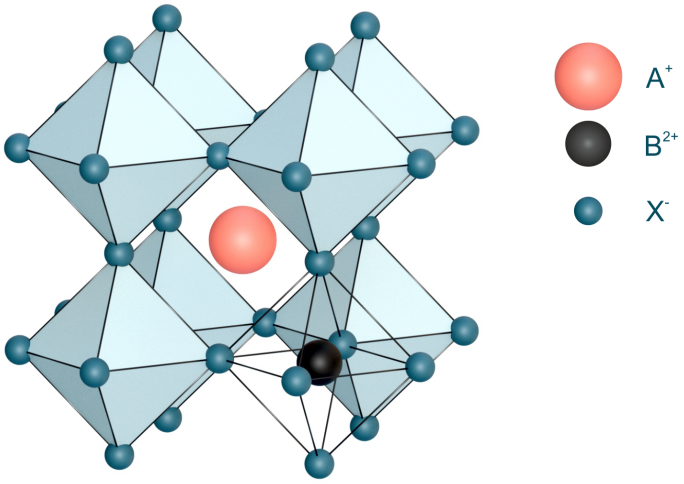

Figure 2.16: Perovskite Crystal Structure. The corner-sharing octahedra shown in light blue are spanned by the lattice sites occupied by X-anions. A B-cation is located in the center of each octahedron, as seen in the octahedron without solid faces. Furthermore, every void between eight octahedra contains an A-cation.

The growing interest in this material class in the past decade was driven by the good performance of perovskite solar cells. Notably, efficient devices often employ compositions containing lead as the B-cation and chloride, bromide or iodide as the X-anion. Thus, the term lead halide perovskites (LHPs) emerged. Additionally, in many of the efficient solar cells the A-site was occupied by the small organic molecules methylammonium (MA) or formamidinium (FA) leading to the expression organic-inorganic LHPs.[42]

Besides the constituents mentioned, there is a vast number of further components and combinations, which are able to form a perovskite. Naturally, the combination of ions has to preserve overall charge neutrality but there are also constraints on the sizes of the atomic or molecular ions involved. These constraints are often written down in terms of the Goldschmidt tolerance factor t_G:[43]

$$t_G = \frac{R_A + R_X}{\sqrt{2}(R_B + R_X)} \tag{2.27}$$

For a composition to be able to crystallize in a perovskite structure, t_G should be in the range from 0.8 to 1. In addition to the Goldschmidt tolerance factor, the so-called octahedral factor, which is just the ratio of the radii of the B-cation and X-anion, is also often taken into account to evaluate possible perovskite compositions.[44] Furthermore, not all compositions form a cubic perovskite structure, if their t_G deviates from one. In a $CsPbBr_3$ crystal for example, the Cs^+ ions do not fill the voids between the octahedra sufficiently, resulting in a t_G of 0.815. Thus, at room temperature and below, $CsPbBr_3$ displays an orthorhombic crystal structure caused by a tilting of the octahedra. Only at elevated temperatures, the increased kinetic energy of the ions leads to a tetragonal (88 ℃) and finally cubic (130 ℃) crystal structure for this composition.[45]

Advantageous Optoelectronic Properties

Here, the properties of bulk LHP crystals, which paved the way towards efficient solar cells and lead to scientific interest, are summarized. This serves as a source for comparison of LHP nanocrystals to LHP bulk crystals to enable a discussion of the similarities and differences. In general, the active semiconductor layer of a solar cell has to fulfill certain prerequisites, which are stated here and then discussed in the same order in individual paragraphs for the case of LHPs: (1.) First, the optical absorption coefficient of the material should be high at wavelengths which strongly contribute to the solar spectrum, to enable thin active layers with a high absorbance. (2.) Second, the onset of the absorption correlated to the band gap energy E_G should be close to the maximum of the Shockley-Queisser limit around 1.3 eV.[46] (3.) Third, a low exciton binding energy is beneficial as this energy has to be overcome to achieve charge carrier separation, if excitons are present. (4.) Fourth, the charge carrier diffusion lengths should be long enough for carriers to reach the respective contacts at the boundaries of the active layer.

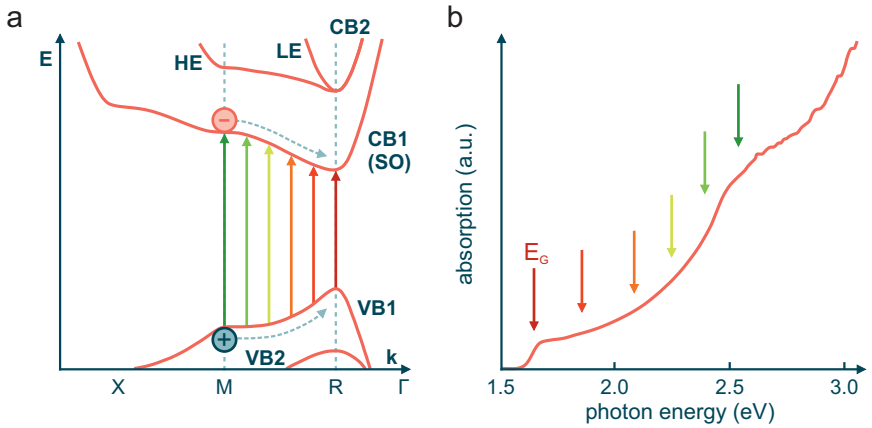

Figure 2.17: Band Structure and Absorption of $MAPbI_3$. a) The electronic band structure of $MAPbI_3$ plotted along specific lines connecting high-symmetry points in the Brillouin zone. The results stem from DFT calculations.[47,48] A direct band gap can be found at the R-point of the Brillouin zone. **b)** The absorption spectrum of $MAPbI_3$ shows an onset connected to the band gap at the R-point. Furthermore, the absorption rises steeply throughout the visible wavelengths due to the relatively flat VB1 and CB1 between the R-point and the M-point. Adapted from Reference [49].

1. Band Structure and High Optical Absorption

Fermi's golden rule (Equation 2.15) states that absorption is closely related to the band structure. Generally, insights into the band structure stem from a combination of experimental data and density-

functional theory (DFT) calculations. A calculated band structure for $MAPbI_3$ is depicted in Figure 2.17 a, where the electronic dispersion relation is plotted along specific lines connecting high-symmetry points in the Brillouin zone. For an introduction on Brillouin zones see Subsection 2.1.1. Importantly, a direct band gap is located at the R-point. From thereon the VB1 and the CB1 evolve relatively flat towards the M-point. These flat bands lead to a high density of initial and final states for optical transitions in the visible spectral range leading to a high absorption at these wavelengths (see Figure 2.17 b). Besides a high JDOS (see Equation 2.16), the matrix element $|\langle f|H'|i\rangle|^2$, which denotes the probability of a transition, is of importance. The VBM at the R-point arises from antibonding states stemming from the hybridization of 6s lead orbitals and 5p iodine orbitals and exhibits an overall s character.[50] In contrast, the CBM located also at the R-point is formed of empty 6p lead orbitals. This difference of one in angular momentum renders optical transitions between these bands dipole-allowed. Notably, in most conventional semiconductors the situation is the opposite with a p-like VBM and an s-like CBM. This also leads to the existence of light and heavy electrons (LE and HE) and a split-off (SO) band in LHPs compared to heavy and light holes in other systems. Due to strong spin-orbit coupling, the SO band is lowered and, thus, is called the CB1, as it contains the CBM. Both, the VBM and CBM are, therefore, degenerate only in terms of spin in this material and can each be approximated by a single parabola. Since the A-cation only has an indirect influence on the band gap by affecting the distance between the other lattice sites, the $MAPbI_3$ band structure depicted here is representative for other LHPs.

Furthermore the dependence of the band structure on temperature shall be discussed. As mentioned above, the Goldschmidt tolerance factor t_G does not equal one in LHPs, neither in those containing cesium nor those containing MA. Therefore, at T = 0 K, the octahedra are tilted and the crystal structure is orthorhombic. Only with increasing temperature, phase changes into the tetragonal and finally the cubic phase occur. While in the compositions containing MA or FA one or both of these transitions take place below room temperature, $CsPbBr_3$, the composition under investigation in this thesis, is still in the orthorhombic phase at room temperature. These phase transitions are mentioned here again, as the rearrangement of the atoms at specific temperatures leads to discontinuities in the otherwise continuous evolution of the band gap with temperature.[51] The continuous evolution manifests in an increase of the band gap with increasing temperature. This contrasts the findings in typical semiconductors like Si or GaAs, where the band gap generally decreases with increasing temperature.[52] The reason for this lies in the antibonding nature of the states in the VBM in LHPs.[53]

2. Tunable Band Gap

The criterion that a specific band gap is required for efficient solar cell operation is met by the band gap tunability of LHPs. With an exchange of the halide and the possibility of forming mixed-halide LHPs, the band gap can be tuned throughout the visible range and specifically tailored to different applications.[54,55] Employing iodide as the halide leads to the smallest band gap. The band gap of $MAPbI_3$, a very prominent compound, however, is still around 1.6 eV and, thus, slightly higher than the the optimum band gap in terms of the Shockley-Queisser limit. Nevertheless, the solar conversion efficiencies theoretically possible with this band gap exceed 30 % in a single junction architecture.

3. Exciton Binding Energy

For LHPs there has been some discrepancy between different measurements of the exciton binding

energy. Reported values for $MAPbI_3$, for example, range from 2 to 62 meV.[49] While some of these values lie above thermal energies at room temperature ($k_B T_{RT} \approx 26$ meV), there is a general consensus that mainly free electrons and holes are present at room temperature. Measurements of the charge carrier decay dynamics in bulk $MAPbI_3$ crystals support this assumption. This behavior is rather surprising, since solution-processed materials as well as organic solids are often characterized by high exciton binding energies due to low dielectric screening.[56] Whereas in many of these systems the picture of Frenkel excitons has to be employed, the theory of Wannier-Mott excitons as described in Subsection 2.1.3 is sufficient in LHPs.

4. Electron-Hole Diffusion Lengths

It was shown that electron-hole diffusion lengths can exceed a micrometer in bulk LHPs.[57] Since LHP layers of just a few hundred nanometers thickness are enough to enable a high absorbance, most of the excited carriers are able to reach the respective contacts in light harvesting devices. The long diffusion lengths are closely connected to surprisingly long lifetimes of electrons and holes in these layers. Both monomolecular as well as bimolecular recombination rates of free charge carriers can be quite low in LHPs (for an introduction on recombination refer to Subsection 2.2.2 and Subsection 2.2.3). First, trap-assisted recombination is strongly suppressed by the defect-tolerance of the material.[58] Here, defect tolerance refers to the fact that defects with a low formation energy, which are thus likely to occur, only induce shallow traps close to or within bands. These trap states do not lead to considerable non-radiative recombination and, therefore, do not decrease the charge carrier lifetime strongly. Second, bimolecular, radiative recombination has to be taken into account. Once trap-assisted decay is eliminated, bimolecular recombination sets an intrinsic limit to the diffusion length of carriers.[49] Advantageously, in LHPs the ratio between the bimolecular recombination constant and the charge-carrier mobility is exceptionally low explaining the long diffusion lengths.[59]

The combination of all these properties constitutes the basis for the high solar conversion efficiencies achieved in simple planar heterojunction architectures.

Disadvantageous Properties

The main disadvantage of LHPs compared to Si or GaAs is a lower stability under some environmental conditions.[60,61] Even if water- or oxygen-induced damage can be reduced sufficiently by different strategies such as encapsulation, this would require additional fabrication steps. Depending on the complexity of these procedures, this counters a main advantage of LHPs, namely their very cheap and easy synthesis. Furthermore, due to a high mobility of the halide ions, mixed-halide perovskites are on the one hand easy to fabricate but on the other hand suffer from phase segregation into domains with different halide compositions.[62] These stability issues constitute the main obstacles LHPs have to overcome to achieve wide-spread commercialization.

2.4.2 Lead Halide Perovskite Nanoplatelets

Having discussed LHPs and their properties in general, LHP nanocrystals shall be introduced next. The theoretical foundation concerning quantum confinement of semiconductors can be found in Subsection 2.1.5. In that section the effects of confinement are exemplified by a one-dimensional particle in a box model. In a real system, however, confinement can be induced in zero, one, two or

three dimensions. Normally, when addressing these systems, the unconfined dimensions are counted resulting in 3D, 2D, 1D and 0D systems. In literature these systems are often called bulk or bulk-like (3D), quantum well (2D), quantum wire (1D) and quantum dot (0D). In contrast to epitaxially grown low-dimensional structures, however, LHP nanocrystals are synthesized in solution resulting in colloidal dispersions of nanocrystals stabilized by a ligand layer. The first such synthesis yielding fully inorganic LHP nanocubes was achieved by Protesescu et al. in 2015.[7] Since then, many different synthesis routes have been developed leading to dispersions of differently shaped nanocrystals with different numbers of confined dimensions.[8,63] Among those are nanoplatelets (NPLs), which are similar to 2D quantum wells. Their lateral dimensions, however, are also on the nanometer scale and can induce additional weak confinement on top of the strong confinement in the thickness dimension. This sets them apart from so-called Ruddlesden-Popper perovskites, which are two-dimensional slabs of perovskite separated by spacer ligands and can thus be seen as 2D quantum wells.[64,65] The thickness of both of these (quasi-)2D systems can be tuned with a monolayer (ML) precision down to a single ML for Ruddlesden-Popper perovskites and two MLs for the NPLs within this thesis. In this context a ML refers to a single layer of corner-sharing $[PbBr_6]$-octahedra with a thickness of around 0.6 nm. This high precision in size tuning within the strong confinement regime is unmatched by other LHP nanocrystal shapes and constitutes the basis for the results presented in this work. By carefully examining the dependence of specific properties on the NPL thickness, conclusions on the role of quantum confinement in LHP nanocrystals in particular and in nano-sized semiconductors in general can be drawn. In the following, LHP NPLs are introduced in detail.

The $CsPbBr_3$ NPLs, or more precisely $Cs_{n-1}Pb_nBr_{3n+1}$ NPLs, with n being the number of MLs, under investigation in this thesis were first developed by Bohn et al. in 2018.[10] One of the problems which the development of the NPLs was tackling was a lack of efficient nanocrystalline LHP light emitters in the blue spectral region. Due to an increase in the band gap induced by quantum confinement in very thin NPLs (see Subsection 2.1.5), the otherwise green light emission of $CsPbBr_3$ is shifted into the blue. This is schematically depicted in Figure 2.18. Previous attempts to obtain blue emission from LHP nanocrystals have often incorporated chloride as the halide, which drastically reduces the PLQY through the formation of deep trap states.[66] In the following, the optoelectronic properties of the $Cs_{n-1}Pb_nBr_{3n+1}$ NPLs are discussed, while their synthesis as well as a verification of their shape can be found in the Methods chapter in Section 3.1.

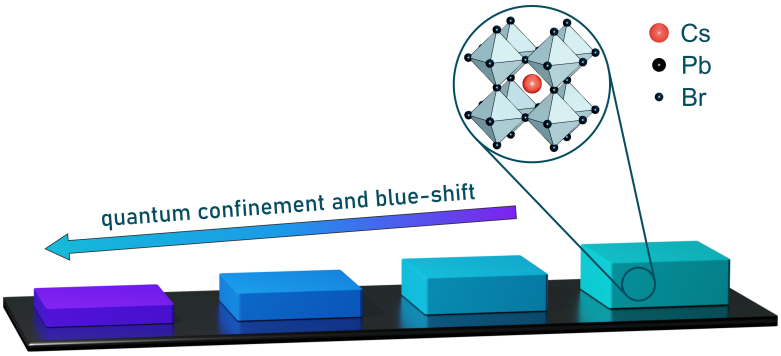

Figure 2.18: Thickness-Tunability of $Cs_{n-1}Pb_nBr_{3n+1}$ Nanoplatelets. Schematic representation of the material under investigation in this thesis. Quantum confinement in one dimension affects the band gap, thereby blue-shifting the emission spectrum with decreasing thickness.

Advantageous Optoelectronic Properties

Analogous to the section on bulk LHPs, the advantageous optoelectronic properties of $Cs_{n-1}Pb_nBr_{3n+1}$ NPLs are introduced here. For bulk LHPs the discussion of their properties was conducted on the basis of efficient solar cell operation. In contrast, LHP nanocrystals have demonstrated their highest potential in light-emitting devices. Therefore, some of the properties listed here are only advantageous in terms of light emission and can even be detrimental for light harvesting. The order in which the points are addressed is the following: (1.) First, the band gap tunability over a wide range is important, since the band gap determines the emission wavelength of a semiconductor. (2.) Second, high exciton binding energies are not a disadvantage like in solar cells and can also be tuned through a variation of the NPL thickness. (3.) Third, a high PLQY is required, which is tied to the recombination dynamics and in turn the exciton binding energy. (4.) Fourth, anisotropic light emission can enhance the photon outcoupling efficiency from a device.

1. Tunable Band Gap

Nanocrystals displaying some degree of quantum confinement enable the tuning of transition energies, i.e., emission wavelength through size variation. This is a powerful property, since wavelength shifts of the emission spectrum no longer have to be achieved solely by compositional changes and the parameter space for finding suitable materials increases drastically by employing nanocrystal size tuning. In the case of $Cs_{n-1}Pb_nBr_{3n+1}$ NPLs, a variable emission in the blue spectral range is achieved without halide exchange or the need for mixed-halide compositions eliminating phase segregation as a stability issue. Figure 2.19 displays the PL spectra of $Cs_{n-1}Pb_nBr_{3n+1}$ NPLs for thicknesses ranging from 2 ML to 6 ML. For comparison, the PL spectrum of weakly confined $CsPbBr_3$ nanocubes with an edge length similar to the NPLs' lateral size is shown. The spectral peak position ranges from 432 nm (2 ML) to 515 nm (nanocubes). Importantly, the spectra are all quite symmetric and narrow, supporting the hypothesis that the samples each comprise NPLs of only one thickness. This can be observed best in the 2 ML PL spectrum, since the spectral shift between the 2 ML and 3 ML PL spectra is the largest, due to the quantum confinement effect becoming progressively stronger with decreasing thickness. Thus, NPLs with a different thickness would lead to additional peaks in the 2 ML PL spectrum and the absence of such peaks points towards a high monodispersity in the thickness dimension.

2. Exciton Binding Energy

To determine the exciton binding energy experimentally, one can analyze the absorption onset of a sample with the Elliot model.[67,68] For larger exciton binding energies this gives reliable results. To this end, the absorption spectra of $Cs_{n-1}Pb_nBr_{3n+1}$ NPL and $CsPbBr_3$ NC dispersions are depicted in Figure 2.20 a. The energetic positions of the 1s exciton and the continuum onset are obtained through the Elliot model for each spectrum. To clarify the procedure, Figure 2.20 b shows the Elliot model fit for 2 ML NPLs in detail with the extracted 1s exciton and continuum onset positions. Furthermore, the energetic values of the two positions are plotted for all samples against NPL thickness in Figure 2.20 c on the black y-axis. In addition, the energetic difference between these two positions, the exciton binding energy E_B, is extracted for each NPL thickness and plotted on the red y-axis. In Subsection 2.1.5 it was already established theoretically that quantum confinement leads to an increase in exciton binding energy. This effect can be observed nicely in the NPLs. E_B reaches 280 meV in the 2 ML NPLs, which is nearly 10 times higher than the 30 meV measured for the weakly confined $CsPbBr_3$ nanocubes.

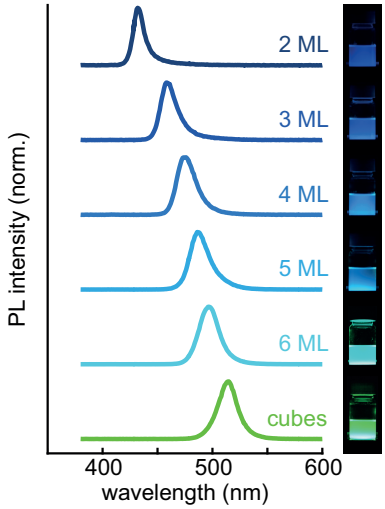

Figure 2.19: Photoluminescence Spectra of $Cs_{n-1}Pb_nBr_{3n+1}$ Nanoplatelets. The PL spectra of $Cs_{n-1}Pb_nBr_{3n+1}$ NPLs are plotted normalized in respect to the maximum of the PL intensity. The blue-shift with decreasing thickness down to 432 nm for 2 ML NPLs is clearly visible. For comparison, the PL spectrum of $CsPbBr_3$ nanocubes with an edge length similar to the NPLs' lateral size is also shown. Their emission maximum lies at 515 nm. Next to the spectra dispersions under UV light are depicted, which contain the respective nanocrystals. Adapted from Reference [10].

As pointed out in Subsection 2.1.5, pure quantum confinement in one dimension can only lead to a fourfold increase in E_B, which reveals that dielectric confinement also plays a large role here. Even the 6 ML NPLs possess an E_B above 80 meV. Since the exciton Bohr radius (for theory see Subsection 2.1.3) in $CsPbBr_3$ is around 7 nm,[69] all NPLs fall into the strong confinement regime. This is confirmed by the large PL emission shifts and strongly increased exciton binding energies. It shall be noted here that the increase in the band gap and the increase in E_B shift the PL emission wavelength in opposite directions. The overall blue-shift of the PL emission illustrates, however, that the increase in band gap dominates. The most important takeaway here is that E_B is at least three times larger than thermal energy at room temperature (26 meV) for all NPL thicknesses up to 6 ML. Thus, at room temperature and below, excitons govern the optoelectronic properties in $Cs_{n-1}Pb_nBr_{3n+1}$ NPLs after an initial relaxation on the femto- to picosecond timescale of the excited carriers into the excitonic states.[70] In particular, light emission stems predominantly from excitons rather than from free electrons and holes.

3. High Photoluminescence Quantum Yields

As established in the last paragraph, excitons dominate the recombination dynamics in LHP NPLs. Thus, the fraction of excitons decaying radiatively mainly determines the PLQY. It has been shown already for GaAs quantum wells and $MA_{n-1}Pb_nBr_{3n+1}$ NPLs that an increase in E_B caused by a decrease in well or NPL thickness leads to a faster radiative exciton decay.[9,71] Following Equation 2.18 a faster radiative decay should give rise to an increase in PLQY, if the non-radiative decay is not affected. Unfortunately, surface defects play also a large role in these ultrathin colloidal NPLs and the surface-to-bulk ratio increases with decreasing thickness. Consequently, the PLQY of the as-synthesized $Cs_{n-1}Pb_nBr_{3n+1}$ NPLs ranges from around 40 % for 6 ML NPLs to below 10 % for 2 ML NPLs. While this is not completely inefficient, it is still far from the PLQY of $CsPbBr_3$ nanocubes, which can be close to unity.[7] Furthermore, if the excitonic decay rates in all NPLs in a dispersion are similar and the excitation density is not too high, the total decay should be monoexponential. As can be seen from

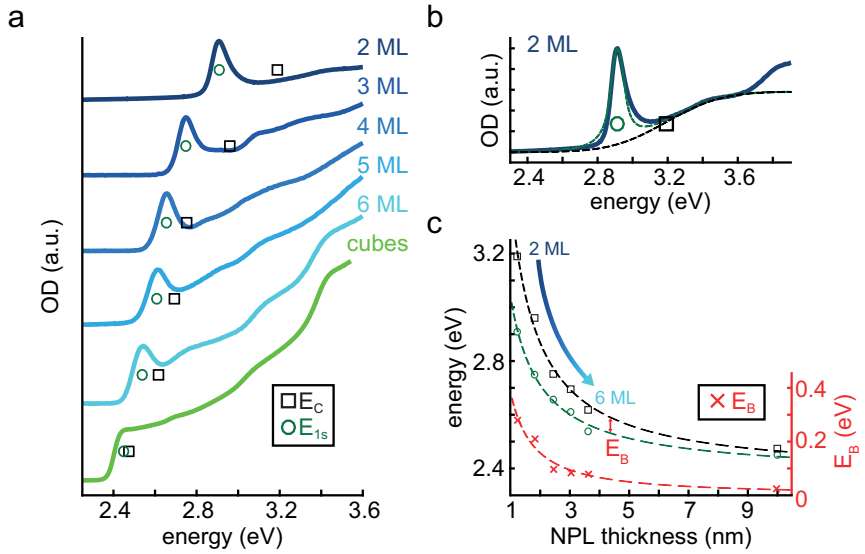

Figure 2.20: Absorption Spectra of $Cs_{n-1}Pb_nBr_{3n+1}$ Nanoplatelets. a) The absorption spectra of $Cs_{n-1}Pb_nBr_{3n+1}$ NPL and $CsPbBr_3$ NC dispersions are shown with the position of the 1s exciton (green circles) as well as the continuum onset (black squares) highlighted. These two properties are derived through fits of the absorption onset based on the so-called Elliot model. **b)** The Elliot model fit with (green dashed line) and without (black dashed line) excitonic contribution is displayed for the 2 ML NPLs. **c)** The resulting 1s exciton and continuum energies are plotted against NPL thickness on the first y-axis (black). Furthermore, the energetic difference of these two positions, the exciton binding energy E_B, is added with a second y-axis (red). Adapted from Reference [10].

the black curve in Figure 2.21 b, this is not the case. It follows that at least two different sub-ensembles must be present, one of those characterized by a much faster non-radiative decay channel. To tackle this issue, an additional surface-passivation step is introduced. By adding additional lead and bromide ions as well as ligands to the already formed NPLs, the defects can be repaired, which boosts the PLQY significantly, as presented in Figure 2.21. Additionally, the PL decay curve becomes monoexponential, demonstrating that all NPLs in the dispersion are now of a similar nature; an important prerequisite for the thickness-dependent studies in this thesis.

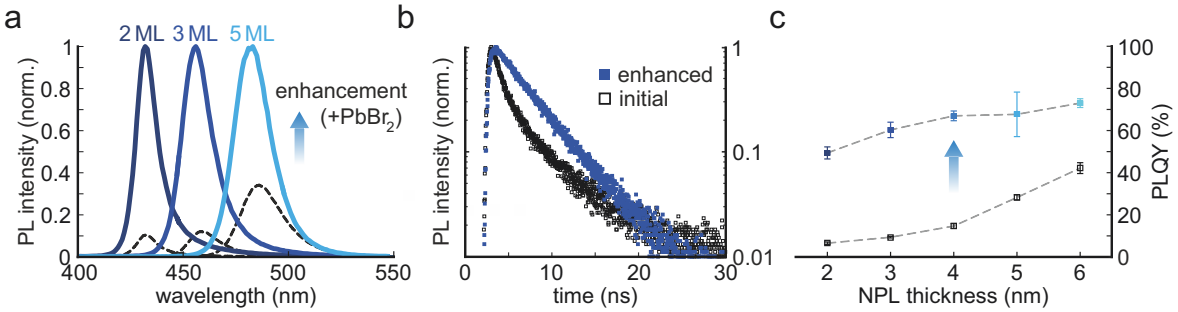

Figure 2.21: Enhancement of the Nanoplatelets. a) By adding an enhancement solution to the NPL dispersion upon synthesis, the PL emission intensity can be enhanced strongly. This results in **b)** a monoexponential decay on the one hand and **c)** an increased PLQY on the other hand. Adapted from Reference [10].

4. Shape Anisotropy

Another aspect setting NPLs apart from nanocubes, which must also be taken into account, is their shape anisotropy. Since the NPL thickness is well below the exciton Bohr radius for all NPLs, the probability distribution of the relative position of electron and hole should be anisotropic as well. This can even lead to a lifting of the degeneracy of the exciton fine structure mentioned in Subsection 2.1.3.

This is investigated in detail in the results part of this thesis. Among further implications, the shape anisotropy can also cause anisotropic light emission, which can be used to increase light outcoupling efficiency in devices.[72]

Disadvantageous Properties

Analogous to their bulk counterpart, LHP nanocrystals in general and LHP NPLs in particular suffer from different degradation mechanisms, which up to now prohibit their wide-spread commercialisation. Different approaches to overcome these stability issues include the encapsulation of single nanocrystals in protective shells or the search for more tightly bound ligands on the surface of the nanocrystals.[73,74] Another obstacle is the low conductivity of thins film consisting of LHP nanocrystals individually covered in ligand layers. Without achieving efficient electrical excitation, the LHP nanocrystals can only be employed as optically excited down converters delivering pure color.

3

Materials and Methods

In this chapter the synthetic routes for obtaining $Cs_{n-1}Pb_nBr_{3n+1}$ nanoplatelets and $CsPbBr_3$ nanocubes are introduced. Furthermore, since the resulting nanocrystals are dispersed in a solvent, the fabrication of thin films from the nanocrystal dispersions is discussed. A first characterization of the samples is usually conducted employing electron microscopy and room-temperature steady-state photoluminescence and absorption spectroscopy. Therefore, these techniques and some material-specific results are presented first. The main insights in this thesis, however, are drawn from data acquired with a temperature-dependent photoluminescence microscope. Building this setup, which allows for a spectrally or temporally resolved examination of the photoluminescence, was an essential step during the course of this thesis. In addition, some results were obtained with a transient absorption spectrometer, which allows for a better temporal resolution of ultrafast processes. This technique and the underlying physics are, thus, also explained.

3.1 Nanocrystal Synthesis and Characterization

The synthesis of the perovskite nanocrystals investigated within this thesis was mainly conducted by my colleagues Carola Lampe and Nina Henke. Here, the synthetic routes yielding $Cs_{n-1}Pb_nBr_{3n+1}$ NPLs and $CsPbBr_3$ nanocubes, respectively, are described. Table 3.1 lists all chemicals, which were purchased from *Sigma-Aldrich* and used in the syntheses.

Table 3.1: Chemicals Required for the Syntheses. All chemicals were purchased from *Sigma-Aldrich* and used as received. If the condensed formula of a compound is too long to be written down conveniently here, it is omitted.

Material	Condensed Formula	Purity
cesium carbonate	Cs_2CO_3	99 %
lead(II) bromide	$PbBr_2$	≥98 %
oleic acid	-	technical grade, 90 %
oleylamine	-	technical grade, 70 %
acetone	CH_3COCH_3	for HPLC, ≥99.9 %
toluene	$C_6H_5CH_3$	for HPLC, ≥99.9 %
hexane	$CH_3(CH_2)_4CH_3$	for HPLC, ≥97 %, GC
1-octadecene	-	technical grade, 90 %

3.1.1 $CsPbBr_3$ Nanoplatelets

The synthesis of the $Cs_{n-1}Pb_nBr_{3n+1}$ NPLs is based on the work by Bohn et al., 2018.[10] There are, however, some slight modifications. Nevertheless, the preparation of the precursors was not changed and is described first in the following.

Preparation of Precursors

The first precursor, Cs-oleate, is prepared by dissolving 0.1 mmol Cs_2CO_3 powder in 10 ml oleic acid at 100 °C under continuous stirring. The second precursor, a $PbBr_2$ ligand solution, is prepared by dissolving 0.1 mmol $PbBr_2$ and 100 µl each of oleylamine and oleic acid in 10 ml toluene at 100 °C under continuous stirring. The ligands improve the solubilization of $PbBr_2$ in toluene.

Enhancement Solution

This enhancement solution is already mentioned in the fundamentals part about the NPLs (see Subsection 2.4.2), as it is an important finding of the original NPL publication.[10] It is prepared by dissolving 0.1 mmol $PbBr_2$ and 100 µl each of oleylamine and oleic acid in 10 ml hexane at 100 °C under continuous stirring.

Synthesis

The synthesis itself is carried out at room temperature under ambient conditions. A vial is charged with the $PbBr_2$ precursor solution and the Cs-oleate precursor solution is added under stirring at 1200 rpm. The volume ratio of these two solutions determines the thickness of the resulting NPLs. Table 3.2 lists the volumes for the different NPL thicknesses. After 10 s, acetone, which acts as an antisolvent, is added. After 1 min of stirring, the mixture is centrifuged at 1800 g for 3 min and the

precipitate is redispersed in 1.8 ml hexane. To improve the stability as well as the quantum yield through the repair of surface traps, 200 µl of the enhancement solution are added immediately.

Table 3.2: Precursor and Acetone Amounts. The precursor and acetone amounts for achieving NPLs of different thicknesses are listed.

	$PbBr_2$ (ml)	Cs-oleate (µl)	Acetone (ml)
2 ML	3	150	2
3 ML	1.5	150	2
4 ML	1.3	150	2
5 ML	1.2	150	2
6 ML	1	150	2
8 ML	0.8	150	2

3.1.2 $CsPbBr_3$ Nanocubes

The synthesis of the $CsPbBr_3$ nanocubes is carried out following the work by Tong et al., 2016.[75] First, 0.5 ml each of oleylamine and oleic acid are mixed with 10 ml of 1-octadecene. Next, 0.1 mmol Cs_2CO_3 and 0.3 mmol $PbBr_2$ are added and the reaction medium subjected to tip sonication at a power of 30 W for 10 min. Afterwards the dispersion is centrifuged at 9000 g and the NC precipitate is redispersed in 5 ml hexane. The dispersion is centrifuged again at around 450 g to remove larger crystals and this time the supernatant is kept, which contains the $CsPbBr_3$ nanocubes.

3.1.3 Film Formation

Both of the investigated nanocrystal shapes, $Cs_{n-1}Pb_nBr_{3n+1}$ NPLs and $CsPbBr_3$ nanocubes, are present in colloidal dispersions upon synthesis. Since a dispersion would introduce complications when cooling it down to liquid helium temperatures, the measurements in this thesis are usually conducted on films comprising these nanocrystals. Whereas devices in particular often require thin films with a high homogeneity in thickness, thick films are beneficial for most of the measurements conducted here, as they provide a high PL intensity due to a large ensemble of nanocrystals in the excited volume. Furthermore, in a thick film the nanocrystals should be randomly oriented. Especially for the NPLs this helps to exclude that only part of the non-isotropic light emission is measured, which could occur, if, e.g., all NPLs in the probed volume lie face up.[72] Thus, drop-casting is chosen for film formation in most experiments, which produces less homogeneous but thicker films. To suppress influences of the substrate on the charge carrier dynamics, silicon substrates with a 300 nm oxide top layer acquired from *SIEGERT WAFER* are used. This ensures that free electrons and holes or excitons created within the nanocrystal layer are not able to transfer into the substrate material.

3.1.4 Electron Microscopy

Besides a spectroscopic characterization of the synthesis products, electron microscopy is employed to verify that the nanocrystals possess the expected shape. Therefore, 25 µl were drop-casted onto transmission electron microscopy (TEM) grids coated with Formvar (10 nm) and carbon (1 nm) acquired from *Electron Microscopy Sciences*. Electron microscopy is conducted either with the transmission electron microscope JEM-1011 (from *JEOL*) at an operating voltage of 80 kV or for a higher resolution

with the scanning transmission electron microscope Titan Themis (*Thermo Fisher Scientific*) in high-angle annular dark field (STEM-HAADF) mode at an operating voltage of 300 kV.

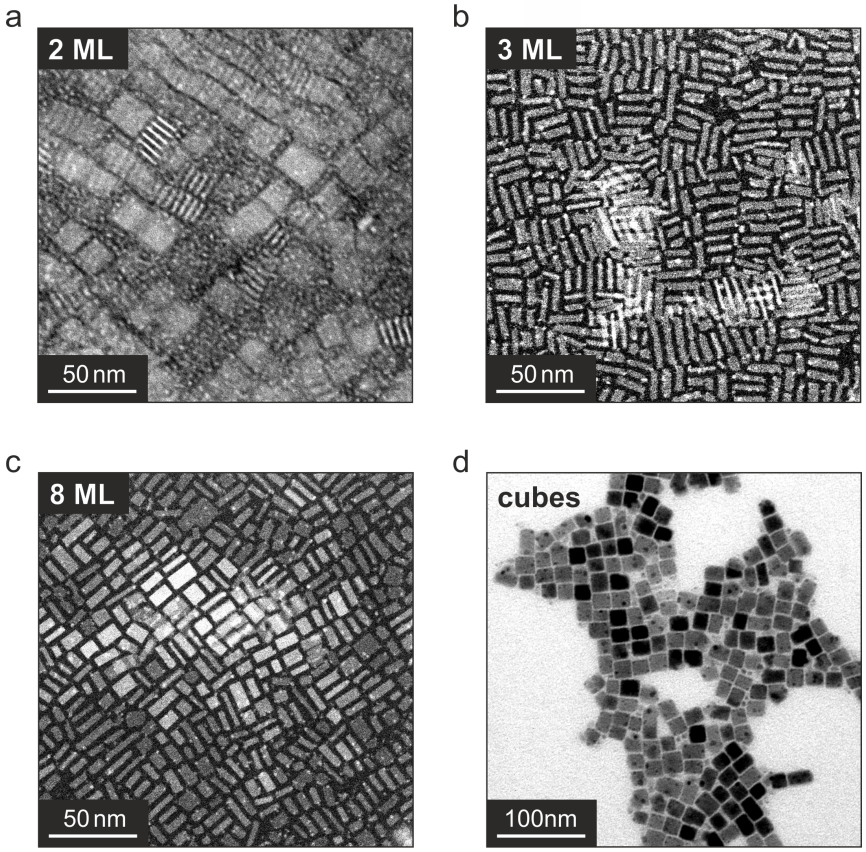

Figure 3.1: Electron Microscopy Images. STEM-HAADF images of **a)** 2 ML, **b)** 3 ML and **c)** 8 ML cesium lead bromide NPLs. **d)** A TEM image of cesium lead bromide nanocubes.

Figure 3.1 depicts STEM-HAADF images of 2 ML, 3 ML and 8 ML NPLs as well as a TEM image of the nanocubes. Especially in Figure 3.1 b all NPLs are in stacks and standing on their side. Employing these images, an evaluation of the size of 50 different nanoplatelets from each NPL sample measured in STEM-HAADF is presented in Table 3.3. This includes all thicknesses shown in Figure 3.1 a-c as well as 5 ML NPLs. This analysis reveals similar lateral sizes of around 14 nm for all NPL samples as well as a high homogeneity in terms of NPL thickness within a sample. Only for thicker NPLs this homogeneity starts to decrease, as can be seen in Figure 3.1 c. Furthermore, Figure 3.1 d discloses that the edge length of the nanocubes is comparable to the lateral size of the NPLs.

Table 3.3: Size Analysis. Analyzing 50 nanocrystals from multiple STEM-HAADF images gives an average value for the thickness d and the lateral sizes L_x and L_y as well as the respective standard deviations σ. The value L_y can only be extracted for the 2 ML NPLs, since some of the NPLs are lying face-down. In the other films all NPLs are standing on their side.

	d (nm)	σ(d) (nm)	L_x (nm)	$\sigma(L_x)$ (nm)	L_y (nm)	$\sigma(L_y)$ (nm)
2 ML	1.5	0.2	14.0	1.6	16.4	2.7
3 ML	2.5	0.5	15.1	4.3		
5 ML	3.3	0.6	14.9	2.4		
8 ML	4.5	1.1	12.6	3.5		

Since the thickness should increase in increments of 0.59 nm, which corresponds to one layer of unit cells, it seems the analysis of the STEM-HAADF images slightly overestimates the thickness. Thus,

further characterization is required to corroborate the NPL thickness assignments to the different samples. The small standard deviation in thickness stemming from a high homogeneity, however, can already be seen nicely in the electron microscopy images.

3.1.5 Optical Characterization

Steady-state absorption and PL of the synthesized dispersions was measured with a FluoroMax-PLUS spectrometer acquired from *HORIBA Scientific*, which is equipped with the optional absorbance/transmission accessory. The processes governing the absorptive and emissive properties of semiconductor nanocrystals were introduced in Subsection 2.2.1 and Subsection 2.2.2, respectively. Since these properties are tied to the band structure of the semiconductor, their measurement can help characterize the NPLs in terms of thickness and monodispersity upon synthesis. Only if this first optical characterization of a dispersion reveals a high monodispersity for NPLs of a fixed thickness, the sample is considered for further experiments.

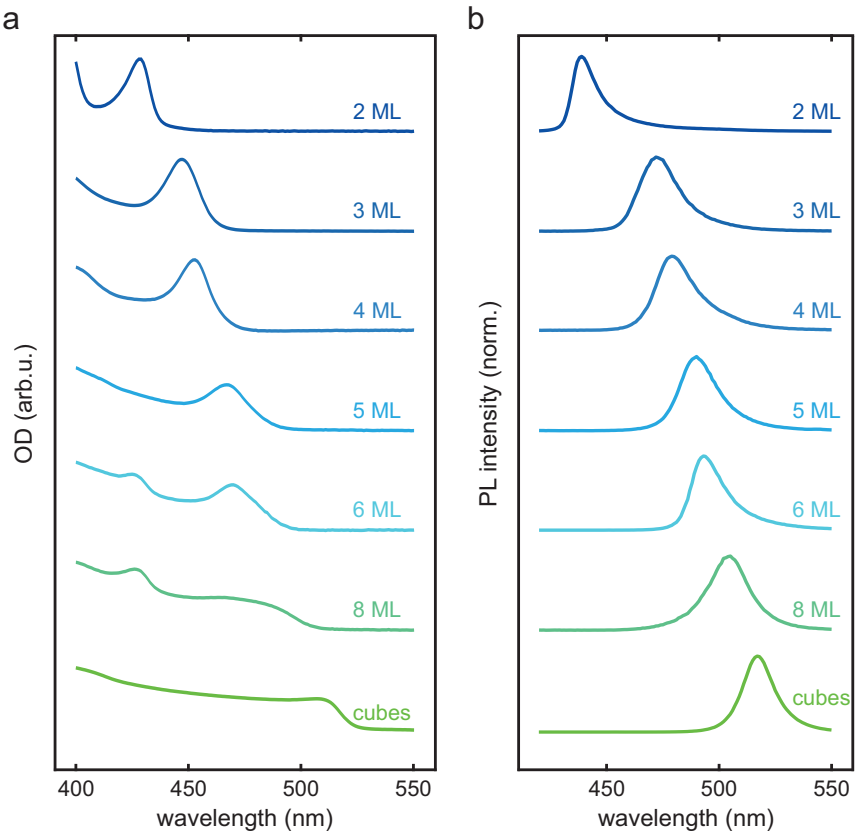

Figure 3.2: Absorption and Photoluminescence of Dispersions. a) The OD and **b)** the PL spectrum of $Cs_{n-1}Pb_nBr_{3n+1}$ NPLs of different thickness and $CsPbBr_3$ nanocubes are displayed. The PL and absorption onset blue-shift with decreasing thickness caused by an increase in quantum and dielectric confinement. Furthermore, with decreasing thickness an excitonic absorption feature mainly stemming from direct 1s exciton absorption becomes more pronounced.

Some spectra in this thesis are just termed absorption spectra. The property, however, that is actually measured is absorbance or optical density (OD). To calculate the OD of a dispersion, the intensity of the incident light from a broadband white-light source $I_0(\lambda)$ and the intensity of the transmitted light $I(\lambda)$ have to be measured. The $OD(\lambda)$ is then obtained by:

$$OD(\lambda) = -log_{10}\frac{I(\lambda)}{I_0(\lambda)} \tag{3.1}$$

Figure 3.2 depicts absorption and PL spectra of $Cs_{n-1}Pb_nBr_{3n+1}$ NPLs of different thickness and $CsPbBr_3$ nanocubes measured in dispersion. Such spectra are acquired after each synthesis to assess the quality of the sample. The PL spectrum as well as the absorption onset blue-shift with decreasing thickness and an excitonic absorption feature becomes more pronounced. These effects are a direct consequence of the increase in E_G and E_B caused by quantum and dielectric confinement and introduced in Subsection 2.1.5.

Combining these spectra with electron microscopy images and the information published by Bohn et al.,[10] NPL thicknesses can be assigned unambiguously. Furthermore, the spectral PL shift between 2 ML and 3 ML NPLs is large enough so that NPLs of the respective other species would cause an additional peak. The absence of such a peak confirms the conclusions drawn from the electron microscopy images that the monodispersity in thickness is quite high in these samples and that slight asymmetries in the PL peaks rather stem from not perfectly defined lateral sizes.

3.2 Temperature-Dependent Photoluminescence

A PL microscope was the most important tool for acquiring data on the excitonic properties of the nanocrystals within this thesis. In literature this is sometimes also termed a micro-PL setup, if the spatial resolution is very high. I designed and built two versions of such setups during the course of this thesis. The first version is quite compact and the substrate with the nanocrystal film is exposed to ambient conditions. The second one is built around a cryostat and enables the variation of sample temperature down to 5 K. For simplicity, only this second version is introduced here, since the functionality, operation and components are essentially the same and the most crucial data was acquired with this setup. A schematic of the full setup can be seen in Figure 3.3. All optomechanical components as well as lenses were purchased from *Thorlabs Inc.* Optical filters and dichroic mirrors were either purchased from *Chroma Technology* or *Semrock*. Furthermore, as the focusing and PL collecting objective, different options in terms of magnification and numerical aperture were obtained from *Nikon Metrology* and *Mitutoyo*. In the following, the setup is described in detail by differentiating between sections with specific functions.

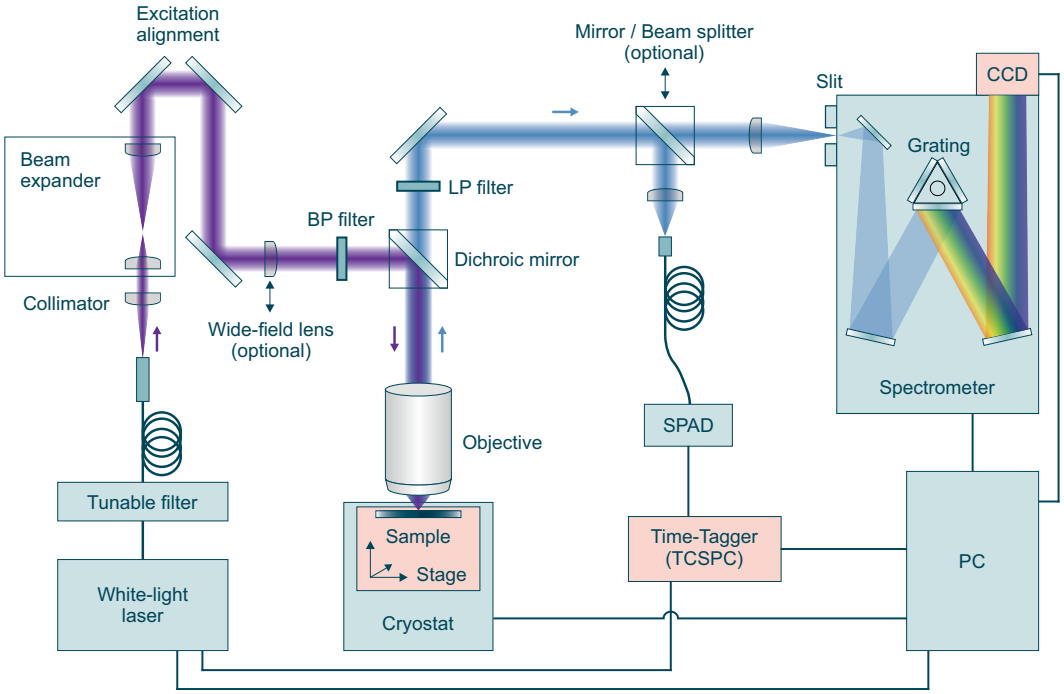

Figure 3.3: Micro-Photoluminescence Setup. Schematics of the micro-PL setup displaying the most important optical components and devices controlled by a computer. This setup exists in two versions with one of those able to vary the sample temperature in a cryostat.

3.2.1 Excitation Source

The optical part of this setup can be divided into an excitation pathway and a signal pathway. As the excitation section is rather generic and independent of how the PL signal is examined in the second part of the setup, it is introduced here separately. Generally, such an excitation configuration, as depicted in Figure 3.4, can also be found in other setups where optical excitation is required.

The excitation light is generated by the supercontinuum white light laser SuperK FIANIUM FIU-15 from *NKT Photonics*. In this system the narrow spectrum of a pulsed seed laser (repetition rate of

78 MHz) is strongly broadened in a supercontinuum fiber by a number of non-linear optical effects. These effects involve, e.g., self-phase modulation, Raman scattering, phase matching and solitons and result in a broad spectrum from 390 nm to 2400 nm, while the pulsed nature with a pulse length of a few tens of picoseconds is retained. Combining this system with a SuperK VARIA tunable filter (*NKT Photonics*), any wavelength interval between 10 nm and 100 nm in width and located between 400 nm and 840 nm can be filtered from the white light spectrum and employed as excitation light. In essence, this powerful combination results in a wavelength-tunable pulsed laser source. Since the light is subsequently delivered via another glass fiber to the setups, it can also be switched easily between applications.

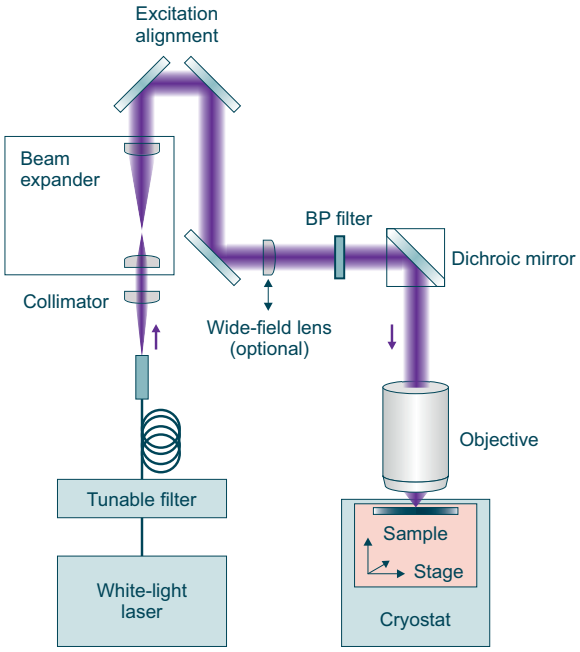

Figure 3.4: Optical Excitation Pathway. The configuration used for the optical excitation of the sample. This is a common build and can be found in different setups drawing data from PL.

Upon exiting the fiber the beam is slightly divergent so it is collimated by a lens. Then, its diameter is expanded so that the first lens of the objective is fully illuminated, which allows for better focusing of the beam. To separate the excitation light from the PL later on, the last mirror prior to the objective is a dichroic longpass (LP). Optionally, a wide-field lens can be flipped into the beam. Without it the focal planes of excitation and emission after the objective are equal, since the objective is an apochromat and the setup infinity-corrected. Thus, only a very small area determined by the diffraction-limited diameter of the focused laser is excited. To observe a wide-area PL image or decrease the excitation intensity at a fixed excitation power the wide-field lens is flipped in, which shifts the focal plane of the excitation and, thus, excites a larger sample area.

The sample itself sits inside an attoDRY 800 closed cycle cryostat on top of an xyz-nanopositioner stage, both acquired from *attocube systems*, which allows for sample temperatures from 5 K to 300 K.

3.2.2 Steady-State Photoluminescence

The PL emitted from the sample is collected by the same objective employed for directing the laser beam onto the sample. A schematic of this can be seen in Figure 3.5. The dichroic longpass (LP) is chosen in such a way that its transmission at the wavelength of the PL is high. An additional LP filter

ensures that scattered laser light is completely blocked and only signal light can travel towards the detection devices.

For steady-state PL detection the light is guided into an HRS-500 spectrometer from *Teledyne Princeton Instruments*. Its grating turret can also be set to a mirror. In this case and with the sample in focus, a PL image can be observed on the PIXIS CCD camera (also *Teledyne Princeton Instruments*). Hence, this detection option is responsible for the setup being termed a PL microscope.

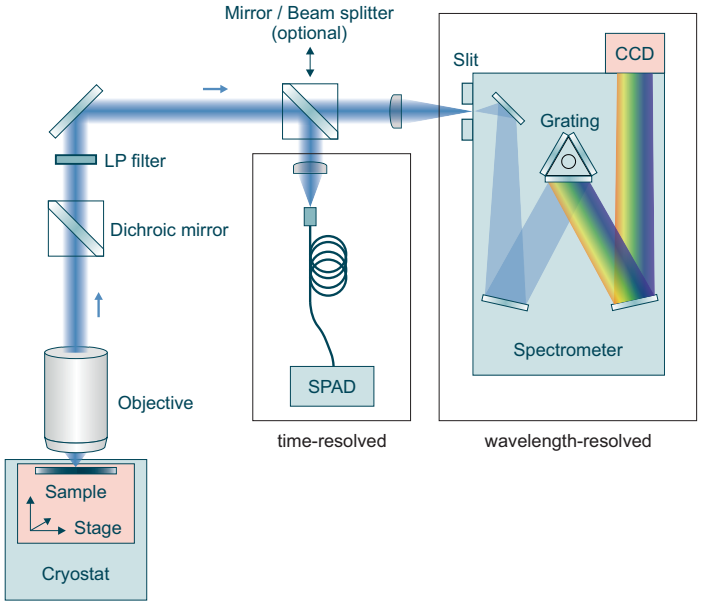

Figure 3.5: Optical Detection Pathway. The PL signal can be directed towards two different types of measurements in this setup. On the one hand, a spectrometer allows for wavelength-resolved measurements and, on the other hand, a TCSPC unit enables time-resolved PL decay measurements.

By closing the entrance slit to 80 µm and using a grating instead of the mirror, the PL is resolved spectrally with the CCD camera. In this configuration, a steady-state PL spectrum can be acquired. Here, the term steady-state is used to set the wavelength-resolved measurement apart from time-resolved measurements on a nanosecond timescale, which are introduced in the next section. Since the representation of a PL spectrum on an energy axis is in many cases more relevant than on a wavelength axis and is often employed in this work, it shall be discussed here briefly. Due to the inverse relationship between wavelength and energy only an energy scale allows for a convenient comparison of energetic peak widths or other energetic spacings between certain spectral features. This inverse relationship, however, has to be also taken into account when transforming between the two representations. It is described nicely by Mooney et al. and summarized here.[76]

Jacobian Conversion of Scales

The relation between wavelength and energy of a photon is:

$$E_{\mathrm{ph}} = \frac{hc}{\lambda} \tag{3.2}$$

This relation can be used to convert the axis values from wavelength to energy. The corresponding PL intensity values, however, are recorded in constant wavelength intervals $d\lambda$ in a spectrometer. From energy conservation it follows:

$$I(E)dE = I(\lambda)d\lambda \tag{3.3}$$

Combining those two relations, one arrives at:

$$I(E) = I(\lambda)\frac{d\lambda}{dE} = I(\lambda)\frac{d}{dE}\left(\frac{hc}{E}\right) = -I(\lambda)\frac{hc}{E^2} \tag{3.4}$$

While the minus only encodes the direction of integration, the factor $\frac{hc}{E^2}$ is important. When converting data recorded in units of wavelength to an energy representation, the intensity values have to be scaled with that factor to account for the inverse relationship of energy and wavelength of a photon.

3.2.3 Time-Resolved Photoluminescence

The first prerequisite for time-resolved PL (TR-PL) measurements is the pulsed nature of the laser described above with a pulse length of a few tens of picoseconds. Following each pulse the generated excitons or electron-hole pairs recombine over time and emit photons over that period, as the sample relaxes back into the ground state.

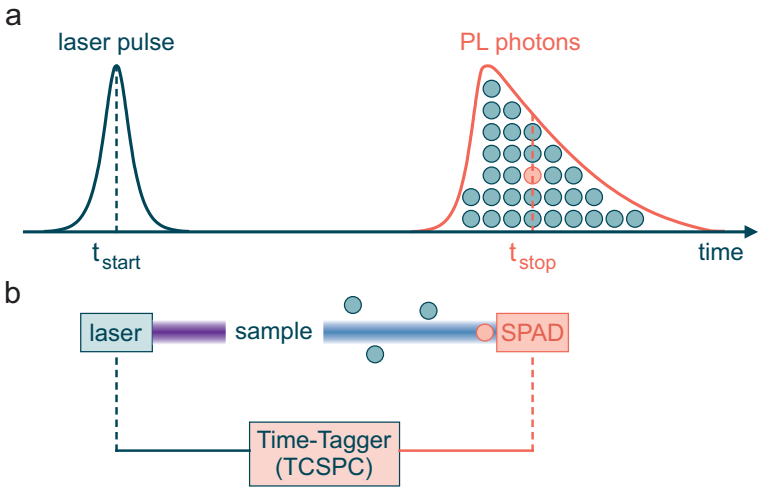

Figure 3.6: Time-Resolved Single Photon Counting. a) Schematic representation of one photon detection event in a TCSPC setup and **b)** the corresponding setup configuration.

To gain insight on the temporal distribution of these emitted photons and, thus, on the decay dynamics within the semiconductor sample, time-correlated single photon counting (TCSPC) is employed. For this the sample PL is focused onto a single-photon avalanche diode (SPAD / SPCM-AQRH from *Excelitas Technologies*), which sends an electronic trigger signal to a time-to-digital converter (Time Tagger 20 from *Swabian Instruments*) once it detects a photon. This stops a very fast stopwatch that is started by a trigger signal at the moment of laser pulse emission, as visualized in Figure 3.6. Since the SPAD allows for only one detection event following one laser pulse, the time difference $\Delta t = t_{\text{stop}} - t_{\text{start}}$ is added as one count in a histogram and the process is repeated over many laser pulses. The probability to detect a photon stemming from a certain time of the decay is proportional to the number of photons emitted at that time so that the histogram resembles the PL emission dynamics within the sample after enough detection events. Multiple photons reaching the SPAD following one laser pulse has to be avoided, as only the first photon is detected. If this scenario occurs in a high fraction of detection events, early photons are overrepresented in the histogram resulting in the so-called pile-up effect.

Thus, the signal has to be attenuated by neutral density filters until the SPAD detection rate is one hundred times smaller than the laser repetition rate meaning that only one photon is detected for every one hundred laser pulses. The resulting TR-PL decay curve is temporally offset by the time it takes the photons to travel through the setup as well as a possible difference in length of electronic signal paths. When such data is displayed in the results part of this thesis, however, the maximum of the PL decay curve is generally set to zero in time.

3.3 Transient Absorption Spectroscopy

An investigation of excitonic processes, which take place on timescales well below one nanosecond, is not possible with TCSPC. This is a result of both the temporal extension of the laser pulses and the electronics involved, which are not able to resolve time differences once they become too small. To achieve even better resolution in time, one has to turn to optical techniques relying on ultrashort laser pulses, which are not limited by electronic responses. One such technique is transient absorption spectroscopy (TAS), sometimes also termed differential transmission spectroscopy (DTS). In such an experiment, also called pump-probe experiment, excitations within the sample are generated by a pump pulse and subsequently investigated by a probe pulse. Through a variation of the delay between those two pulses the temporal evolution of the excited population is resolved. The technique is explained in detail in the following.

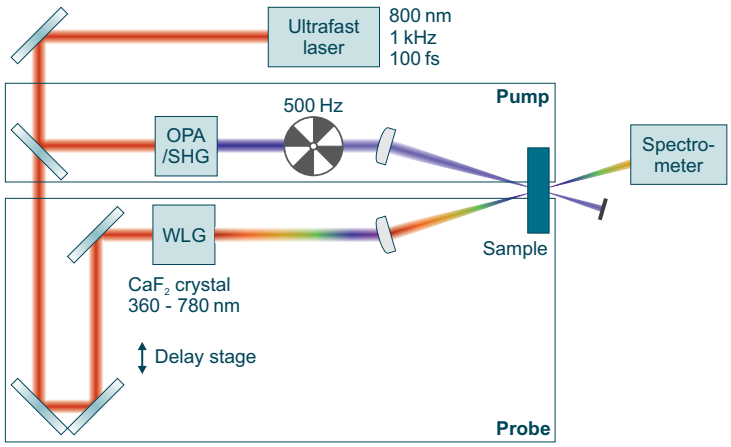

Figure 3.7: Transient Absorption Spectrometer. Schematic representation of the TAS experimental setup. An insight into ultrafast exciton dynamics is gained through exploiting ultrashort laser pulses with a temporal extension on the order of 100 fs.

The laser pulses in the TAS setup are generated by a Libra-HE$_+$ system, which combines a Vitesse seed laser with an Evolution pump laser (all from *Coherent, Inc*). Employing optical pulse compression, it is able to emit pulses of a temporal extension of around 100 fs centered at 800 nm with a pulse energy of 5 mJ and a repetition rate of 1 kHz.

The TAS system itself is designed and assembled by *Newport Inc.* Within the setup, as a first step, the laser beam is split by a beam splitter. Then, the two resulting laser beams travel on different paths through the setup and overlap again within the sample volume, as depicted schematically in Figure 3.7. One of those beams, the so-called probe, passes through a CaF_2 crystal. This white light generation (WLG) step broadens the spectrum significantly by means of various non-linear optical processes, resulting in a spectrum covering wavelengths from 360 nm to 780 nm. Subsequently, the beam is directed through the sample and the spectrum of the transmitted light is measured by an MS260i spectrometer from *Newport Inc.* Naturally, this spectrum represents the generated white light minus the light absorbed by the sample.

The second pulse, the so-called pump, is used to generate an exciton population, the decay of which is then probed in the experiment. Since the photons in the 800 nm laser pulse do not carry enough energy to overcome the band gap in the nanocrystals under investigation, the pulse is frequency doubled through second harmonic generation (SHG). Alternatively, an optical parametric amplifier

can be used to produce other excitation wavelengths. In this thesis, however, the second harmonic of the Libra-HE$_+$ laser is always employed. Furthermore, the pump beam is chopped with a frequency of 500 Hz so that only every second pump pulse reaches the sample. Thus, every second probe pulse experiences an altered absorption/transmission, which is modified by the excitations in the probed sample volume. The ratio between the transmitted probe light with and the transmitted probe light without pump pulse is influenced by the generated excitons or free electrons and holes through a number of mechanisms. Most notably, the absorption of the sample is decreased, if excited states are already occupied. This is connected to Fermi's golden rule (see Equation 2.15), which introduces a linear relation of the absorption of a semiconductor to the number of initial and final states with the energetic spacing of a specific photon energy. Already occupied final states or empty initial states cannot contribute to absorption resulting in a decreased absorption at associated wavelengths compared to a sample in thermodynamic equilibrium. This effect is also termed a bleaching of those states. By varying the temporal delay between the pump and the probe pulse the dynamics upon excitation, e.g., the decay of excitons, can be resolved. This is achieved through controlling the optical path length of the probe pulse by moving a retroreflector mounted on a linear stage. The temporal resolution of this setup is then only determined by the temporal extension of the laser pulse ($\approx$ 100 fs), as the smallest step size of the stage relates to below 1 fs of change in the delay. The maximum delay possible is 3 ns rendering the setup unsuitable for the investigation of slower dynamics.

The quantity, which is usually plotted throughout the thesis, is $\Delta T(\lambda)/T(\lambda)$, the relative change in transmission. Here, $\Delta T(\lambda)$ equals to $T^*(\lambda) - T(\lambda)$ with $T^*(\lambda)$ being the transmission of the excited sample and $T(\lambda)$ the transmission of the sample in thermal equilibrium. This quantity is calculated for every two subsequent laser pulses, which is equal to once every two milliseconds. The signal, however, is averaged for a few seconds at every pulse delay to reduce noise. Naturally, the spectrometer actually measures just the spectrum of the probe pulse after the excited and non-excited sample $I^*(\lambda)$ and $I(\lambda)$. The ratio between those, however, is equal to the ratio of the transmission spectra, since the spectrum of the probe pulse before the sample $I_0(\lambda)$ cancels out:

$$\frac{\Delta I(\lambda)}{I(\lambda)} = \frac{I^*(\lambda) - I(\lambda)}{I(\lambda)} = \frac{\frac{I^*(\lambda)}{I_0(\lambda)} - \frac{I(\lambda)}{I_0(\lambda)}}{\frac{I(\lambda)}{I_0(\lambda)}} = \frac{T^*(\lambda) - T(\lambda)}{T(\lambda)} = \frac{\Delta T(\lambda)}{T(\lambda)} \tag{3.5}$$

Furthermore, taking into account Equation 3.1, $\Delta T(\lambda)/T(\lambda)$ can also be expressed in terms of the change in optical density of the sample caused by the excited carriers:

$$\frac{\Delta T(\lambda)}{T(\lambda)} = \frac{T^*(\lambda) - T(\lambda)}{T(\lambda)} = \frac{T^*(\lambda)}{T(\lambda)} - 1 = \frac{10^{-OD^*(\lambda)}}{10^{-OD(\lambda)}} - 1 = 10^{-\Delta OD(\lambda)} - 1 \tag{3.6}$$

While there are different ways in which the generated charge carriers can alter the OD of a semiconductor sample, e.g., band gap renormalization, induced absorption or even stimulated emission, the feature of interest in this thesis is the exciton bleaching peak. It stems from the effect already described above that present excitons decrease the direct absorption of photons in resonance with the respective exciton level. For $\Delta OD(\lambda)/OD(\lambda) < 0.1$ at the excitonic absorption peak the relation between the size of the exciton population and $\Delta T(\lambda)/T(\lambda)$ at that spectral position can be approximated as linear and in that case TAS is a powerful tool to measure the decay of excitons on an ultrafast time scale.

Lastly, the dispersions measured in this setup are diluted to low OD values at the excitation wavelength of 400 nm to ensure a spatially homogeneous excitation over the whole path length of the cuvette.

4

Exciton Fine Structure

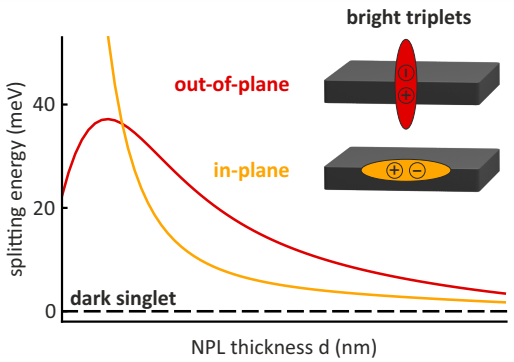

This chapter introduces and analyzes the exciton fine structure of $Cs_{n-1}Pb_nBr_{3n+1}$ NPLs with a particular focus on the thickness- and, thus, confinement-dependence of the energetic splitting. Notably, the strong shape anisotropy of the NPLs induces an energetic splitting of the bright exciton states into in-plane and out-of-plane excitons, both of which are significantly split from a lowest lying dark excitonic level, which affects the PL decay dynamics drastically at low temperatures. To explain the results theoretically, an effective mass model taking into account quantum as well as dielectric confinement is developed, which matches the low-temperature PL data nicely. The measured bright-dark splitting reaches 32.3 meV for the 2 ML NPLs. This constitutes the largest splitting of those states observed in any semiconductor system to date. Combining the strong thickness-dependence of these properties with the newly developed model, these results can help to advance our understanding of excitons in strongly quantum-confined and anisotropically shaped semiconductors. The results and all figures presented in this chapter have been published in Advanced Science in 2022 [77].

4.1 Temperature-Dependent Photoluminescence

The basis for all experiments in this thesis is a precise synthesis and a basic characterization of the $Cs_{n-1}Pb_nBr_{3n+1}$ NPLs, which includes a verification of the homogeneity of the samples. Since this routine applies to all result chapters, all of the information and background on synthesis and basic characterization of the NPLs consisting of electron microscopy, PL and absorption measurements can be found in Section 3.1. A general background on the $Cs_{n-1}Pb_nBr_{3n+1}$ NPLs discussing previously published results with a focus on quantum confinement effects on the band gap and the exciton binding energy can be found in Subsection 2.4.2.

Prior to this thesis, all of the investigations of the NPLs were conducted at room temperature. A first suspicion that the strongly quantum confined $Cs_{n-1}Pb_nBr_{3n+1}$ NPLs could possess a fine structure splitting between a bright excitonic level and a lower lying dark excitonic level stemmed from 2 ML PL and TR-PL data acquired at low temperature down to 5 K. For those measurements, the NPLs were drop-casted onto a silicon substrate and cooled to cryogenic temperatures in the micro-PL setup introduced in Section 3.2. A large ensemble of NPLs resides in the excitation volume during a PL measurement of such a film, rendering inhomogeneous broadening (see Subsection 2.2.5) the main contributor to the PL linewidth at 5 K.

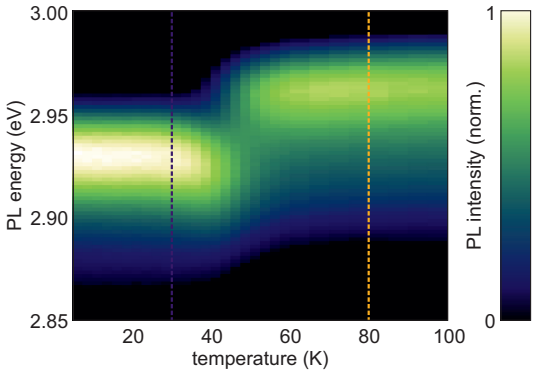

Figure 4.1: Low-Temperature Photoluminescence of 2 ML Nanoplatelets. PL map comprising PL spectra of 2 ML NPLs acquired in 2.5 K steps from 5 K up to 60 K and in 5 K steps from 60 K up to 100 K.

Figure 4.1 depicts the temperature-dependent PL emission of 2 ML NPLs between 5 K and 100 K for an excitation wavelength of 400 nm. While this excitation generates free electron-hole pairs, the emission should stem nearly exclusively from excitons, considering the high exciton binding energies in NPLs (around 280 meV for $Cs_{n-1}Pb_nBr_{3n+1}$ 2 ML NPLs), the fast relaxation times of hot carriers and the low temperature. Surprisingly, a large shift in the PL photon energy occurs between 40 K and 55 K. This shift is reproducible for different 2 ML NPL samples as well as reversible in both temperature directions. Such a sudden shift is sometimes observed in other perovskite compositions at low temperatures and is in that case connected to a phase change of the crystal structure, as discussed in Subsection 2.4.1. For this composition, however, phase changes from the orthorhombic to a tetragonal (88 °C) and finally cubic (130 °C) crystal structure were found to occur above room temperature.[45] Even if the NPL shape influences these transition temperatures to a certain degree, it is highly unlikely to find such a transition at around 50 K. We recently corroborated this through room temperature grazing incidence wide angle x-ray scattering (GIWAXS) measurements, which revealed an orthorhomic crystal structure of the NPLs.

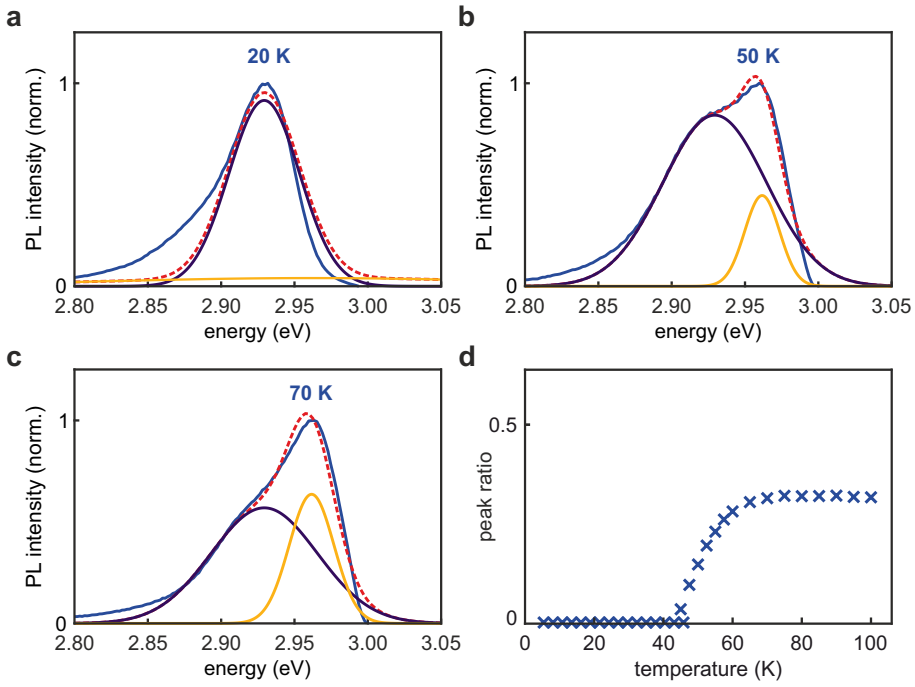

Figure 4.2: Double Gaussian Fit. a)-c) The measured spectra of the 2 ML NPLs (blue lines) during the spectral shift can be reproduced by two Gaussians. The individual Gaussians are shown as purple and yellow lines and their sum as a dashed red line, which describes the measured spectra reasonably well for each temperature. Both of the Gaussians are fixed to the same energetic position for all temperatures. This shows that the effect is not a gradual shift of the spectrum with temperature but rather a decreasing emission at one photon energy accompanied by an increasing emission at another. The use of Gaussian distribution functions is justified by inhomogeneous broadening being the main contributor to total spectral broadening at these temperatures (see Subsection 2.2.5). **d)** The integral of the high energy Gaussian divided by the integral over the sum of both Gaussians reveals an activation behavior of the high energy Gaussian.

Investigating the spectral shift more precisely, one finds that the spectra in the transition range can be reproduced quite nicely by the sum of two Gaussians with an energetic spacing of 32.3 meV, as depicted in Figure 4.2. Moreover, the two Gaussians can be fixed to the same two energetic positions for all temperatures and still fit all the spectra convincingly, as the spectral shift is described well by a shifting of the the weight from the low energy Gaussian to the high energy Gaussian with increasing temperature. This effect is illustrated in Figure 4.2 d by plotting the ratio between the integral over high energy Gaussian and the integral over the sum of both Gaussians.

To further unravel the origin of this spectral shift of the emission, one has to turn to the TR-PL decay dynamics at temperatures below and above the shift. Accordingly, Figure 4.3 a depicts two PL spectra of 2 ML NPLs at 30 K and 80 K with their energetic maxima split by 32.3 meV, while Figure 4.3 b contains the corresponding TR-PL curves acquired with the TCSPC technique introduced in Subsection 3.2.3.

Interestingly, a clear difference in the TR-PL curves between temperatures below and above the spectral shift can be observed. At 30 K, the decay comprises two distinctly different components: The first is a very fast decay component not resolvable by the temporal resolution of the setup (see Subsection 3.2.3), which has, thus, a lifetime $\tau_{\text{fast}} < 600\,\text{ps}$. The second is characterized by a significantly longer lifetime $\tau_{\text{slow}} > 1\,\mu\text{s}$. This behavior strongly points towards two different energetic levels involved in the decay. If the decay of the energetically lower level via emission of a photon is dipole forbidden and, thus, quite slow yet there is no competing faster non-radiative decay mechanism, then its PL emission can still be efficient and detectable, resulting in a large contribution to the steady state PL spectrum.

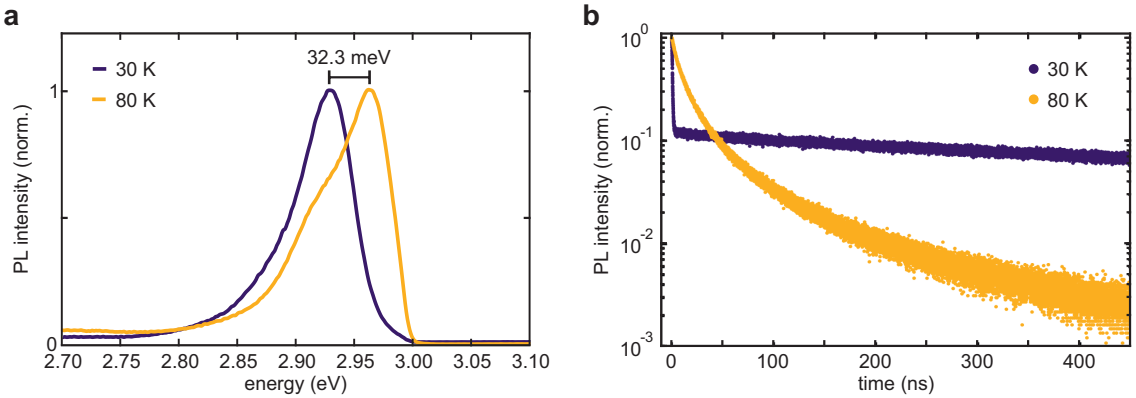

Figure 4.3: Photoluminescence Spectra and Decay. a) PL spectra of 2 ML NPLs at 30 K (dark blue) and 80 K (yellow) and **b)** the corresponding TR-PL curves at the respective temperatures.

Furthermore, at very low temperatures the probability for the thermal activation of an exciton into the higher level is near zero and the fast initial decay stems from the exciton population occupying the higher level at $t = 0$, which decays either radiatively or transfers into the lower level. Here, it is generally assumed that states with an energetic spacing much smaller than E_B are equally populated upon relaxation from the continuum into the excitonic states.[78] Only with increasing temperature does the probability of a thermal transition during the long lifetime of the lower level start to deviate from zero and the fast decay from the higher level can be accessed, as can be seen in the TR-PL curve at 80 K. Combining this observation from the TR-PL data with the corresponding PL spectra, the origin of the shift can be deduced: At low temperatures the emission stems mainly from the lower energy level and at higher temperatures mainly from the higher energy level. It follows that the energetic width of the shift of 32.3 meV should resemble the energetic spacing between the two levels involved.

Excitonic states with these properties are often termed bright and dark excitons and stem from an additional splitting of the hydrogen-like excitonic sublevels. Here, the terms bright and dark refer to the transition matrix element of the respective radiative transition to the ground state. If the matrix element is zero due to the violation of a quantum mechanical conservation law, a state is termed dark. Generally, this does not exclude such transitions completely and a radiative decay can still occur with the participation of an additional particle or due to other perturbations. Such an additional requirement typically renders the transition quite slow, similar to phosphorescence requiring a spin flip to take place.[79] As discussed in Subsection 2.4.1, the band gap is well defined in lead halide perovskites by one non-degenerate p-like conduction band (CB1/SO) and one non-degenerate s-like valence band (VB1). In the vicinity of the band gap this leads to only two types of electrons and holes, respectively, when spin is considered. It has been shown for cesium lead halide nanocrystals that this results in three bright triplet exciton states as well as one dark singlet exciton state.[32,80]

While the energetic splitting of the exciton fine structure is generally negligible in bulk semiconductors, even at lower temperatures, it is known that it can be increased by quantum confinement. For CdSe NPLs, however, the bright-dark splitting reaches only 6 meV in 3 ML NPLs, which are 0.9 nm thick, and, thus, even 0.3 nm thinner than the 2 ML cesium lead bromide NPLs.[81] The peak shift of 32.3 meV we observed would even be the largest bright-dark splitting reported to date in any semiconductor nanocrystal. To gain a deeper theoretical understanding of the excitonic fine structure in this strongly anisotropic system and explain the unusually large bright-dark splitting, we collaborated with Alexander L. Efros at the U.S. Naval Research Laboratory as well as Peter C. Sercel at the Center

for Hybrid Organic Inorganic Semiconductors for Energy. They developed an effective mass model, which takes quantum and dielectric confinement anisotropy into account, to describe the bright and dark exciton states in $Cs_{n-1}Pb_nBr_{3n+1}$ NPLs. The model is presented here in a nutshell, since its results are important in the following. The full derivation, however, can be found in Reference [77] merged with the other results presented in this chapter.

4.2 2D Exciton in Perovskite Nanoplatelets

To describe an exciton in an effective mass model, the Hamilton is first divided into independent center-of-mass $\vec{R} = (m_e\vec{r_e} + m_h\vec{r_h})/(m_e + m_h)$ and relative electron-hole coordinates $\vec{r} = \vec{r_e} - \vec{r_h}$ defining the exciton translational mass $M = m_e + m_h$, the reduced mass $\mu = (1/m_e + 1/m_h)^{-1}$, the center-of-mass momentum $\hat{P} = \hat{p_e} + \hat{p_h}$ and the relative momentum $\hat{p} = (m_h\hat{p_e} - m_e\hat{p_h})/M$:

$$\hat{H}_0 = \hat{H}_{0,\mathrm{com}} + \hat{H}_{0,\mathrm{rel}} = \frac{\hat{P}^2}{2M} + \left[\frac{\hat{p}^2}{2\mu} + V(\vec{r})\right] \tag{4.1}$$

Here, the Coulomb potential $V(\vec{r})$ describes the electron-hole interaction and takes into account the difference in dielectric constant between the NPL and its surrounding.[82,83] The resulting wave function of the exciton ground state in an infinite 2D semiconductor layer with thickness d in the z-direction is made up of the band edge Bloch functions $u_{j_e}(\vec{r_e})$ and $u_{j_h}(\vec{r_h})$, the wave functions $\sqrt{2/d}\cos(\pi z_e/d)$ and $\sqrt{2/d}\cos(\pi z_h/d)$, which describe electron and hole confinement in the layer, respectively, and the relative motion wave function $\phi_d(\vec{r_e} - \vec{r_h})$ with zero angular momentum in z direction. Introducing the finite size of a NPL in the lateral dimensions in addition to the thickness d to this system by modeling the edges as impenetrable barriers, the exciton wave function in a NPL can then be expressed as:

$$\Psi^d_{j_e,j_h}(\vec{r_e},\vec{r_h}) = \frac{4u_{j_e}(\vec{r_e})u_{j_h}(\vec{r_h})}{d\sqrt{L_xL_y}}\cos\left(\frac{\pi X}{L_x}\right)\cos\left(\frac{\pi Y}{L_y}\right)\cos\left(\frac{\pi z_e}{d}\right)\cos\left(\frac{\pi z_h}{d}\right)\phi_d(\vec{r_e} - \vec{r_h}) \tag{4.2}$$

Next, to analyze this wave function, the conduction and valence band Bloch functions $u_{j_e}(\vec{r_e})$ and $u_{j_h}(\vec{r_h})$ have to be described. While the Bloch functions of the s-like VB1 can be just written as $u_{v,1/2} = |S\uparrow\rangle$ and $u_{v,-1/2} = |S\downarrow\rangle$, the effect of the strong spatial confinement on the p-like CB1 has to be considered. As discussed in Subsection 2.4.1, the CB1 relevant for exciton formation is the split-off band with $J = 1/2$, which is lowered by the strong spin-orbit coupling, and lies, thus, considerably below the $J = 3/2$ light and heavy electron bands. Employing the spin-orbit splitting Δ_{SO} between the $J = 3/2$ and $J = 1/2$ states, as well as $\delta = -3\frac{\hbar^2}{2m_0}\gamma_2\frac{2\pi^2}{d^2}$, which can be considered as an effective tetragonal crystal field, the energy of the split-off band can be written as:[80]

$$E_c = \frac{3\Delta_{SO} - \delta}{6} - \frac{1}{2}\sqrt{\Delta^2_{SO} - \frac{2}{3}\Delta_{SO}\,\delta + \delta^2} \tag{4.3}$$

This results in the CB1 Bloch functions:[80,84]

$$u_{c,1/2} = -\sin\theta Z\uparrow - \cos\theta\frac{X + iY}{\sqrt{2}}\downarrow \qquad u_{c,-1/2} = -\cos\theta\frac{X - iY}{\sqrt{2}}\uparrow + \sin\theta Z\downarrow \tag{4.4}$$

Here, the angle θ is given by:[84]

$$\tan 2\theta = \frac{2\sqrt{2}\Delta_{SO}}{\Delta_{SO} - 3\delta}, \qquad (\theta \leq \frac{\pi}{2}). \tag{4.5}$$

At this point, the exciton wave function as well as the band-edge Bloch functions in a NPL have been established. The exchange interaction between the electron and hole spin states that has to be considered next splits the fourfold degenerate exciton ground state into three bright and one dark exciton levels. The basis employed consists of the functions $|X_i\rangle$, which run over $|D\rangle$, $|X\rangle$, $|Y\rangle$ and $|Z\rangle$ representing the wave functions of the dark state and the three bright excitons with transition dipoles aligned along the X, Y, Z directions.[85] Here, Z is defined along the thickness dimension of the NPL. In the following, two splitting energies have to be considered: The first of those represents the splitting between the degenerate X and Y dipoles and the dark exciton. The degeneracy of the X and Y dipoles is not lifted, as the NPLs are assumed to be quadratic in the X-Y-plane and the crystal structure is approximated as cubic. This simplification of the orthorhombic crystal structure is justified by the small contribution it has to the total fine structure splitting compared to the effect of the strong shape anisotropy of the NPL. This is discussed later in more detail. Typically, the exchange interaction is split into short-range (SR) and long-range (LR) components: $\Delta E_{\text{exchange}} = \Delta E_{SR} + \Delta E_{LR}$. While the SR exchange interaction has the form of a contact interaction with an effective spin operator acting on the electron and hole Bloch functions, the LR exchange interaction induces a splitting between the longitudinal and transverse (LT) optically active exciton states. Again, the exact derivation of those components can be found in Reference [77], here, just the results are listed. Accordingly, the fine structure splitting stemming from the SR exchange interaction between the X and Y dipoles and the dark exciton $\Delta E_{XY,SR}(d)$ and between the Z dipole and the dark exciton $\Delta E_{Z,SR}(d)$ is determined to be:

$$\begin{aligned} \Delta E_{XY,SR}(d) &= f_{XY} C^{SR} \Omega \frac{3}{2d} |\phi_d(0)|^2 \\ \Delta E_{Z,SR}(d) &= f_Z C^{SR} \Omega \frac{3}{2d} |\phi_d(0)|^2 \end{aligned} \tag{4.6}$$

Here, C^{SR} is the exchange constant and Ω is the volume of the crystal unit cell. The thickness-dependence of the fine structure anisotropy factors f_{XY} and f_Z is depicted in Figure 4.4 a.

Next, the LR contributions to the fine structure splitting $\Delta E_{XY,LR}(d)$ and $\Delta E_{Z,LR}(d)$ are considered and can be written as:

$$\begin{aligned} \Delta E_{XY,LR}(d) &= \frac{\hbar\omega_{LT}(d)}{2} f_{XY} \mathcal{A}_{XY}(d/L) \frac{\Theta}{\Theta_{\text{bulk}}} \\ \Delta E_{Z,LR}(d) &= \frac{\hbar\omega_{LT}(d)}{2} f_Z \mathcal{A}_Z(d/L) \frac{\Theta}{\Theta_{\text{bulk}}} \end{aligned} \tag{4.7}$$

In these Equations $\hbar\omega_{LT}(d) = \hbar\omega_{LT}^{\text{bulk}}(E_g/\hbar\omega)^2$ is the thickness-dependent LT splitting energy and $\frac{\Theta}{\Theta_{\text{bulk}}} = \frac{3}{2d}\pi a_x^3 |\phi_d(0)|^2$ the ratio of the confined and the bulk exchange overlap. The dimensionless LR exchange integrals $\mathcal{A}_{XY}$ and $\mathcal{A}_Z$ are plotted in Figure 4.4 b.

Lastly, Figure 4.4 c depicts the thickness-dependence of the SR and LR contributions to the fine structure splitting represented by Equation 4.6 and Equation 4.7. The SR contribution is depicted

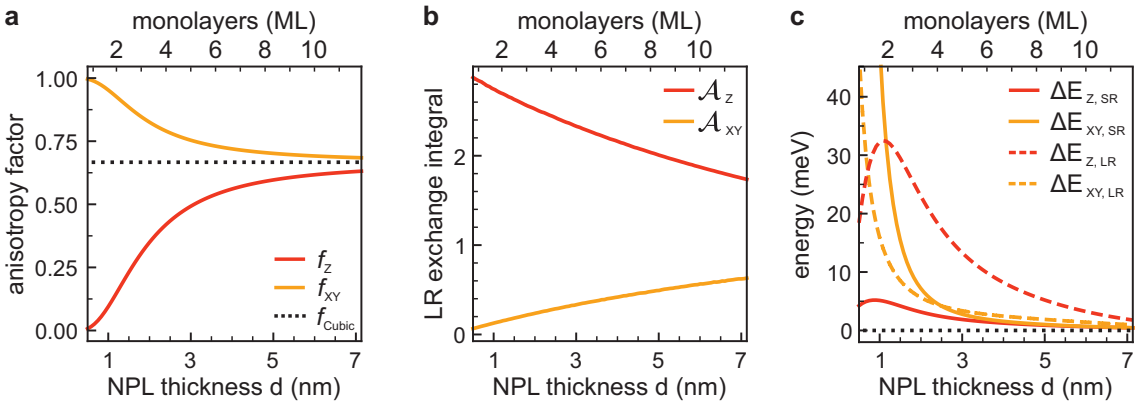

Figure 4.4: Important Quantities within the Model. a) The fine structure anisotropy factors f_{X_i} encode the anisotropic confinement of the band-edge Bloch functions in a square-shaped NPL. The value for a nanocube is depicted as a dashed black line. **b)** The thickness-dependence of the dimensionless LR exchange integrals $\mathcal{A}_{X_i}$ is calculated numerically and plotted here. **c)** The total SR and LR contributions to the fine structure splitting resulting from the electron-hole exchange interaction are depicted. The dark level is set to zero and is represented by the dashed black line.

as solid lines and the LR contribution is depicted as dashed lines, while red and orange encode the Z-dark splitting and XY-dark splitting, respectively. All material parameters, which are used in the calculations, are listed in Table 4.1.

Parameter	Value	Description	Source
$\hbar\omega_{LT}^{\text{bulk}}$	5.4 meV	LT exciton splitting	Experiment[86]
E_p	27.8 eV	Kane energy	Derived from $\hbar\omega_{LT}$[80,86]
a_{ex}	3.1 nm	bulk exciton Bohr radius	Theory[87]
ϵ_i	7.3	interior dielectric constant	Experiment[88]
ϵ_o	2.1263	exterior dielectric constant	Experiment[89]
ϵ_∞	4.76	high-frequency dielectric constant	Derived from $\hbar\omega_{LT}^{\text{bulk}}$ and E_p[86,87]
μ	$0.126\,m_0$	reduced effective mass	Experiment[88]
m_e	$0.25\,m_0$	electron effective mass	Theory[87]
m_h	$0.25\,m_0$	hole effective mass	Theory[87]
E_g	2.342 eV	band gap	Experiment ($T = 4.2$ K)[88]
Δ_{SO}	1.5 eV	spin-orbit splitting	Theory[80]
Ω	0.2104 nm^3	pseudocubic unit-cell volume	Experiment[80]
C^{SR}	315.5 meV	short-range exchange constant	Derived from experiment[80,90]

Table 4.1: $CsPbBr_3$ Material Parameters Used for Calculation of the Level Splitting. All parameters, which were used in Reference [77] for the calculations, and their original source are listed here.

4.3 Spectroscopically Determined Bright-Dark Splitting

Since the theoretical description of an exciton in a $Cs_{n-1}Pb_nBr_{3n+1}$ NPL has been established, we can revisit the data. First, we will investigate the thickness-dependence of the low-temperature spectral shift, which has already been introduced for 2 ML NPLs in Section 4.1 and caused us to theoretically investigate and describe the exciton fine structure in these NPLs. To that end, the low-temperature PL data is acquired for all NPL thicknesses following the same experimental procedure described for the 2 ML NPLs in Section 4.1. Again, a basic experimental room temperature characterization of all NPL thicknesses can be found in Section 3.1. The temperature-dependence of the PL spectrum for all

thicknesses is depicted in Figure 4.5. Here, the individual spectra are distributed in 2.5 K steps from 5 K to 60 K and in 5 K steps from 60 K to 100 K.

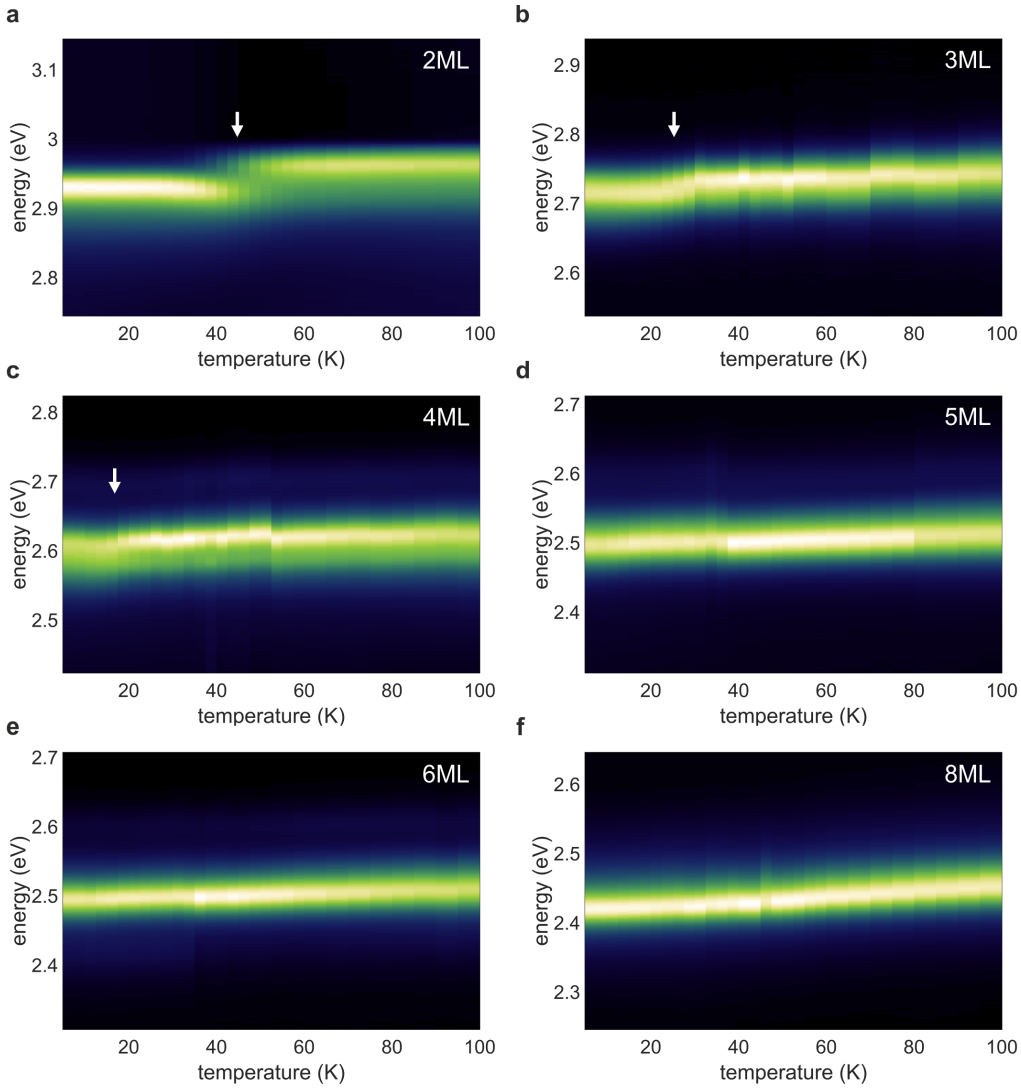

Figure 4.5: Temperature-Resolved Photoluminescence Spectra. PL spectra acquired from 5 K to 100 K for all NPL thicknesses with each spectrum normalized individually in respect to its overall integrated intensity to account for small laser fluctuations. The shift, highlighted by the white arrows, is clearly visible for the 2 ML NPLs and still discernible for the 3 ML and 4 ML NPLs, although smaller and at lower temperatures. With increasing thickness, however, a possible shift becomes more difficult to observe, due to inhomogeneous broadening of the spectrum masking the effect.

Interestingly, the energetic width of the shift strongly decreases with increasing NPL thickness and occurs at lower temperatures. Whereas the PL shift is more or less discernible for the 2 ML to 4 ML NPLs, its existence is not as easily verified for the 5 ML, 6 ML and 8 ML NPLs. This stems from the fact that for these thicknesses the energetic shift is much smaller than the inhomogeneous broadening of the spectrum introduced in Subsection 2.2.5, which covered the fundamental broadening mechanisms of optical transitions. If one looks closer at the temperature-dependent PL spectra of the 5 ML and 6 ML NPLs, however, it is still present, as depicted in Figure 4.6 a and Figure 4.6 b, respectively. Here, three spectra from 5 K to 10 K as well as three spectra from 17.5 K to 22.5 K display very little deviation within these two intervals, while there is an offset between the intervals. The temperature at which this occurs fits the trend of decreasing temperatures with increasing NPL thickness.

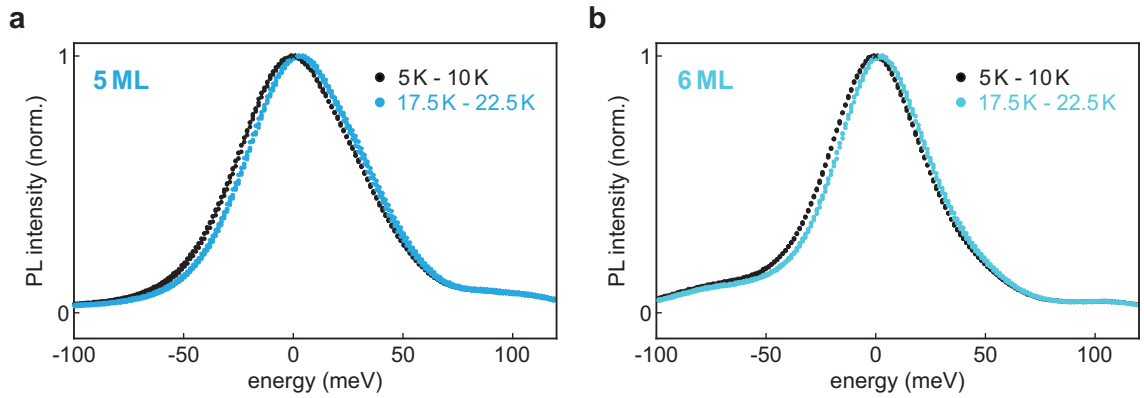

Figure 4.6: 5 ML and 6 ML Photoluminescence Spectra. All measured spectra within the intervals denoted in the two panels are plotted in the respective color. This reveals that the shift is still present in **a)** 5 ML and **b)** 6 ML NPLs. However, it is much smaller and, thus, not as easily distinguishable due to the inhomogeneously broadened spectra.

In Figure 4.7, several spectra at temperatures below and above the spectral shift are plotted for all investigated NPL thicknesses with the maximum position of the 5 K spectrum offset to zero on the energy axis. The temperature ranges from which the spectra are taken differ for each NPL thickness, since the temperature at which the shift occurs decreases with increasing NPL thickness. The exact temperature interval boundaries for each thickness are presented in Table 4.2. For the 8 ML NPLs the exact range of the shift is no longer observable and the same intervals as for the 5 ML and 6 ML NPLs are employed.

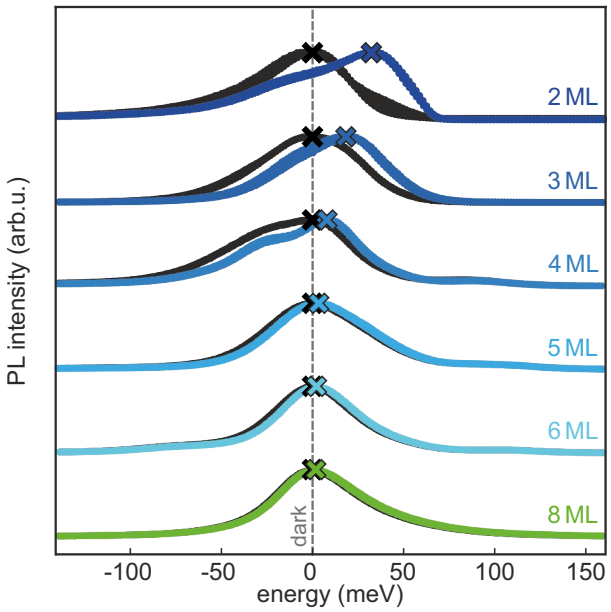

Figure 4.7: Thickness-Dependent Spectral Shift. For each NPL thickness several spectra before (black dots) and after the PL shift (colored dots) are superimposed. The exact temperature intervals from which the PL spectra are taken are shown in Table Table 4.2 for each thickness. All spectra are offset horizontally according to the respective energetic position of the peak maximum prior to the shift denoted by the black cross. Accordingly, the PL shift resembled by the position of the colored cross becomes larger as the thickness of the NPL decreases, from 1.8 meV for 8 ML NPLs up to 32.3 meV for 2 ML NPLs.

The black and the colored dots in Figure 4.7 consist of all data points of those spectra measured in 2.5 K increments before and after the sudden spectral shift, respectively. The exact number of spectra varies with thickness, since, e.g., the black dots contain all fourteen spectra up to 37.5 K for 2 ML NPLs, whereas the black dots contain only three spectra for 5 ML, 6 ML and 8 ML NPLs, as the shift

already occurs between 10 K and 17.5 K. At first glance, the maximum of all spectra of the same color or all black spectra of one thickness, respectively, does not shift noticeably compared to the energetic width of the shift between the black and colored dots. Still, a small contribution of a continuous shift caused by the temperature-dependence of the band gap, which is sometimes also called band gap renormalization, should be superimposed on the sudden shift. An upper bound for the contribution of this effect over the small temperature range in which the sudden shift takes place is given in Table 4.2 for all thicknesses up to 5 ML. The source of these values is another project conducted within this thesis, which is presented in Chapter 5.

NPL thickness	2 ML	3 ML	4 ML	5 ML	6 ML	8 ML
Temp. before PL shift	37.5 K	17.5 K	12.5 K	10 K	10 K	10 K
Temp. after PL shift	57.5 K	30 K	22.5 K	17.5 K	17.5 K	17.5 K
ΔE_{BGR}	3.9 meV	2.6 meV	2.0 meV	1.7 meV	–	–

Table 4.2: Temperature Interval of the Photoluminescence Shift. The temperatures of the last spectrum before the PL shift and the first one after the shift. Several spectra before and after these intervals are plotted in Figure 4.7. The interval shifts to lower temperatures and becomes smaller with increasing thickness. Furthermore, the corresponding shift of the PL emission over this interval resulting from band gap renormalization, ΔE_{BGR}, is quantified for all thicknesses up to 5 ML.

At this point, we take into account the conclusion we drew in Section 4.1 that the PL shift should be connected to the exciton fine structure. More specifically, it should resemble the energetic spacing of the dark state and the lowest bright state, as this is the first transition which is activated with increasing temperature. Naturally, a decreased splitting should lead to a decreased activation temperature. This effect also explains, why the small shifts in the thicker NPLs occur at much lower temperatures than the larger shifts in the thinner NPLs.

The full results from the effective mass model $\Delta E_{\mathrm{Z/XY}}(d) = \Delta E_{Z/XY,SR}(d) + \Delta E_{Z/XY,LR}(d)$ are plotted in Figure 4.8 with the dark exciton level set to zero. $\Delta E_{\mathrm{Z/XY}}(d)$ describes the thickness-dependence of the energetic splitting between the dark level and an out-of-plane (Z) and the dark level and an in-plane (XY) polarized bright exciton in a $Cs_{n-1}Pb_nBr_{3n+1}$ NPL. Plots of the two individual contributions $\Delta E_{Z/XY,SR}(d)$ and $\Delta E_{Z/XY,LR}(d)$ can be found in Figure 4.4 c. In addition, the energetic width of the experimentally acquired PL shift is denoted by a colored cross for each thickness. Here, the y-error bars combine two contributions: Since we plotted several curves before and after the shift in Figure 4.7 for each thickness, the mean of the energetic maxima positions of these spectra was denoted by the crosses to reduce spectral noise from the measurements. Accordingly, the first contribution to the error bars stems from the standard deviation of these maximum positions. Second, the spectral shifts might be increased due to a contribution of the continuous shift originating from the temperature-dependence of the band gap, which shifts in the same direction. The ΔE_{BGR} values from Table 4.2, which serve as an upper bound for the effect, are, thus, also added to the error in negative direction. For the 6 ML and 8 ML NPLs the ΔE_{BGR} value of the 5 ML NPLs is used. Furthermore, a horizontal error bar is added to the 8 ML NPLs, as TEM images revealed populations of NPLs with a different thickness within this sample (see Figure 3.1 in Subsection 3.1.4).

Remarkably, the energetic width of the PL shift lies quite close to the respective lowest bright exciton level. It comes as a surprise, however, that the model predicts this should be the in-plane polarized exciton for $d \geq 3$ ML and the out-of plane polarized exciton in 2 ML NPLs, as these levels cross between those two thicknesses. It has to be mentioned again that the parameters going into the model were strictly taken from literature and not tweaked to fit the data. This circumstance gives us on the

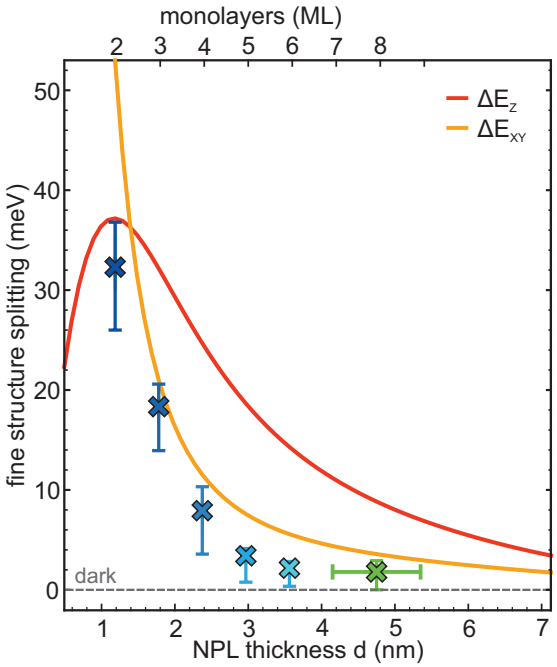

Figure 4.8: Thickness Dependence of the Exciton Fine Structure Splitting. The total exchange splitting $\Delta E_{Z/XY}$ for the bright out-of-plane Z (red line) and the bright in-plane exciton states XY (orange line) in a square $Cs_{n-1}Pb_nBr_{3n+1}$ NPL with side length L = 14 nm. The dark exciton state is set to zero and is the lowest state for all thicknesses. The crosses depict the experimentally determined splitting energies from Figure 4.7 and should correspond to the lowest bright level. The y-error bars contain the standard deviation of the multiple spectra used to determine the splitting as well as the ΔE_{BGR} values from Table 4.2 in negative direction, since a continuous shift of the band gap is superimposed on the shift stemming from the fine structure. The horizontal error bars on the 8 ML sample indicate a possible minor contribution from NPLs of different thicknesses.

one hand additional confidence in the validity of the newly developed model and on the other hand corroborates that the spectral shift does indeed stem from the excitonic fine structure, as suspected in Section 4.1. Notably, the experimental method only works, because the exciton fine structure splitting is so strongly increased by the thickness-confinement in these NPLs and reaches a record value for any semiconductor system of 32.3 mev for the 2 ML NPLs. Comparing this to the reported value of 6 meV for 3 ML CdSe NPLs, which are 0.9 nm thick, and, thus, even 0.3 nm thinner than the 2 ML cesium lead bromide NPLs,[81] it becomes clear, why such a spectral observation of the fine structure is usually difficult in ensemble measurements.

While the overall agreement of theory and experiment is surprisingly good in terms of the thickness-dependence, the experimental values are generally too low with an increase of the relative deviation towards thicker NPLs. This could stem from multiple sources besides the fact that the correct determination of the PL shift becomes progressively more difficult with increasing thickness due to a decreased fine structure splitting. First, some of the acquired TEM images suggest that the shape inhomogeneity increases towards thin films of thicker NPLs. Naturally, this leads to different NPLs within the measurement volume possessing different excitonic fine structures and can introduce errors to the extracted splitting. Second, and possibly even more important, the theoretical model does not include the crystal structure anisotropy, which introduces an additional contribution to the lifting of the degeneracy of the exciton fine structure. The $Cs_{n-1}Pb_nBr_{3n+1}$ NPLs possess an orthorhombic lattice structure at these temperatures. Since it is not clear yet, however, if the orthorhombic axes have a preferential alignment in respect to the Z-axis of the NPL, the effect can not be added on top of

the model, as the alignment would determine whether the overall splitting is increased or decreased. While the contribution of this effect should be small in the thinner NPLs compared to the strong splitting stemming from the shape anisotropy, the same can not be said for the thicker NPLs. Finally, some of the parameters employed by the theoretical calculation could be inaccurate. For example the surrounding of the NPLs in a film is assumed to consist mainly of the organic ligands attached to its surface as well as additional unbound ligands. Thus, the dielectric constant outside of the NPLs is taken from oleic acid, one of the two ligands present. This might of course be inaccurate and not describe the environment perfectly and, therefore, introduce a small error to the calculation.

The spectral shift of the PL nicely validated the general trend of the model. However, the strong splitting of the bright exciton into in-plane and out-of-plane exciton states reaching from 4.5 meV up to 13.2 meV over the investigated range still needs experimental proof. In particular, the level crossing between 2 ML and 3 ML NPLs is thus far only predicted by the model. Furthermore, a possible investigation of the thickness dependence of the shift temperature to further corroborate the splitting energies proves difficult, since on the one hand a lot of transitions are involved in such a three level system and on the other hand the exact transition temperatures, at which the PL spectrum for a specific NPL thickness shifts, are not easy to pinpoint in the spectral data. Therefore, to gain a deeper insight into the exciton fine structure, we turn to temperature-dependent TR-PL measurements.

4.4 Exciton Lifetimes

In the first section of this chapter, Section 4.1, the low-temperature decay dynamics of excitons arising from an energetic splitting of the exciton fine structure have already been introduced. For completeness, however, the main features of those dynamics are summarized briefly before describing them quantitatively with a mathematical model. The experimental background on the setup configuration employed for acquiring the TR-PL can be found in Subsection 3.2.3, while the fundamentals on different recombination mechanisms as well as intraband relaxation in semiconductors are discussed in Section 2.2.

As a basis for discussion, Figure 4.9 depicts TR-PL curves of 4 ML NPLs for different temperatures. Importantly, the 5 K TR-PL curve, and this holds true for each thickness, consists of two distinctly different decay components. The respective temperature-dependent rates shall be defined as Γ_{long} and Γ_{short}. Since the excitation pulse with a wavelength of 400 nm generates free electron-hole pairs in all of the samples, the excitonic states are populated through a fast initial relaxation from the continuum states into the excitonic states. As the fine structure splitting of the 1s exciton state is much smaller than the exciton binding energy, it is generally assumed that the different 1s fine structure levels are populated with equal probability from higher lying states.[78] The temporal resolution of the setup used for these measurements is much slower than the relaxation process into the excitonic states,[70] thus, we can assume an equal population of the different 1s fine structure levels at t = 0. Independent of the validity of the model prediction that the bright in-plane (XY) and out-of-plane (Z) excitonic levels are also split energetically by the shape anisotropy, the lowest exciton level in these NPLs is in any case the dark state. Accordingly, the fast initial decay corresponds to the depletion of the bright exciton levels through radiative transitions into the ground state, which allow for observing the process in the TR-PL measurements, as well as transitions into the lower lying dark state. Subsequently, the very slow spin-forbidden decay on the order of a microsecond from the dark exciton state takes place. This

process is, however, still strongly radiative and it appears, as if no competing non-radiative transition into the ground state is significantly faster. Notably, when integrating over the two components nearly all of the emitted photons stem from the slow decay. Thus, the transition from the bright levels into the dark level must be much faster than the radiative transitions from the bright levels into the ground state. Interestingly, this also explains the observation in the last section that the spectra at temperatures lower than the shift are dominated by the dark state.

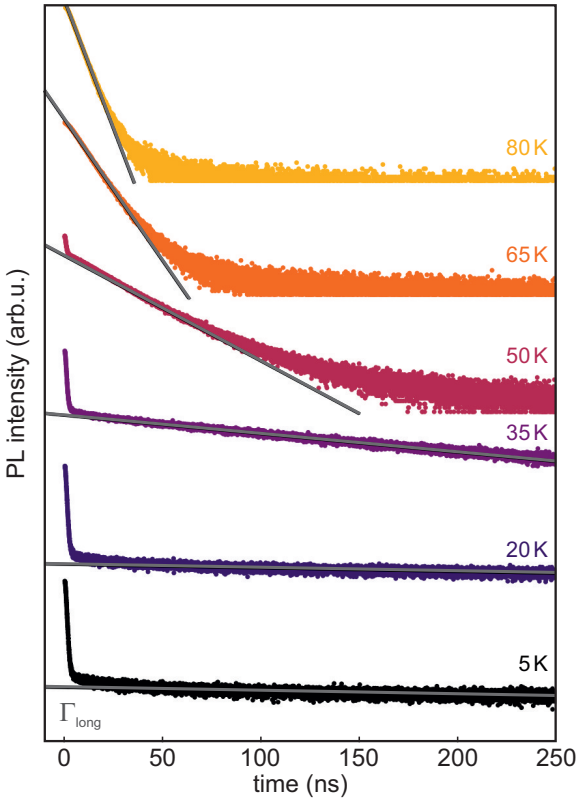

Figure 4.9: Time-Resolved Photoluminescence of 4 ML Nanoplatelets. TR-PL curves of 4 ML NPLs for different temperatures between 5 K and 80 K offset in the y-direction for clarity on a logarithmic PL intensity scale. In addition, monoexponential fits for extracting the long decay rate Γ_{long} are displayed as solid grey lines. Γ_{long} increases with temperature, while the component characterized by Γ_{short} vanishes at 65 K. For Γ_{short}, however, only an upper bound can be extracted from the data, since this decay component is faster than the temporal resolution of the setup of a few hundred picoseconds.

Increasing the temperature sufficiently activates the phonon-assisted transition between the dark level and the bright levels. The exact temperature at which this happens is thickness-dependent and fits the temperature at which the respective PL peak shifts spectrally. The increase in temperature triggers two effects: First, the upwards transition becomes probable within the long lifetime of the dark state. Thus, the dark state can also be depleted with a bright state as an intermediate state and photons with the energy difference of this bright state and the ground state are emitted. Naturally, this effect decreases the lifetime of the second decay component gradually with increasing temperature. Second, the transition rates from the bright states into the dark state also increase. This manifests in the gradual vanishing of the first component, as less excitons decay radiatively immediately upon arriving in the bright states at t = 0. In other words, all transitions between the fine structure states become faster and the respective temperature-dependent transition rates only determine the percentage of time an exciton spends in a specific state. For a large number of excitons this just results in a Bose-Einstein distribution function between the fine structure states, which is of course influenced by the fast radiative decay of the bright states, while a radiative decay from the dark states becomes

highly improbable on this timescale. Ultimately, this leads to one monoexponential decay, which is just slowed by the amount of time a particle spends in the dark state. For higher temperatures ($E_{th} >> E_{splitting}$) this time converges to 25 % of the total time as the fine structure consists of three bright states, as opposed to one dark state.

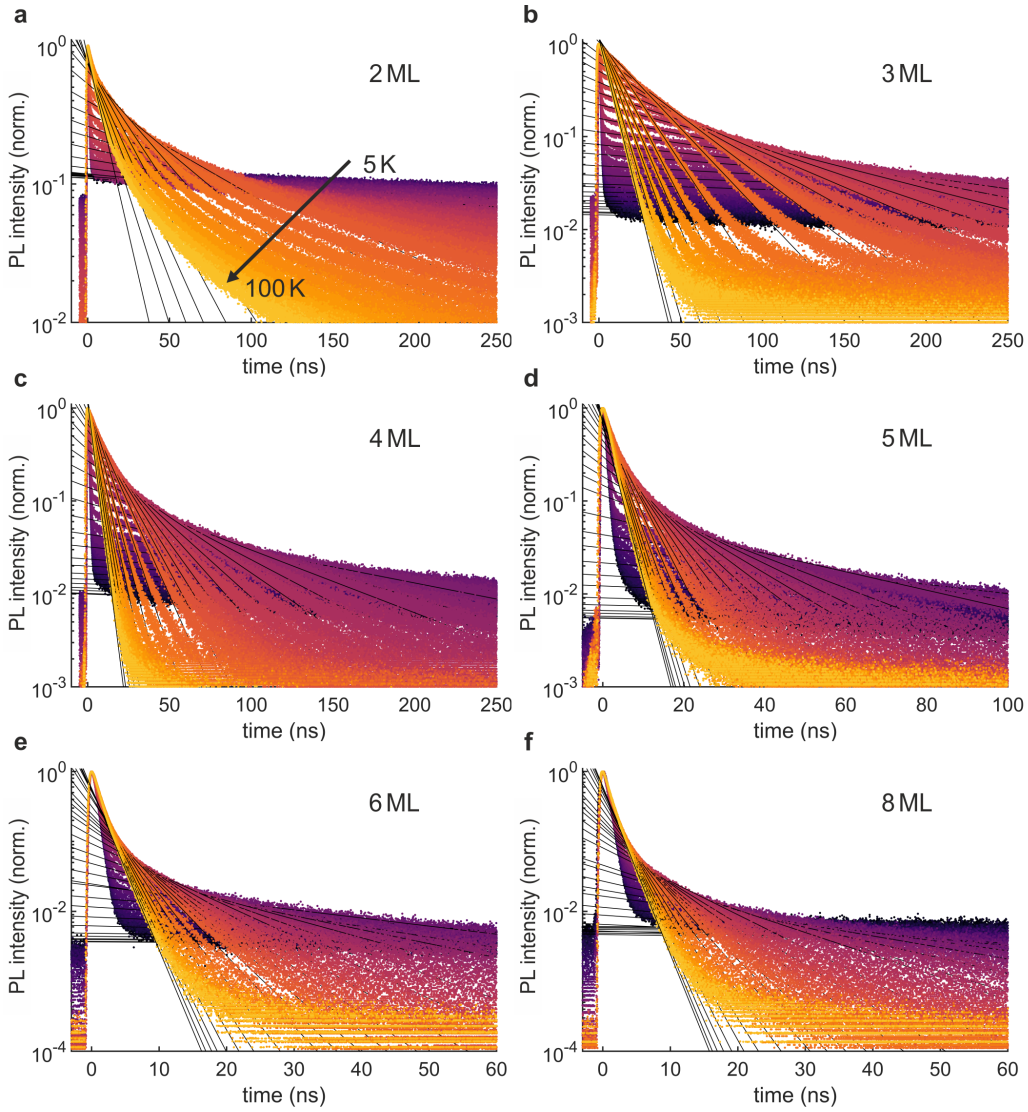

Figure 4.10: Temperature-Dependent Photoluminescence Decay of all Nanoplatelets. Normalized TR-PL curves for all NPL thicknesses acquired in 2.5 K steps from 5 K to 60 K and in 5 K steps from 60 K to 100 K on a logarithmic PL intensity scale. The typical signature of the exciton fine structure can be observed for all thicknesses. Furthermore, the monoexponential fits of the long decay component used for the extraction of Γ_{long} are added as solid black lines.

To enable the comparison of the TR-PL data to a mathematical model, the temperature-dependent rate Γ_{long} has to be determined for all thicknesses and temperatures. Figure 4.10 displays all of the fits employed for the extraction of Γ_{long}. The respective longer decay component can be precisely fitted with a single exponential for all thicknesses from 3 ML upwards. Only for the case of 2 ML NPLs is the long decay component not perfectly exponential in a certain temperature range, likely due to an additional decay channel affecting the dynamics on a similar timescale. In these ultrathin NPLs, a broad emission band develops simultaneously below the band gap, as depicted in Figure 4.11. This behavior has previously been attributed to self-trapped excitons (STE) in studies on layered 2D perovskites of the same thickness of 2 ML.[91] Even if this feature is spectrally filtered prior to the

TR-PL measurement, the dynamics of the free excitons cannot be completely detached. Most likely, the additional pathway for an exciton to self-trap also affects the dynamics of the long-lived dark excitons. Especially for higher temperatures, however, the STE emission appears as an even longer decay component, only present in the 2 ML NPLs (e.g. 100 K). Thus, it is still possible to extract Γ_{long} to a certain degree, as shown by the fits in Figure 4.10 a. One has to keep in mind, though, that those values might not be exact and can contain an error.

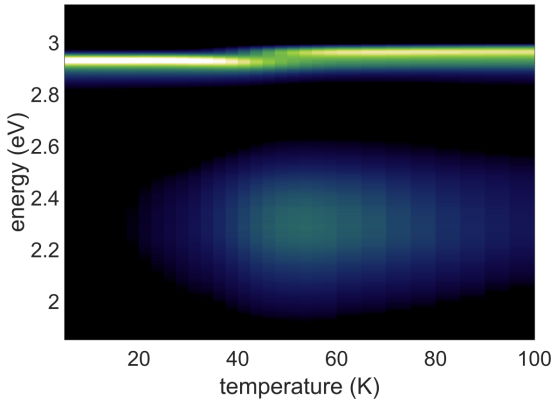

Figure 4.11: Self Trapped Excitons in 2 ML NPLs. The PL spectrum of 2 ML NPLs exhibits a broad emission band centered at 2.3 eV. This broad emission becomes visible at around 20 K and reaches a maximum around 50 K before decreasing again. Such a behavior has also been observed for layered 2D perovskites of a thickness of 2 ML and is attributed to the self-trapping of excitons.[91]

In order to describe the temperature-dependence of the TR-PL curves or, more specifically, the temperature-dependence of the extracted Γ_{long} rates, all rates between the levels involved have to be considered. Previously, e.g. for CdSe NPLs, a model comprising two excited states, one bright (B) and one dark (D) state was applied.[81,92] A schematic of such a model is presented in Figure 4.12 a. The transition between those two excited states, γ_{BD}, encodes a temperature-independent rate γ_0 from B to D indicated by the black arrow as well as a temperature-dependent rate $\gamma_{th} = \gamma_0 N_B$ in both directions indicated by the red arrow. The resulting transition rates in the two directions upwards (↑) and downwards (↓) can, thus, be written as:

$$\begin{aligned} \gamma_{BD\uparrow} &= \gamma_{th} = \gamma_0 N_B \\ \gamma_{BD\downarrow} &= \gamma_0 + \gamma_{th} = \gamma_0 (N_B + 1) \end{aligned} \tag{4.8}$$

Here, $N_B = 1/[exp(\Delta E/k_B T) - 1]$ is the Bose-Einstein phonon occupation for phonons of the energy ΔE. Both of these processes, which enable an exciton transition between the degenerated bright ($J = 1$) and the dark state ($J = 0$), require a spin-flip of either the electron or the hole, since these states differ by one unit of total angular momentum J.

From the model depicted in Figure 4.12 a the following rate equations for the populations of the bright and the dark state, p_B and p_D, can be deduced:

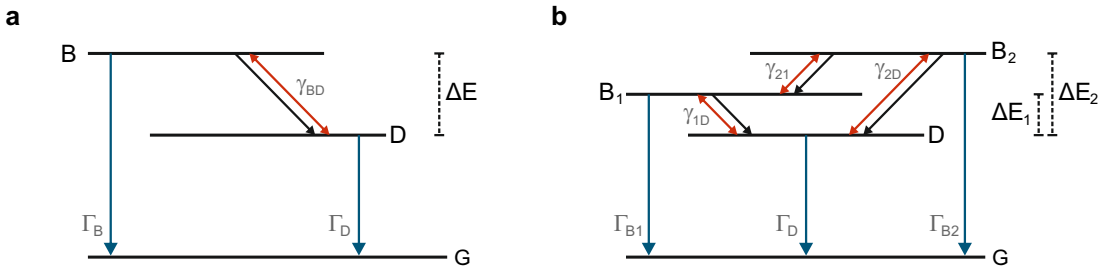

Figure 4.12: Splitting of the Bright States. a) A model, which considers only the bright-dark splitting, has been employed before to describe the temperature-dependence of TR-PL curves connected to the exciton fine structure.[81,92] **b)** Taking the splitting of the bright exciton states in the LHP NPLs predicted by the effective mass model into account, a more refined model comprising three excited states emerges. All of the transitions between the excited states γ_{XX} combine a temperature-independent rate from the higher to the lower level γ_0 indicated by the black arrow as well as a temperature-dependent rate $\gamma_{th} = \gamma_0 N_B$ in both directions indicated by the red arrow.

$$\begin{aligned} \frac{dp_B}{dt} &= -[\Gamma_B + \gamma_0(N_B + 1)]p_B + \gamma_0 N_B p_D \\ \frac{dp_D}{dt} &= -[\Gamma_D + \gamma_0 N_B]p_D + \gamma_0(N_B + 1)p_B \end{aligned} \tag{4.9}$$

Despite the bright state in this scenario consisting of three degenerated states in LHPs, we will assume that $p_B(t = 0) = p_D(t = 0) = 0.5$. This assumption should, however, mainly influence the percentage of photons emitted from the bright state at low temperatures and not the temperature-dependence of the dynamics. Then, for the decay component Γ_{long}, one arrives at:[81,92]

$$\Gamma_{long}(T) = \frac{1}{2}\left[\Gamma_B + \Gamma_D + \gamma_0 \coth\left(\frac{\Delta E}{2k_B T}\right) - \sqrt{(\Gamma_B - \Gamma_D + \gamma_0)^2 + \gamma_0^2 \sinh^{-2}\left(\frac{\Delta E}{2k_B T}\right)}\right] \tag{4.10}$$

The rate Γ_D can easily be extracted from the data, as $\Gamma_{long} = \Gamma_D$ for $E_{th} << E_{splitting}$, since thermal activation of excitons from the dark state D to the bright state B is then negligible. Similarly, the fast decay $\Gamma_{short}(T) = \Gamma_B + \gamma_0$ at 5 K, which describes the depopulation of the bright level. This fact can not be used to eliminate another fitting parameter, however, since the setup is not fast enough to resolve $\Gamma_{short}(T)$ and just delivers an upper bound for it. Thus, the data resembling $\Gamma_{long}(T)$ has to be fitted with the three free parameters Γ_B, γ_0 and ΔE.

Figure 4.13 a depicts the $\Gamma_{long}(T)$ values obtained from the monoexponential fits of the long decay component shown in Figure 4.10. The curves corresponding to the different NPL thicknesses are offset vertically for clarity. Furthermore, the y-axis is plotted logarithmically, since $\Gamma_{long}(T)$ changes over two orders of magnitude between 5 K and 100 K and derivations of the fit should also be visible for lower Γ_{long} values. The values basically stay constant up to a thickness dependent temperature at which the thermal transition from the dark to the bright states is activated.

Fits obtained via Equation 4.10 are represented by the grey curves in Figure 4.13 a and display good agreement with the data. For all thicknesses, the sum of the resulting γ_0 and Γ_B rate lies between 20 ns^{-1} and 110 ns^{-1} and, thus, four orders of magnitude above the Γ_D rates of around 10^{-3} ns^{-1}, which seems reasonable compared to the TR-PL data. Notably, the temperature at which the thermal transition from the dark state into the bright state is activated and $\Gamma_{long}(T)$ starts to increase significantly is mainly determined by the energetic splitting between the two states ΔE. However, the ΔE values

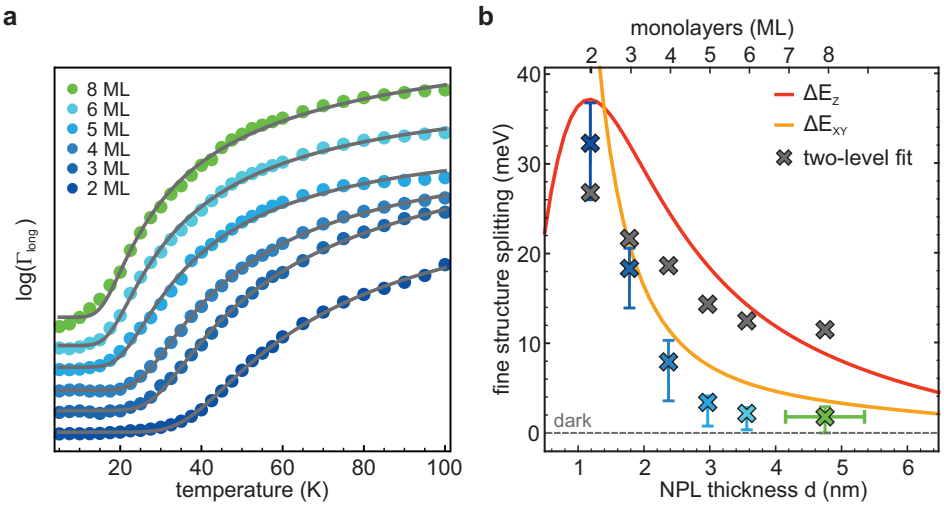

Figure 4.13: Two-Level Model Fits. a) The $\Gamma_{\text{long}}(T)$ values extracted from the monoexponential fits of the long decay component shown in Figure 4.10 for all temperatures and NPL thicknesses plotted on a logarithmic y-axis. The curves corresponding to the different NPL thicknesses are offset vertically for clarity. The grey curves show the fits of Equation 4.10 to the data displaying good agreement. **b)** The ΔE values resulting from the fits (grey crosses) are compared to the experimental and theoretical description of the exciton fine structure introduced in previous section.

extracted from the fits, do not match any of the previously observed splitting energies. Figure 4.13 b compares these extracted values (grey crosses) to the theoretically predicted fine structure splitting as well as the energetic width of the spectral shift, which happens simultaneous to the increase of $\Gamma_{\text{long}}(T)$ with increasing temperatures. Especially for 4 ML to 8 ML NPLs the energetic shift would be much more pronounced, if the ΔE values extracted from the fits employing a two-level model were correct. Therefore, following the theoretically predicted splitting of the bright exciton states into a degenerate in-plane level and a non-degenerate out-of-plane level and the inability of the two-level model to predict the correct spectral shift, we developed a model comprising three excited states. In accordance with the effective mass model, these consist of two bright states above one dark state. The two bright states will be termed B1 and B2 instead of XY and Z, since the XY and Z levels are predicted to cross between 2 ML and 3 ML NPLs. Thus, the lower level will be represented by B1 for all thicknesses independent of it being the XY or Z level. The resulting model is schematically depicted in Figure 4.12 b.

Adding a third excited state, however, complicates the formulas significantly. The full rate equations for all three levels and the derivation of the result can be found in the Supporting Information of Reference [77]. Furthermore, this new model has eight free parameters, too many to result in a reliable fit. However, as shown in [77], the ratio between Γ_{B1} and Γ_{B2} can be calculated from the transition matrix elements. In addition, we fix the splitting energies between the three excited states, ΔE_1 and ΔE_2, to the values predicted by the effective mass model. This reduces the number of free parameters to five and enables a more reliable fitting.

Figure 4.14 depicts the fits of $\Gamma_{\text{long}}(T)$ achieved with the three-level model. The resulting fitting parameters are summarized in Table 4.3. Importantly, most parameters are in accordance with the general principles of the exciton fine structure. In particular, the exciton recombination rates of the two bright levels, Γ_{B1} and Γ_{B2} are a lot faster than the recombination rate of the dark state, Γ_{D}. However, for the case of the 2 ML and the 8 ML NPLs the fits are not optimal and some of the resulting parameters are strongly over- or underestimated. In the case of the 8 ML NPLs this is likely rooted

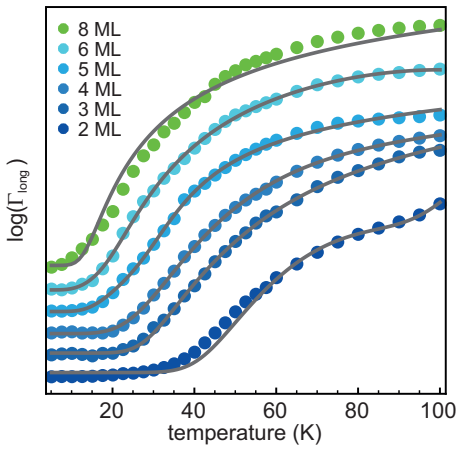

Figure 4.14: Three-Level Model Fits. The $\Gamma_{\text{long}}(T)$ values are plotted exactly as in Figure 4.13 a for all temperatures and NPL thicknesses on a logarithmic y-scale and offset for clarity. The grey curves show the fits according to the three-level model schematically depicted in Figure 4.12 b.

in the inhomogeneity of this sample, which has already been discussed. A different effect, however, could be responsible for the slight deviation in the range from 30 K to 55 K between the fit and the data of the 2 ML NPLs. Namely, in this temperature range the broad emission peak stemming from the self-trapping of excitons emerges only in the 2 ML sample, as shown in Figure 4.11. It was already discussed that this introduces an uncertainty to the extracted $\Gamma_{\text{long}}(T)$ values. On the other hand, however, the 2 ML fit seems to capture a further increase of $\Gamma_{\text{long}}(T)$ at around 90 K, which could stem from an activation of the upper bright level B2.

Sample	Γ_D	Γ_{B1}	γ_{1D}	γ_{2D}	γ_{21}	Γ_{B2}	ΔE_1	ΔE_2
2ML	0.001195	9.202	7220.27	3.46e−19	7.60e−14	377.5	37.18	52.87
3ML	0.000647	1.762	1.36439	118.4	4.034	0.101	20.98	32.16
4ML	0.001444	1.316	0.07565	15.87	75.35	0.116	11.53	24.68
5ML	0.001852	1.158	0.03569	2979.0	4.934	0.131	7.591	18.66
6ML	0.001267	1.943	0.01444	105.4	1.824	0.257	5.575	14.30
8ML	0.000773	190.2	2.80e−34	0.886	30.17	29.77	3.581	8.835

Table 4.3: Three-Level Model Fit Parameters. The parameters of the decay model Γ_D, Γ_{B1}, γ_{1D}, γ_{2D}, and γ_{21} fit to the experimental data. Also shown are ΔE_1 and ΔE_2, which were not extracted from the fits but rather fixed to the theoretical values stemming from the effective mass model, and Γ_{B2} which is fixed based on the fitted Γ_{B1} and the calculated ratio of radiative decay rates. All parameters are given in ns^{-1} except ΔE_1 and ΔE_2, which are in meV.

With five free parameters the fit is still rather qualitative than quantitative. It demonstrates, however, that the theoretically calculated splitting energies can also explain the TR-PL data and that the limitation to only one bright state is likely the flaw of describing the data with a two-level model.

Lastly, the temperature range in which $\Gamma_{\text{long}}(T)$ begins to increase coincides with the temperature range of the spectral shift for each thickness. To be more rigorous, however, it can be checked, whether the extracted rates are able to reproduce the exact temperature-dependence of the steady-state spectrum, which we analyzed in Section 4.3. To theoretically calculate the spectra from the rates, one only needs to make assumptions on the initial occupation of the states directly upon excitation, the PLQY of the states, and finally the lineshape of the broadened emission. First, for reasons discussed in the beginning of this section, the 1s exciton fine structure states in a NPL ensemble are presumed

to be equally populated upon relaxation from the excited continuum states. Second, the PLQY of all states is set to unity. This might not resemble reality, however, the data does not point towards a much lower PLQY for the dark state compared to the bright states, the decay is just significantly slower. Third, we assume a normal distribution with a full-width at half-maximum (FWHM) of 35 meV for the dark state and 25 meV for the bright states. These values are extracted from the measured spectra. Combining those assumptions with the rates shown in Table 4.3, the time-integrated steady-state PL spectra are calculated. Figure 4.15 depicts the resulting temperature-dependent PL spectra normalized to a total intensity of one for each spectrum in the form of PL maps.

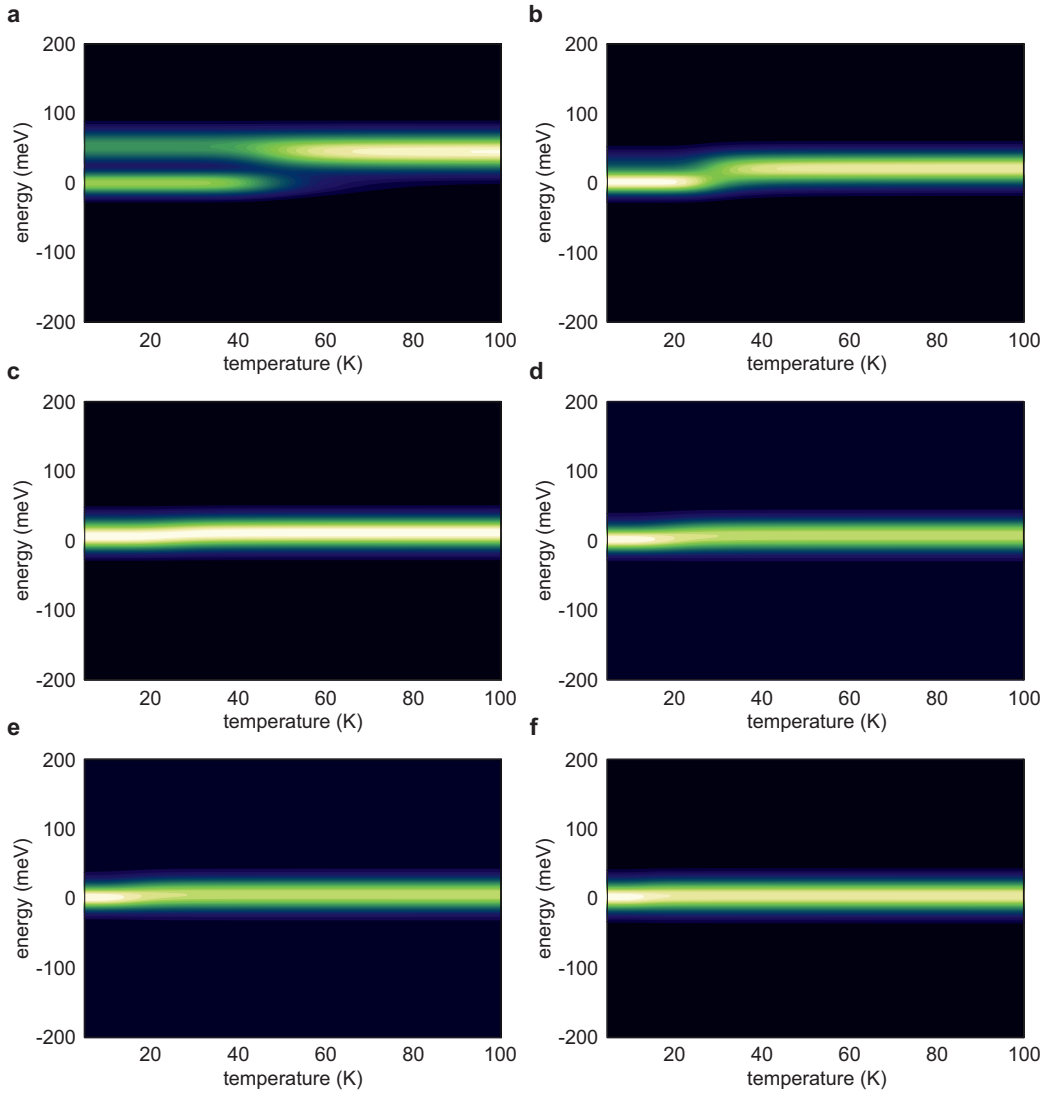

Figure 4.15: Theoretical Temperature-Resolved Photoluminescence Spectra. The steady state spectra are calculated from the rates in Table 4.3. Additionally, assumptions on the initial occupation of the states directly upon excitation, the PLQY of the states, and finally the lineshape of the broadened emission have to be made. In the calculations the states is presumed to be populated equally upon excitation, the PLQY is set to unity for all states and the FWHM is fixed to 35 meV for the dark state and 25 meV for the bright states. The resulting PL maps display good agreement to the experimentally acquired PL maps, which are presented in Figure 4.5.

Especially visible for the 2 ML and 3 ML NPLs, the calculated PL maps show striking agreement to the experimentally acquired ones, depicted in Figure 4.5. The only notable difference is the non-vanishing bright state emission at temperatures lower then 40 K for the 2 ML NPLs. This stems from a fitting artifact during the rate extraction: The splitting energy stemming from the effective mass model

seems too high in the case of the 2 ML NPLs. Therefore, the increase of $\Gamma_{\text{long}}(T)$ in the fit initiates at a too high temperature, as can be observed in Figure 4.14. The overestimation of the splitting energies causing this probably stems from the hard wall boundary condition in the effective mass model neglecting any wave function leakage. As a result, however, the fit in Figure 4.14 decouples the state B2 from B1 and D completely, which manifests in vanishingly small γ_{2D} and γ_{21} values. Thus, the complete initial exciton population in that state recombines and emits photons rather than transferring into the dark state.

4.5 Summary and Discussion

This study reveals and quantifies the strong influence of shape anisotropy on the exciton fine structure of $Cs_{n-1}Pb_nBr_{3n+1}$ NPLs. The experimentally deduced excitonic bright-dark splitting values range from 1.8 meV for 8 ML up to 32.3 meV for 2 ML NPLs, constituting the largest value ever observed in semiconductor nanocrystals. Thus, an effective mass model was developed to describe the influence of the shape anisotropy on the exciton fine structure theoretically. A comparison of the result to the experimental values validates that the large bright-dark splitting does indeed stem from the strong confinement in the thickness dimension of the NPLs. Furthermore, the model predicts an additional large splitting of the bright in-plane and out-of-plane polarized exciton states. To check this experimentally, we demonstrate that the TR-PL data can be explained with a model, which takes the bright level splitting into account, while a model with one degenerate bright level fails to reproduce the correct splitting energies. As a final verification, the extracted decay and transition rates from this model are then employed to reproduce the spectral behavior theoretically.

In two previous studies we had observed a faster PL decay of the 3 ML NPLs compared to the 2 ML NPLs at room temperature.[10,93] Since the 3 ML NPLs also have a higher PLQY, their faster PL decay has to stem from an increase in the radiative decay rate. This contrasts findings for quantum wells, in which an increase in quantum confinement stemming from a decrease in thickness accelerates the radiative decay of excitons.[71] However, the contradiction is lifted by the insight into the fine structure. Due to the increased bright-dark splitting of a 2 ML NPL, the excitons spend more time in the dark state than in a 3 ML NPL, even at room temperature. The actual decay rate of the bright states is, thus, prolonged by a feeding from the dark state.

Furthermore, the novel theoretical model shows that the large splitting simply results from the electron-hole exchange interaction in combination with the unique material parameters of LHPs. The model could be further refined by the addition of the crystal structure anisotropy. To include it, however, the alignment of the orthorhombic crystal axes within the NPLs has to be determined. Importantly, the new model can be generalized to any anisotropically shaped nanocrystal system and help to unravel its excitonic fine structure.

The potential of anisotropically shaped nanocrystals in lighting applications is enhanced by a possible anisotropic light emission, which can be employed to increase the out-coupling efficiency of LEDs or displays. Interestingly, our model predicts a crossing of the in-plane and out-of-plane bright states between 2 ML and 3 ML NPLs. This could mean that the light emission is stronger in directions parallel to the NPL plane for 2 MLs, while it is stronger perpendicular to this plane for the other thicknesses.

To investigate this, further experiments either on single NPLs or on ordered thin films of NPLs are necessary.

Lastly, it shall be mentioned that an inversion of the bright and dark state was recently observed for $CsPbBr_3$ nanocubes.[32] While it is still under dispute, if this holds true for the material they investigated, it is theoretically possible that nanocrystals exist, in which the lowest exciton state is bright. The exact knowledge of the crystal shape and size influence on the exciton fine structure is, thus, highly important in the search for such a material.

5

Exciton-Phonon Coupling

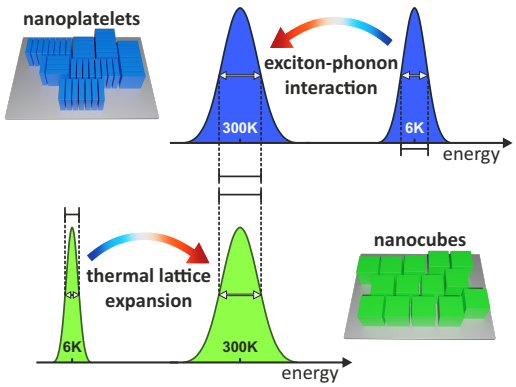

This chapter investigates the interaction between excitons and phonons in $Cs_{n-1}Pb_nBr_{3n+1}$ NPLs. A narrow room temperature emission linewidth is a prerequisite for many lighting applications and exciton-phonon coupling governs the temperature-induced contribution to spectral broadening. To quantify this effect, we analyze the temperature dependence of the PL in terms of linewidth and spectral position. Surprisingly, 2 ML NPLs display a red-shift of the PL with increasing temperature, the 3 ML NPLs no overall shift and only thicker NPLs show the blue-shift typical for perovskites of this composition. Additionally, the linewidth broadening also depends on NPL thickness with the 2 ML NPLs possessing the lowest temperature-induced broadening at room temperature. A combination of exciton-phonon coupling and thermal lattice expansion is determined to explain both effects. Interestingly, the 2 ML NPLs possess a strongly increased optical phonon energy and Fröhlich coupling constant. This could be connected to the inversion of the bright exciton fine structure levels between 2 ML and 3 ML NPLs predicted in the last chapter. These results illustrate the potential of ultrathin lead halide perovskite NPLs towards narrow blue light emission at room temperature. The results and all figures presented in this chapter have been published in the Journal of Physical Chemistry Letters in 2021 [94].

5.1 Temperature Influence on Photoluminescence

The last chapter expanded our insight into excitons in $Cs_{n-1}Pb_nBr_{3n+1}$ NPLs on a fundamental level by unraveling and quantifying the excitonic fine structure. In other words, the inherent properties of a single exciton in a NPL were investigated. Building on this knowledge, this chapter and the next chapter ask the question, how such an exciton interacts with further (quasi-)particles. In this chapter the focus lies on its interaction with phonons and, in particular, how thermally induced linewidth broadening governed by exciton-phonon coupling is influenced by the NPL thickness.

The thickest NPLs investigated here are the 5 ML NPLs. Since a very high homogeneity of the samples is of great importance in this study, thicker NPLs were omitted, as homogeneity tends to decrease with thickness. In exchange, nanocubes of the same composition with an edge length comparable to the NPLs lateral size were included. These are very homogeneous and basically serve as the upper thickness limit (14 nm, which correspond to roughly 24 ML). The synthesis route and subsequent characterization of those nanocubes can be found in Section 3.1. Figure 5.1 depicts the 300 K spectra (lines) as well as the 6 K spectra (filled) for all investigated samples. Notably, the 5 ML NPLs possess an additional PL peak at around 2.3 eV, which corresponds to the band gap of bulk $CsPbBr_3$. This peak is, however, split far enough from the main PL peak to not affect the correct extraction of its position and width. In contrast, the 4 ML NPL main PL peak has a slight shoulder on the low energy side, which can affect the correct extraction of its position and increases its width.

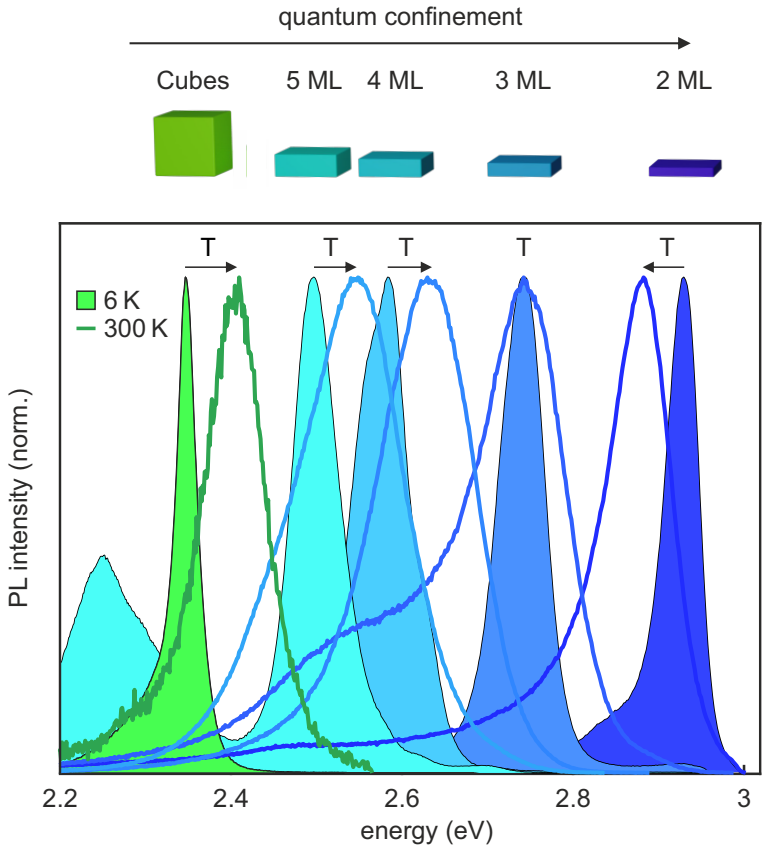

Figure 5.1: Room and Cryogenic Temperature Photoluminescence Spectra. For each NPL thickness and the nanocubes the 300 K spectrum (lines) as well as the 6 K spectrum (filled) of a thin film is plotted. Whereas nanocubes, 5 ML and 4 ML NPLs show the LHP-typical overall blue-shift, 3 ML NPLs display no shift and 2 ML NPLs a red-shift with increasing temperature.

In Subsection 2.4.1 the band gap increase with rising temperature typical for LHPs was discussed. This expected trend, however, is only present for the nanocubes as well as the 5 ML and 4 ML NPLs. In contrast, the 3 ML NPLs display no overall shift between 6 K and 300 K and the 2 ML NPLs even red-shift with increasing temperature. To visualize the differences between the room temperature and low temperature spectra, the energetic position of the PL maximum and the FWHM of each spectrum are extracted. The resulting differences $\Delta E_{PL} = E_{PL}(300K) - E_{PL}(6K)$ and $\Delta FWHM = FWHM(300K) - FWHM(6K)$ are plotted in Figure 5.2 and Figure 5.3, respectively. Figure 5.2 illustrates the aforementioned overall PL shifts nicely. While ΔE_{PL} is positive for the 4 ML and 5 ML NPLs as well as for the nanocubes, it is near zero for the 3 ML NPLs and negative for the 2 ML NPLs.

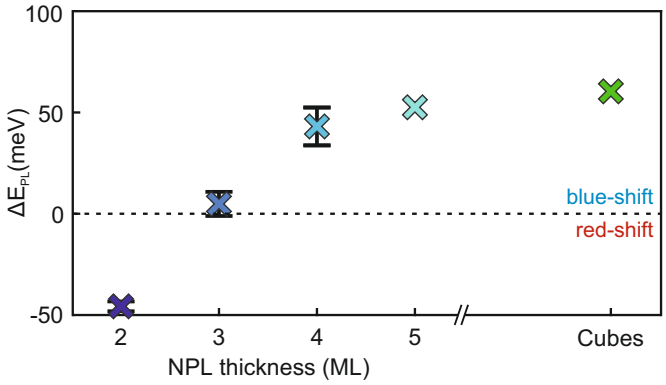

Figure 5.2: Thermal Photoluminescence Shift. The difference in PL maximum position ΔE_{PL} between 6 K and 300 K for all samples. Positive values correspond to a blue-shift of the PL maximum position with increasing temperature.

The total temperature-induced broadening ΔFWHM is depicted in Figure 5.3. This analysis reveals that the thermally induced linewidth broadening is strongly dependent on the NPL thickness. As a result, ΔFWHM is even lower for the 2 ML NPLs than for the nanocubes, which are known to possess a very narrow room temperature linewidth.[7]

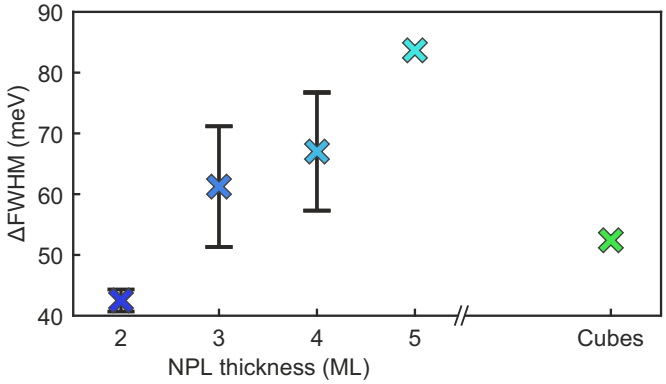

Figure 5.3: Thermal Photoluminescence Broadening. The difference in the FWHM of the main PL peak ΔFWHM between 6 K and 300 K for all samples.

Comparing the total FWHM at 300 K, the 2 ML NPLs and the nanocubes are rather similar with values of 86 meV/12.9 nm and 81 meV/17.5 nm, respectively, as shown in Figure 5.4. However, the temperature-dependent (colored) and temperature-independent (grey) contributions differ.

This demonstrates that the 2 ML NPLs have the potential to become the narrowest room temperature light emitters among those samples including the nanocubes, once their homogeneity in the lateral dimensions and surface are improved. Inhomogeneity in the thickness dimension is unlikely to cause

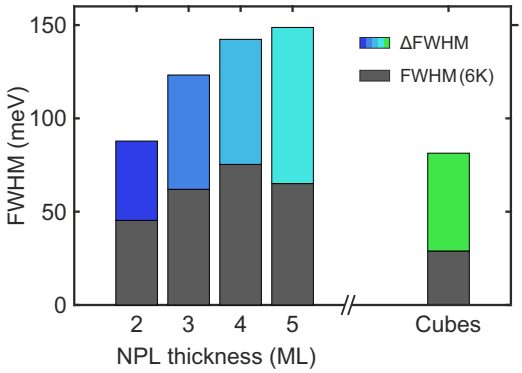

Figure 5.4: Photoluminescence Broadening Contributions at 300 K. Temperature-dependent (colored) and temperature-independent (grey) contributions to the total FWHM of the room temperature PL peak. While the FWHM at 6 K, which is mainly governed by inhomogeneous broadening, is smallest for the nanocubes, the 2 ML NPLs possess a similar FWHM at 300 K due to a reduced temperature-dependent contribution.

the inhomogeneous broadening of the 2 ML NPL PL peak, since the smallest increment is a full ML, which would result in an additional PL peak rather than a mere broadening of the existing PL peak. To improve our general understanding of LHP nanocrystals and the NPL system in particular, however, we are interested in the reasons for the strongly decreased temperature-induced linewidth broadening in 2 ML NPLs. As thermally induced broadening is connected to exciton-phonon interaction, such an investigation should give insight into the properties of phonons in LHP NPLs.

5.2 Temperature-Dependent Linewidth

To shed light on the exciton-phonon interaction, spectra were acquired for all samples at different temperatures between 6 K and 300 K. The extracted FWHM values for each thickness and temperature are plotted in Figure 5.5. For clarity, values corresponding to different samples are offset vertically, since the exact values for the FWHM at 6 K can be taken from Figure 5.4. Notably, the 2 ML as well as the 3 ML NPLs display a discontinuity in the FWHM below 60 K. This stems from the exciton fine structure investigated in the last chapter. In a certain temperature range the PL originates from both, dark and bright level emission, and the extracted FWHM is broadened. In the 3 ML NPLs the dark state emission is even inherently broader than the bright state emission, which increases the FWHM down to 6 K. This has been observed in the last chapter, the reason for the broadened dark state emission, however, remains unknown. Furthermore, a discontinuity at around 280 K emerges for the 2 ML NPLs, the origin of which will be discussed in the next section (Section 5.3). Both of those discontinuities, however, do not impede the analysis of the temperature-dependence of the FWHM.

The theoretical background on phonons and the different broadening mechanisms connected to exciton-phonon interaction is given in Subsection 2.2.5. Many other studies have identified the interaction with longitudinal optical (LO) phonons as the dominant source of thermally induced linewidth broadening in LHPs.[10,91,95] It shall be noted that some studies also observed a contribution of an interaction with acoustic phonons.[96–99] As can be seen from Equation 2.23, such an interaction would manifest in a linear increase of the FWHM already starting at 0 K, since the acoustic dispersion relation allows for very low energy phonons. Figure 5.5 reveals, however, that the FWHM is constant up to a certain temperature in all samples, which renders the interaction with acoustic phonons

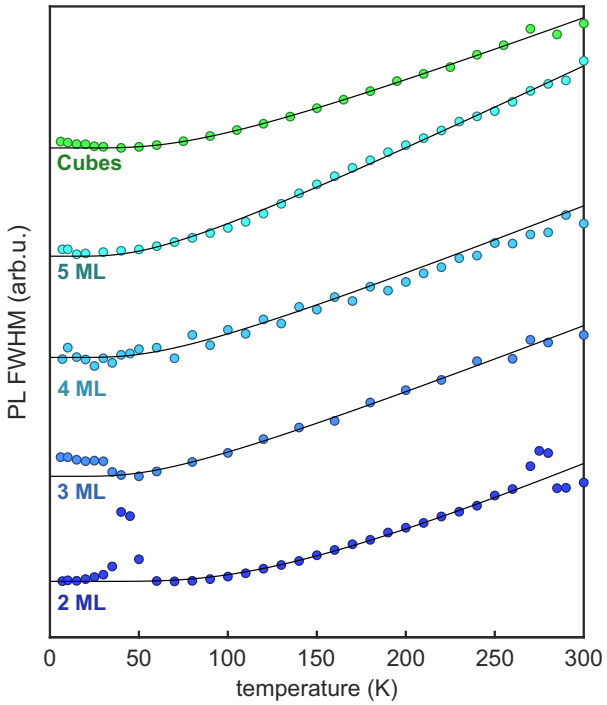

Figure 5.5: Temperature Dependence of Full-Width Half-Maximum. The FWHM is plotted as a function of temperature for each sample. The different samples are offset vertically for clarity. The absolute value of the respective FWHM at 6 K can be found in Figure 5.4. The black lines represent fits to the data according to Equation 5.1.

negligible in the NPLs and the nanocubes. Accordingly, only the term describing the interaction with optical or more specifically LO phonons $\Gamma_{LO}(T)$ is added to the temperature-independent Γ_0 (see Equation 2.23) to describe the data:

$$\Gamma(T) = \Gamma_0 + \Gamma_{LO}(T) = \Gamma_0 + \frac{\gamma_{LO}}{\exp\left(\frac{E_{LO}}{k_B T}\right) - 1} \tag{5.1}$$

Fits to the temperature-dependent FWHM according to Equation 5.1 are shown as black lines in Figure 5.5. Γ_0 had to be fixed, due to the dark level being broader in the 3 ML for example, as already discussed, leaving only two free parameters, γ_{LO} and E_{LO}. The agreement of the resulting fits to the data is good and justifies the reduction of the formula to LO phonons. Γ_0 includes the natural linewidth as well as inhomogeneous broadening stemming from the distribution of different nanocrystals. The parameter E_{LO} indicates the optical phonon energy of the phonons involved in the broadening. Here, the slight dispersion of optical phonons (see Figure 2.15) is generally neglected and the phonon energy assumed to be a constant. Lastly, γ_{LO} is the so-called Fröhlich coupling constant, which denotes the strength of the interaction between excitons and LO phonons. The values γ_{LO} and E_{LO} extracted from the fits are plotted in Figure 5.6 a and Figure 5.6 b, respectively.

Both values are slightly decreased in the 3 ML to 5 ML NPLs compared to the nanocubes. Nevertheless, the γ_{LO} values lie all between 56 meV and 73 meV and the E_{LO} values lie between 14 meV and 22 meV and are, thus, very similar to other literature values reported for bulk LHPs or LHP nanocubes.[95,96,100] Surprisingly, however, both values are strongly increased in the 2 ML NPLs. The high LO phonon energy in 2 ML NPLs leads to a smaller phonon population at any given temperature and a higher temperature necessary to activate those phonons. This can be nicely observed in Figure 5.5: The

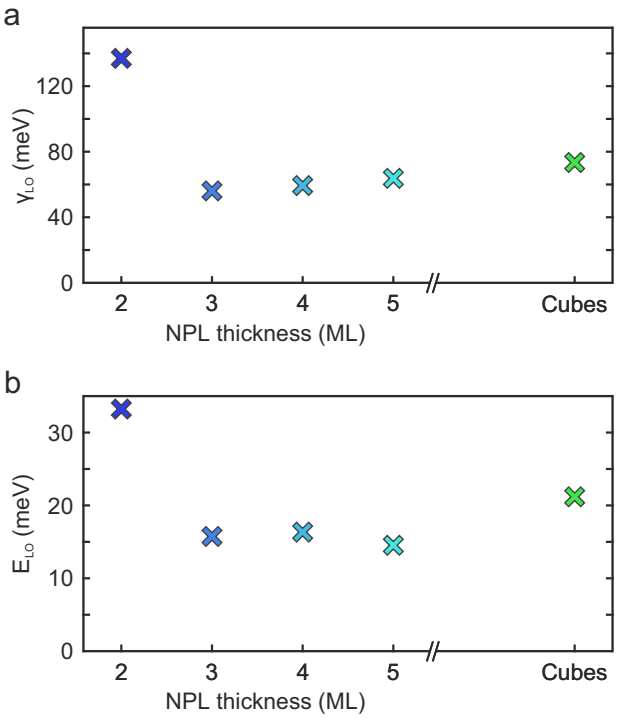

Figure 5.6: Fröhlich Interaction. The Fröhlich interaction between excitons and LO phonons is described by **a)** the coupling strength between the two quasiparticles γ_{LO} and **b)** the LO phonon energy E_{LO}. Both of these properties are strongly enhanced in the 2 ML NPLs.

FWHM of the 2 ML NPLs starts to deviate visibly from Γ_0 at around 20 K to 30 K higher than in the other samples. While the additionally increased interaction with the LO phonons γ_{LO} counteracts this partially, the overall temperature-induced broadening is significantly decreased. This results in our initial observation from Figure 5.3 that the total temperature-induced broadening between 6 K and 300 K is the lowest in the 2 ML NPLs.

5.3 Temperature-Dependent Photoluminescence Peak Position

To gain further insight into the exciton-phonon interaction in these nanocrystals, we analyze the temperature dependence of the energetic position of the PL maximum. This position is extracted from all acquired spectra and plotted in Figure 5.7 for all samples. The large low temperature shift below 50 K in the thinner NPLs stems from the exciton fine structure, which was discussed in-depth in the last chapter. In addition, however, a second discontinuity emerges in the form of a red-shift in the NPLs starting at around 270 K. Similarly, it is thickness-dependent and by far the strongest in the 2 ML NPLs. This effect stems from a reorganization of the organic ligands, which cover the NPLs and fill the space in between them in a thin film. Their pure melting temperatures are 13 °C to 14 °C and 18 °C to 26 °C (oleylamine and oleic acid, respectively), but these temperature ranges can be altered by the mixture and attachment to the NPL surface. Naturally, such a change in the environment affects excitons in thinner NPLs the strongest, as a larger dielectric confinement increases the influence of the external dielectric constant. To test this hypothesis, we dilute the 3 ML NPLs 1:5 in a ZEONEX (480R) polymer solution prior to spin-coating. In the resulting film the NPLs are, thus, embedded in a polymer matrix. While there are still ligands attached to the surface of the NPLs, their environmental influence should be reduced. In Figure 5.8 the PL emission maximum shift of this polymer film (grey circles) is

plotted in addition to the data of two unaltered 3 ML NPL films (blue circles). The PL data of one of the two standard 3 ML NPL films is also the one shown in Figure 5.7. To enable a good comparison of the shift above 270 K, all data sets are offset to overlap in the range of 100 K to 150 K. This reveals, on the one hand, that the red-shift above 270 K is very reproducible for pristine films, as all blue data points show the same trend, while they originate from two different films. On the other hand, the shift is reduced in the NPLs in the polymer film. Thus, our assumption is corroborated that the high temperature PL shift in the thinner NPLs is in fact connected to the melting of the ligand environment. It should be noted here that this effect also caused a discontinuity in the temperature-dependent FWHM analysis in the last section, the discussion of which references this paragraph.

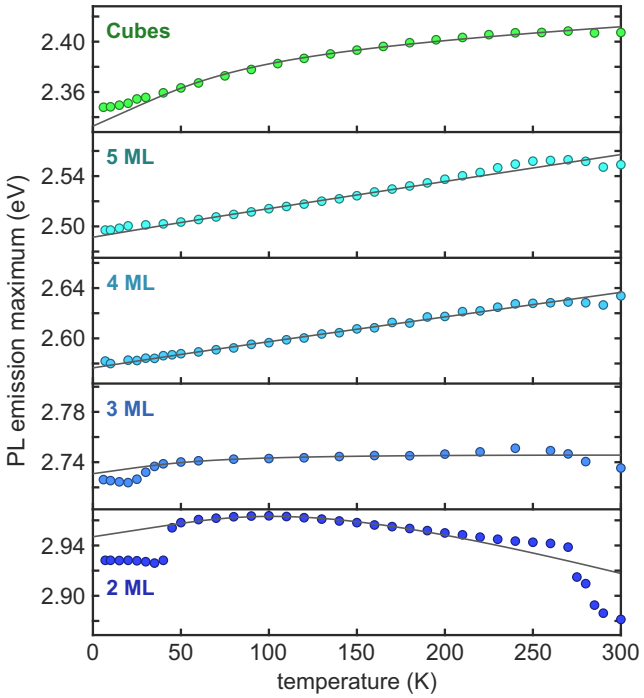

Figure 5.7: Temperature Dependence of Peak Position. The temperature-dependent energetic position of the PL emission maximum is plotted for each sample. The black lines represent fits to the data according to Equation 5.2.

After determining the origins of the discontinuities in the temperature dependence of the PL maximum position, we can focus on the temperature intervals in which the trend seems to be continuous. If we assume the exciton binding energy to be temperature-independent, this continuous shift should resemble the temperature dependence of the band gap. Then, a quasi-harmonic approximation allows for expressing the band gap energy $E_G(T)$ as:[91,101–104]

$$E_G(T) = E_G(0) + A_{TE}T + A_{EP}\left[\frac{2}{\exp\left(\frac{E_{ph}}{k_B T}\right) - 1} + 1\right] \tag{5.2}$$

Here, A_{TE} and A_{EP} describe the influence of thermal lattice expansion, also termed thermal expansion interaction, and exciton-phonon interaction on the band gap, respectively. While the influence of thermal expansion is linear in temperature, the exciton-phonon interaction is again proportional to the population of the phonons responsible for the interaction, which follows Bose-Einstein statistics. We fix the corresponding phonon energy E_{ph} to the respective LO phonon energy E_{LO} extracted from the temperature dependence of the FWHM (see Figure 5.6) and fit the data in Figure 5.7 employing

Equation 5.2 with the two remaining free parameters A_{TE} and A_{EP}. As the fit displays good agreement with the continuous shift of the PL emission maximum in between the discussed discontinuities, we can assume that setting $E_{ph} = E_{LO}$ is correct. Consequently, we can further assume that the FWHM broadening and the PL peak shift are both mainly governed by the interaction with the same LO phonon modes.

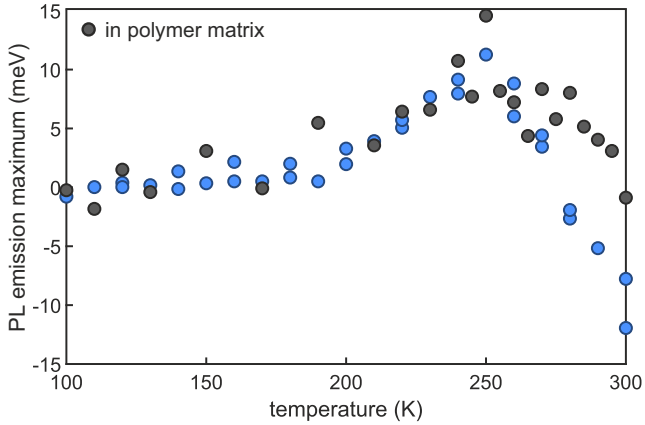

Figure 5.8: 3 ML NPLs NPLs in Polymer Matrix. The temperature dependence of the PL emission maximum position of 3 ML NPLs embedded in a polymer matrix (black circles) and in a pristine film with many unbound ligands within the NPL layer (blue circles) are compared. The pristine film data consists of measurements on two films, which includes the film presented in Figure 5.7. To enable a comparison of the trend above 250 K, the curves are offset to overlap between 100 K and 150 K. As a result, a strongly diminished red-shift above 250 K can be observed.

The coefficients A_{TE} and A_{EP} resulting from the fits are plotted in Figure 5.9 a and Figure 5.9 b, respectively. A_{TE}, the influence of thermal lattice expansion, is reduced in NPLs compared to nanocubes but does not really depend on the NPL thickness. A_{EP}, the influence of exciton-phonon interaction, however, varies strongly for the different NPL thicknesses. Furthermore, it is significantly stronger in the nanocubes than in all NPL thicknesses except the 2 ML NPLs. In the 4 ML and 5 ML NPLs, the band gap shift is completely dominated by the thermal expansion interaction, hence, the expected overall blue-shift is observed. It must be mentioned, however, that the extracted A_{EP} values might be slightly underestimated for those two thicknesses and are caused by the near linear increase of their PL emission energy with temperature. This in turn could originate from the crystal shape inhomogeneities present in thicker NPLs, which not only cause a Gaussian broadening of the PL linewidth, but are especially visible in the low-energy shoulder of the 6 K PL peak of the 4 ML NPLs in Figure 5.1. The extracted PL emission maximum position might not represent the band gap of the same subensemble of NPLs at every temperature, which introduces an error. In the 3 ML NPLs, the thermal expansion interaction and the exciton-phonon interaction overall counterbalance each other resulting in the near-zero net shift of the PL peak between 6 K and 300 K depicted in Figure 5.2. The vastly increased exciton-phonon interaction strength and LO-phonon energy in 2 ML NPLs already observed in the FWHM analysis, however, are confirmed by the temperature-dependent band gap shift. Here, the strong exciton-phonon interaction exceeds the rather weak thermal expansion interaction and causes the (for LHPs atypical) overall red-shift between 6 K and 300 K. This unique behavior could be connected to the composition of the exciton population. As shown in the last chapter, the theoretical description of the exciton fine structure via an effective mass model predicts a crossing of the bright in-plane (X/Y) and bright out-of-plane (Z) excitons at a thickness between 3 MLs and 2 MLs. As a result, only in the 2 ML NPLs the lowest bright excitonic level is the Z-level. Since an LO phonon in a

polar crystal induces an oscillating macroscopic electric field with which the excitons interact, the polarization direction of the excitons in respect to the NPL geometry should be important for the interaction. Furthermore, an exciton might interact predominantly with a different phonon mode, if it is polarized out-of-plane compared to in-plane. Summing up, a different average distribution of the excitons in a NPL ensemble across the excitonic fine structure can indeed affect the LO phonon mode mainly interacting with those excitons and, in turn, also affect the LO phonon energy and interaction strength, which determine the room temperature FWHM.

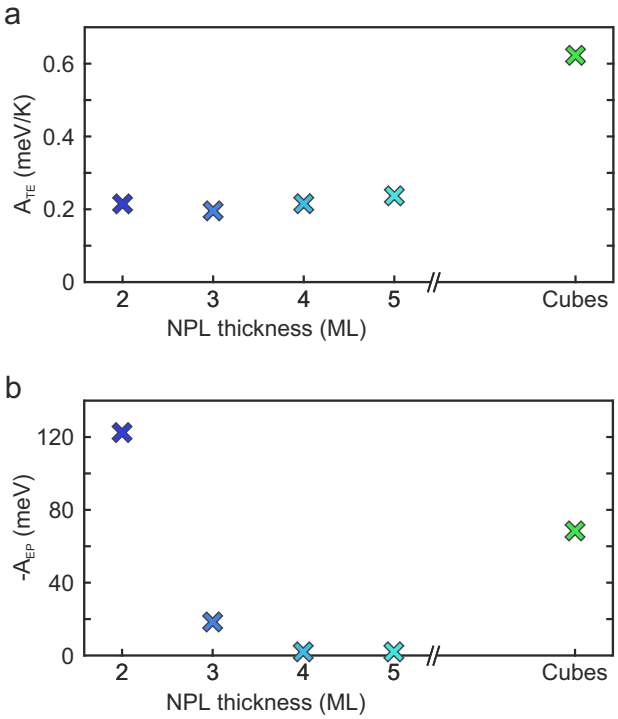

Figure 5.9: Thermal Expansion Interaction and Exciton-Phonon Interaction. The contributions to the temperature-dependent band gap shift are encoded by **a)** the parameter A_{TE} describing the so-called thermal expansion interaction and **b)** the parameter A_{EP} describing the exciton-phonon interaction. While A_{TE} is comparable in all NPLs, A_{EP} is strongly increased in the thinner NPLs.

Lastly, prior to concluding this chapter, the reproducibility of the temperature-dependent PL measurements shall be discussed. Since cryogenic PL measurements with small temperature increments are quite time consuming, large statistics are hard to acquire. Important measurements, however, were repeated on completely different synthesis batches to verify the reproducibility of the observations. To that end, Figure 5.10 a and Figure 5.10 b display the temperature dependence of the FWHM and the PL emission maximum energy, respectively, for two different samples of each, 2 ML, 3 ML and 4 ML NPLs. Additionally, fits of the data according to Equation 5.1 and Equation 5.2 are added as black lines. Importantly, the main features connected to the conclusions drawn are very reproducible. In particular, the steep low and high energy shifts in the thinnest NPLs stemming from the exciton fine structure and the ligand melting, respectively, are of comparable magnitude in both samples. Furthermore, the deviation of the FWHM from Γ_0, which occurs in the 2 ML NPLs at a higher temperature than in the other samples and, thus, points towards an increased LO phonon energy, can be observed nicely in both 2 ML samples. Also, the overall red-shift, no-shift and blue-shift of 2 ML, 3 ML and 4 ML NPLs, respectively, are very reproducible. Only in the thicker NPLs, the exact band gap shift deviates between the two measurements. It was already discussed that in thicker samples the homogeneity within the measured NPL ensemble decreases. While Figure 5.10 b reveals that the reproducibility

also decreases between different synthesis batches for thicker NPLs, for all thicknesses d $\geq$ 4 ML one always observes a clear overall red-shift of the PL with temperature, which is never observed in 2 ML and 3 ML NPLs.

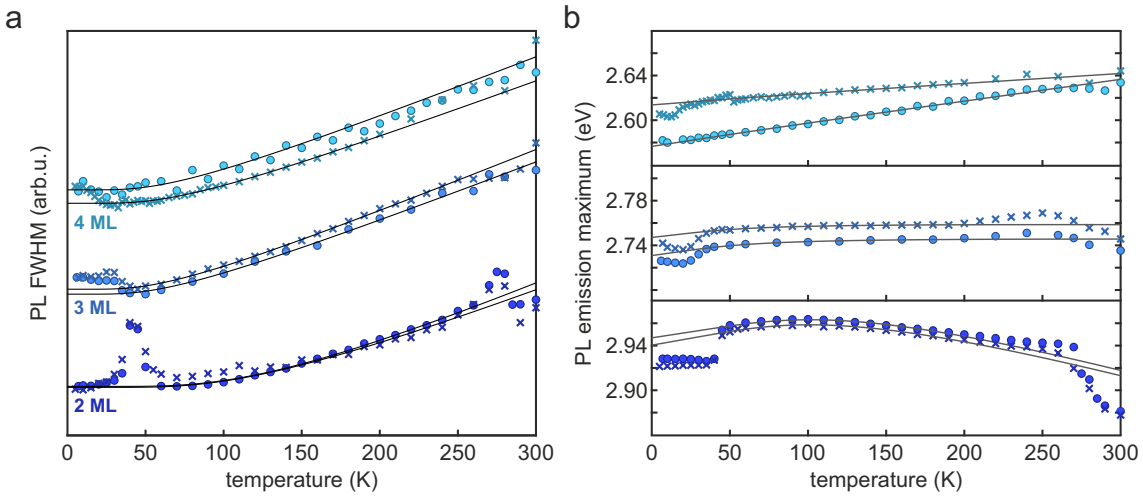

Figure 5.10: Reproducibility of Temperature-Dependent Photoluminescence Spectra. The temperature-dependent PL measurements presented in this and the last chapter are repeated on different synthesis batches and yield the same results. Especially important features in the thinner NPLs are observed in every measurement series.

5.4 Summary and Discussion

This study investigates the thickness dependence of exciton-phonon interaction in $Cs_{n-1}Pb_nBr_{3n+1}$ NPLs. An analysis of the temperature-dependent FWHM of the PL emission peak reveals a strongly increased LO phonon energy as well as an increased Fröhlich coupling of excitons to those phonons in the 2 ML NPLs. These observations are then confirmed by the temperature dependence of the band gap. Ultimately, this effect causes a (for perovskites atypical) overall red-shift of the PL spectrum with temperature in 2 ML NPLs and no overall shift in 3 ML NPLs. The expected blue-shift occurs only in thicker NPLs. Furthermore, the increased LO phonon energy in 2 ML NPLs results in those NPLs displaying the smallest temperature-induced broadening at 300 K, even compared to nanocubes of the same composition. A possible explanation of this surprising behavior of the 2 ML NPLs could be tied to the inversion of the in-plane and out-of-plane bright exciton levels revealed in the last chapter, which originate from the strong thickness confinement.

Whatever the exact reason for the reduced PL linewidth broadening is, the effect renders the 2 ML NPLs a promising candidate for very narrow room-temperature blue light emission - an important prerequisite for a larger color gamut in lighting or display applications.

6

Exciton-Exciton Annihilation

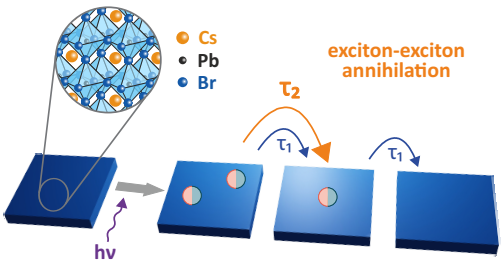

This chapter quantifies the exciton-exciton annihilation lifetime in $Cs_{n-1}Pb_nBr_{3n+1}$ NPLs. The non-radiative annihilation process is identified as the dominant decay pathway for excitons as soon as a NPL contains more than one exciton. While this poses no problem at moderate excitation densities, processes like lasing, which require high exciton densities, are very difficult to achieve. Since exciton-exciton annihilation affects many nanocrystal systems, its dependence on nanocrystal size is an important subject to study. In the $Cs_{n-1}Pb_nBr_{3n+1}$ NPLs, the corresponding lifetime seems to follow a power law dependence on thickness according to $\tau_2 \propto d^{5.3}$. Further measurements suggest that an increase in the lateral dimension also increases the lifetime. Combining the observations, the study shows that a precise control over all dimensions of a nanocrystal is necessary for deciphering the fundamental laws, which govern the exciton-exciton annihilation process in anisotropically confined nanocrystals. The results and all figures presented in this chapter have been published in the Journal of Physical Chemistry Letters in 2020 [105].

6.1 Differential Transmission Spectra

The last two chapters revealed and quantified the exciton fine structure and the exciton-phonon interaction, respectively. These are both properties which come into play at all excitation densities. To exemplify the exciton density in a film of 3 ML NPLs, we can calculate it for the case that every NPL contains exactly one exciton: If we assume that the semiconductor NPLs constitute half of the volume of the film with the space in between them filled by ligands, the exciton density would be roughly $1.4 \cdot 10^{18}$ cm^{-3}. While for standard light emission applications such an exciton density should be sufficient, very high brightness applications and especially lasing, which is enabled by a population inversion of the ground and excited states, can require higher excitation densities. Furthermore, the probability that two excitons occupy the same NPL for a short period of time is, naturally, already non-zero at lower exciton densities. This chapter investigates the consequences of multiple excitons existing in one NPL and identifies exciton-exciton annihilation (EEA) as the dominant process in that case. Background on the processes of EEA and Auger recombination, a similar process for free electrons and holes, can be found in Subsection 2.2.3.

Since EEA can occur on a picosecond timescale, the TCSPC technique employed to achieve time resolution in previous result chapters might be too slow to capture the process correctly. Thus, we turn to TAS for this investigation. More information on this technique can be found in Section 3.3. While this type of pump-probe setup is generally known as a transient absorption spectroscopy setup, the quantity plotted throughout this chapter is $\Delta T/T$. Such a spectrum is, thus, more appropriately called a differential transmission (DT) spectrum .

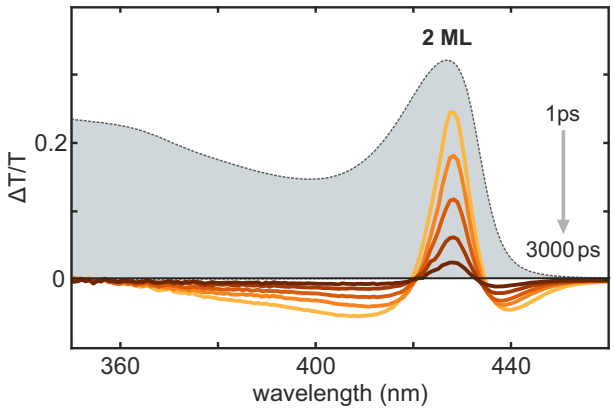

Figure 6.1: Differential Transmission Spectra. The DT spectra of a 2 ML NPL dispersion excited at 400 nm for different times between 1 ps and 3000 ps after excitation. Superimposed in grey is the linear absorption spectrum illustrating that the main peak of the $\Delta T/T$ signal occurs at the spectral position of the 1s exciton.

Furthermore, the analysis of the data requires the suppression of excitonic transfer processes between neighboring NPLs. For this reason the measurements were conducted on diluted NPL dispersions instead of NPL films, as in the preceding chapters. This also allows for the heat deposited by high optical excitation powers to dissipate faster and ensures that the NPLs are not damaged during the measurement. The dispersions were diluted to an OD of around 0.2 at the excitation wavelength of 400 nm to ensure a rather homogeneous excitation over the whole path length of the cuvette (2 mm) in which the dispersion is contained. Figure 6.1 displays exemplary DT spectra for different times ranging from 1 ps up to 3 ns after excitation of a 2 ML sample. While the excitation affects the transmission through the sample in different ways, the feature we are interested in is the so-called bleaching of

states: If an excited state is already occupied, the respective transition from the ground state to that excited state is not possible and the absorption of the semiconductor at that wavelength is reduced - or the transmission increased. Accordingly, the most prominent feature in the DT spectra is a bleaching peak, which is positive in $\Delta T/T$, and located at the spectral position of the 1s exciton peak in the superimposed absorption spectrum. Due to the 400 nm excitation wavelength of the 100 fs long pulses, primarily free electron-hole pairs are generated at $t = 0$. Since the excitonic bleaching peak reaches its maximum prior to 1 ps, however, relaxation into the excitonic 1s state appears to occur on an even faster timescale. This behavior is observed for all NPL thicknesses and is consistent with reports on the fast carrier cooling rates of LHP NPLs.[70]

6.2 Determination of Initial Exciton Density

Since EEA is a exciton density dependent process, a comparison of the corresponding lifetime between samples is only possible if the respective exciton densities are known. In a large semiconductor system, such a lifetime is often simply given as a density dependent quantity. In a nanocrystal, however, the number of generated excitons is small ($N = 0, 1, 2, 3, 4...$) and the EEA lifetime becomes quantized ($\tau_2, \tau_3, \tau_4...$).[33] To enable the extraction of one of these lifetimes and then compare it between samples, the initial exciton density has to be determined first.

Subsequent to the fast formation of a 1s exciton population in the NPL ensemble dispersed in solution, the decay of this population takes place and is probed up to a time $t = 3000$ ps, which is the limit of the TAS setup. The spectra acquired at different times after excitation in Figure 6.1 visualize this. Corresponding time traces of data for 2 ML NPLs displaying the temporal evolution of the bleaching peak maximum are shown in Figure 6.2. Here, the different curves represent different excitation densities and delay times $t \geq 1$ ns are plotted in a second graph to improve the comparability of the curves on this time scale.

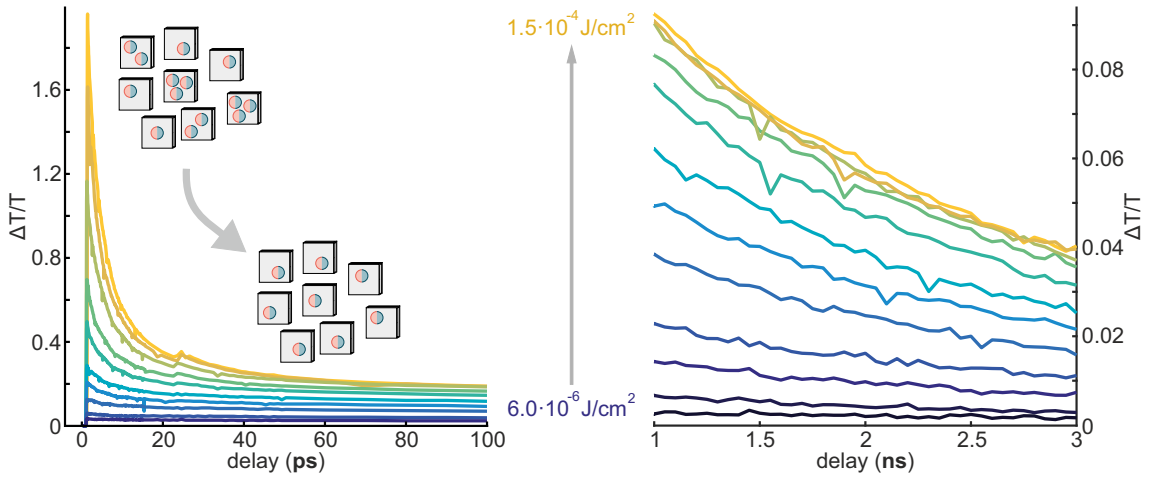

Figure 6.2: Decay of the Exciton Population. The decay of the excitonic bleaching peak maximum in 2 ML NPLs is depicted for different excitation densities (or rather pump pulse energies). With increasing excitation density a fast decay component within the first tens of picoseconds develops, which is attributed to EEA. While the intensity of this component increases for all excitation densities, the signal at times $t \geq 1$ ns saturates from a certain excitation density upwards. This effect is a result of EEA, which causes the fast annihilation of all excess excitons generated by even higher excitation densities, if all NPLs are already excited with a high probability at $t = 0$.

Interestingly, a fast decay component in the first tens of picoseconds develops with increasing excitation density, which we assign to EEA. Notably, the intensity of this component is increased further by every excitation density increase, while the signal at times $t \geq 1$ ns saturates from a certain excitation density upwards. This strongly suggests that the fast decay component is indeed EEA and that the saturation occurs for excitation densities for which each NPL in the excitation volume is nearly assuredly excited at least once. A further increase of the excitation density at this point still increases the number of generated excitons at $t = 0$, however, all excess excitons decay rapidly via EEA until at maximum one exciton per NPL remains after a few tens of picoseconds. Furthermore, it is meaningful to normalize the decay curves at a time after EEA is practically over. Thus, in Figure 6.3 the decay curves of the exciton population in the 2 ML NPL dispersion corresponding to different excitation densities are normalized to their value at 1 ns after excitation. This demonstrates that the dynamics in the first tens of picoseconds are affected by the excitation density, while the subsequent decay follows the same monoexponential curve for all excitation densities, further verifying that at maximum one exciton is left per NPL in that regime.

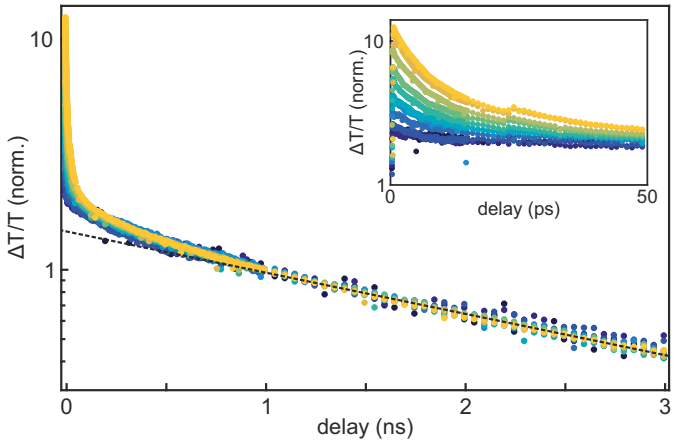

Figure 6.3: Monomolecular Decay. If the decay curves of the exciton population in a 2 ML NPL dispersion are normalized at 1 ns, the same exponential decay is revealed for all excitation densities at later times. This stems from the fact that only monomolecular decay is possible for $t \geq 1$ ns, as at maximum one exciton is left per NPL due to the fast EEA and the NPLs are not able to interact in the diluted dispersion. The inset depicts the first 50 ns more closely and demonstrates that the curves differ on that timescale.

The saturation behavior with excitation density for $t \geq 1$ ns, which can be observed in Figure 6.2, is utilized here to determine the initial excitation density $\langle N \rangle$, which describes the average number of excitons generated per NPL by the pump pulse. To that end, the signal between 1 ns and 3 ns is averaged and plotted against excitation density in Figure 6.4. It should be noted that the extracted saturation behavior is in principle the same at all times $t \geq 1$ ns, since all decay curves follow the same monoexponential decay in that regime and the ratio between the curves is, thus, constant. By averaging the signal from 1 ns to 3 ns, however, experimental noise can be reduced. As it was already discussed above, the signal in this time regime is proportional to the number of NPLs, which were excited at least once and the saturation sets in at excitation densities for which nearly all NPLs are excited at least once. This is indicated by the second y-axis in Figure 6.4, which denotes the probability $P(N \geq 1)$ that an NPL is excited at least once.

At this point, we can use the fact that the optical excitation of the NPL ensemble is governed by Poisson statistics.[33] The complete mathematical description and additional Figures describing the

model can be found in Subsection 2.2.4. The formula, however, which arises from the model and can be employed to describe the saturation behavior is the following:

$$n(t = t_1, \langle N \rangle) = 1 - P(\langle N \rangle, 0) = 1 - e^{C_{ex} I_{ex}} \tag{6.1}$$

In a nutshell, the saturation of the signal at a time t_1 after EEA is practically over is described by unity minus the probability $P(\langle N \rangle, 0)$ that a NPL was not excited at all at $t = 0$. This expression describes the process on the right y-axis in Figure 6.4 as it ranges from zero to one. Comparing Equation 6.1 to Equation 2.22 in Subsection 2.2.4, it is revealed that $\langle N \rangle = C_{ex} I_{ex}$. Thus, upon fitting the data with Equation 6.1 (blue line in Figure 6.4), the extracted proportionality constant C_{ex} establishes the connection between the excitation density I_{ex} and the average number of photo-generated excitons per NPL $\langle N \rangle$. This quantity is then added as the upper x-axis in Figure 6.4.

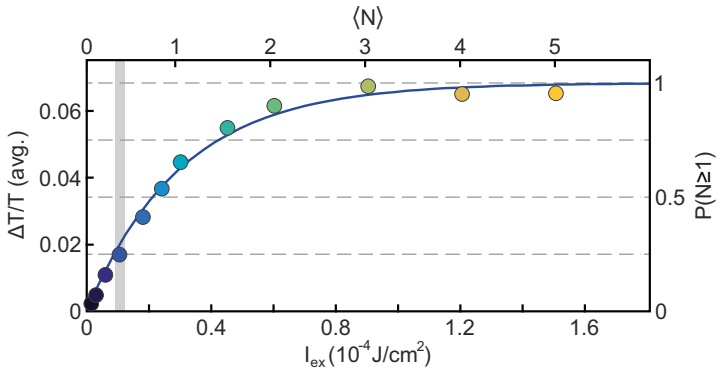

Figure 6.4: Determination of ⟨N⟩. The data points represent the exciton decay signal averaged from 1 ns to 3 ns of the respective curve (same color) in Figure 6.2. Employing Equation 6.1 the data is fit (blue curve) to determine the proportionality constant C_{ex} between I_{ex} and $\langle N \rangle$. Subsequently, the upper x-axis, which connects the two quantities is added. The grey bar marks the interval $0.3 \leq \langle N \rangle \leq 0.4$, which is of importance later in the chapter.

Furthermore, the correlation between the excitation density and the number of excitons generated on average per NPL allows for the calculation of the absorption cross section σ at the excitation wavelength of 400 nm. Since σ is defined as the number of photons absorbed on average by a NPL for a given number of incident photons per area, it can be expressed in terms of the proportionality constant obtained by the fit in Figure 6.4 as follows:

$$\sigma = \frac{E_{photon}}{I_{ex}} \langle N \rangle = E_{photon} C_{ex} \tag{6.2}$$

Here, the assumption is made that the number of absorbed photons equals the number of generated excitons. For the excitation wavelength and intensities present, multiple exciton generation and multiphoton absorption should be negligible and the assumption justified.

The measurement and analysis procedure described so far in this section is conducted with each NPL sample up to a thickness of 6 ML. In other words, exciton decay curves drawn from differential transmission spectra are acquired for each sample for a number of different excitation densities to extract the correlation between I_{ex} and $\langle N \rangle$ as well as σ for each NPL thickness. Instead of shifting the excitation wavelength with the decreasing band gap in thicker NPLs, it is kept at 400 nm, since this is the second harmonic of the TAS laser and a temporally stable excitation is provided. While the energetic surplus of the free electron-hole pairs directly upon excitation in respect to the 1s exciton

state is, thus, larger in thicker NPLs, the excitonic bleaching peak still reaches its maximum within the first picosecond due to the fast carrier relaxation mentioned before.[70]

The extracted σ describing the absorption cross section of a single NPL at 400 nm is depicted for all NPL thicknesses in Figure 6.5. While σ increases rather linearly from 3 ML upwards, it is the highest in the 2 ML NPLs.

Due to its shape anisotropy, a NPL might interact differently with incident light depending on its orientation in respect to the direction and polarization of the light. Since the measurements are conducted on a large ensemble of randomly oriented NPLs in dispersion, however, the extracted absorption cross sections should be an average of all possible orientations. Importantly, all of the values are on the same order of magnitude (10^{-14} cm^2) as the values reported for 4 ML and 5 ML CdSe NPLs of similar lateral dimensions.[106] Furthermore, the trend of a gradual increase from 3 ML upwards could stem from two effects: First, the band gap decrease with increasing thickness causes the 400 nm excitation pulse to excite further above the continuum onset in thicker NPLs, where the density of states is increased. Second, the crystal volume or total number of unit cells simply increases linearly with thickness, which should also increase the absorption cross section of a nanocrystal. Only the 2 ML NPL absorption cross section does not fit this trend. In the last chapter it was already established that excitons in 2 ML NPLs behave differently than in the other samples, possibly due to an inversion of the bright in-plane and out-of-plane exciton states. This effect, however, can not really explain the increased absorption cross section at 400 nm, since this continuum absorption is not an excitonic property, especially in the thicker NPLs. It could of course be the case that the low energy tail of the excitation spectrum centered around 400 nm is in resonance with excitonic states in some NPLs in the 2 ML ensemble, increasing the measured absorption cross section.

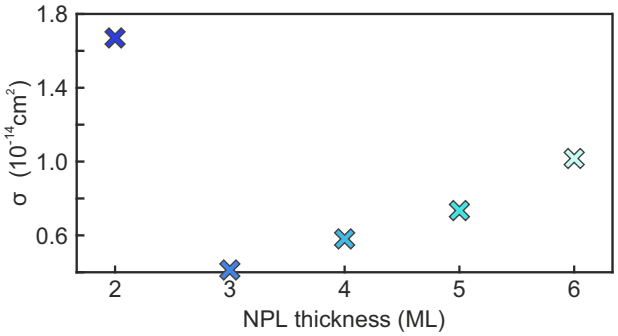

Figure 6.5: Absorption Cross Section. Thickness dependence of the absorption cross section σ at 400 nm in $Cs_{n-1}Pb_nBr_{3n+1}$ NPLs.

Furthermore, the obtained values of σ allow for an estimation of the NPL concentration in the dispersions. To validate our initial assumption that the NPLs in dispersion are independent systems and an interaction is highly unlikely, the NPL concentration c is calculated for all samples according to:

$$c = \frac{\ln(10)\, 10^3 \mathrm{OD}}{\mathrm{N_A} \sigma \mathrm{d}} \tag{6.3}$$

Here, d = 2 mm is the optical path length through the cuvette and OD is the optical density at 400 nm along that path, which is set to 0.2 prior to the measurements by means of dilution in all samples. Furthermore, $\mathrm{N_A}$ is the Avogadro constant. For the 2 ML NPLs for example, a value $c = 1.4 \cdot 10^{14}$ cm^{-3}

corresponding to an average distance between the individual NPLs of 200 nm is obtained. Since σ is the lowest for a 3 ML NPL, the concentration in the 3 ML NPL dispersion has to be the highest, as the OD is constant in all dispersions. Still, the resulting average distance between the individual NPLs amounts to roughly 120 nm in the 3 ML NPL dispersion. This result justifies our assumption that interaction between the NPLs is negligible in these dispersions, especially on the fast time scale of EEA, which is investigated in the following.

6.3 Exciton-Exciton Annihilation Lifetime

After laying the foundation for a comparable analysis of EEA in all samples by determining $\langle N \rangle$, the focus is shifted back to the exciton decay curves. Figure 6.6 depicts the first 20 ps of the decay in 2 ML NPLs for different excitation densities on a logarithmic scale. This representation illustrates the fact that with increasing excitation density EEA becomes even faster. While for lower $\langle N \rangle$ values τ_2 dominates the fast decay caused by EEA, at higher $\langle N \rangle$ values $\tau_{N \geq 3}$, the lifetimes characterizing the duration of existence of three or more excitons in a NPL, also play into the decay. Unfortunately, at higher $\langle N \rangle$ the linear proportionality between the bleaching peak in the DT spectra and the size of the excitonic population is no longer preserved. Thus, a full description of the bimolecular EEA process governed by the rate equation $dn_{ex}/dt = -k_{EEA} n_{ex}^2$ is not possible.

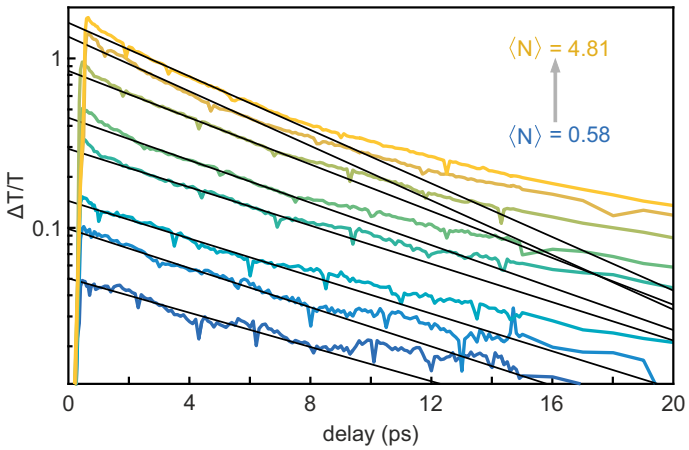

Figure 6.6: Higher-Order Processes. The first 20 ps of the exciton decay curves in 2 ML NPLs are displayed on a logarithmic scale. Processes of a higher order than the decay of an exciton pair characterized by the lifetime τ_2 lead to even faster EEA decay dynamics with increasing $\langle N \rangle$. Whereas the decay is monoexponential, when it is dominated by a single lifetime (τ_2), it converges towards decay dynamics described by the rate equation $dn_{ex}/dt = -k_{EEA} n_{ex}^2$ for high values of $\langle N \rangle$. This effect can, however, not be captured correctly by the TAS measurement technique, as the intensity of the bleaching peak in the DT spectra is not linearly proportional to the size of the exciton population anymore at high $\langle N \rangle$ values.

Instead, to compare the EEA lifetime in the different samples, τ_2, the lifetime of an exciton pair in a NPL shall be extracted for each NPL thickness. To isolate τ_2, the correlation between the excitation density controlled by the laser power and $\langle N \rangle$, the average number of excitons generated per NPL, which was established in the last section, can be employed. The exact probability that a NPL contains N excitons upon excitation, which is governed by Poisson statistics, is plotted in fundamentals Figure 2.14. Calculations yield that in the range $0.3 \leq \langle N \rangle \leq 0.4$ around 4.3 % of the NPLs contain two excitons upon excitation, while only 0.6 % contain more excitons. Accordingly, a decay measurement in this excitation interval, which is marked by the gray bar in Figure 6.4, is chosen to extract the EEA lifetime in each sample and plotted logarithmically in Figure 6.7 normalized to the initial value. For the

presented reasons, this lifetime is then mainly characterized by τ_2. It should further be mentioned that also τ_1, the lifetime characterizing the monomolecular decay of a single exciton in a NPL, plays a negligible role on this time scale, since this process is much slower, i.e., on the order of nanoseconds. Despite some measurement noise affecting the signal at these weaker excitation densities, a clear trend can be observed in the decay curves. While all NPL thicknesses exhibit very fast EEA on the order of tens of picoseconds, the process is even faster in thinner NPLs.

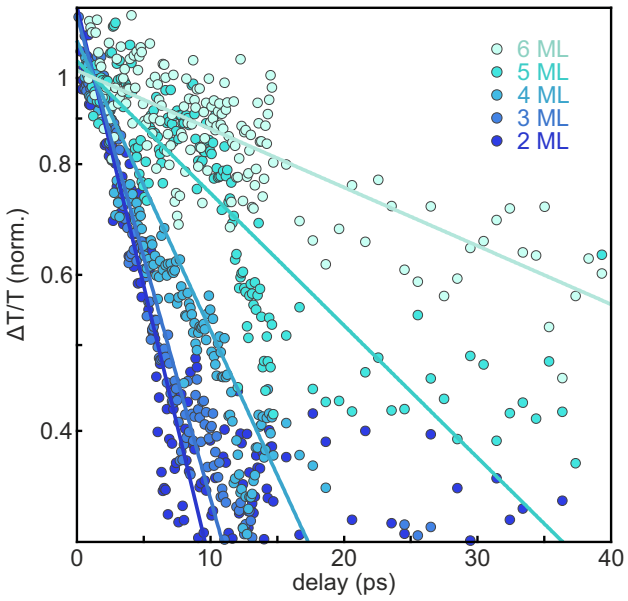

Figure 6.7: Decay of an Exciton Pair. The fast initial exciton decay is shown for each NPL sample for an initial exciton density $0.3 \leq \langle N \rangle \leq 0.4$. Since, the much slower decay of single excitons does not affect the dynamics strongly on this time scale and the generation of three excitons in one NPL is rather unlikely at this $\langle N \rangle$ value, the dynamics mainly represent the fast decay of an exciton pair in a NPL characterized by τ_2.

Furthermore, the exact lifetime at which a monoexponential fit of the temporal evolution of the exciton population drops to $1/e$ of the initial value is plotted in Figure 6.8 for all thicknesses. Interestingly, the thickness dependence of τ_2 is best described by a simple power law $\tau_2 \propto \mathrm{d}^x$ with an exponent of $x = 5.3 \pm 0.2$. Defining $\mathrm{d}_0 = 1\,\mathrm{nm}$, the exact function, which best describes the trend, can be written as:

$$\tau_2(\mathrm{d}) = 6.6\,\mathrm{ps} + 0.064\,\mathrm{ps} \cdot \left(\frac{\mathrm{d}}{\mathrm{d}_0}\right)^{5.3} \tag{6.4}$$

This function is depicted in Figure 6.8 as the grey dashed line and displays good agreement with the τ_2 values extracted for all NPL thicknesses.

An important law, which successfully described the dependence of EEA on nanocrystal size in multiple materials including CdSe and $CsPbBr_3$ in previous studies, is the so-called "universal volume scaling law".[33,107,108] This empirically motivated law suggests a linear dependence between the τ_2 lifetime (in some cases termed τ_{XX}) and the nanocrystal volume and is based on measurements of many cubic or spherical nanocrystal systems. More recent studies have confirmed a general validity of the concept in LHP nanocrystals in combination with notable differences depending on the exact composition.[109,110] Furthermore, for large LHP nanocrystals a sublinear scaling of the EEA lifetime with volume was observed and attributed to differences in the Coulomb interaction in the weak confinement regime.[109] Accordingly, the strength of confinement should play a role in the volume dependence of the EEA

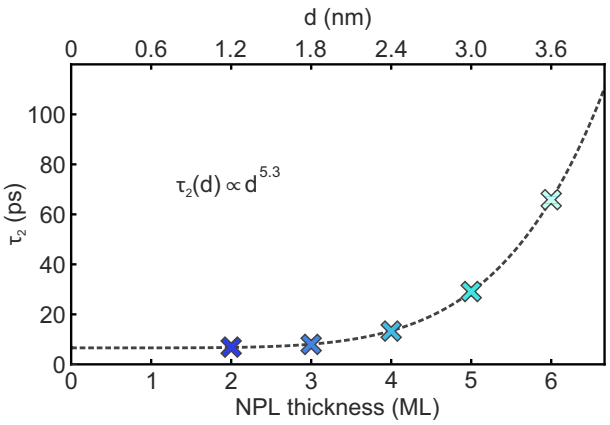

Figure 6.8: Thickness-Dependence of τ_2. The τ_2 lifetimes extracted from the decay curves in Figure 6.7 range from 7 ps to 60 ps and show a power-law dependence on the NPL thickness d with $\tau_2 \propto d^{5.3}$ (grey dashed line).

lifetime. Against this background, an investigation of the effect in strongly confined thickness-tunable NPLs opens up new possibilities. Such a study has, thus far, only been conducted for CdSe NPLs, for which a relationship of $\tau_2 \propto d^7$ was observed and described by a theoretical model.[111] The model suggests that the lateral and thickness dimensions affect the EEA lifetime differently, with the lateral size governing the collision frequency of the two excitons and the thickness mainly affecting the interaction probability during a collision. The difference in exponent between 5.3 in the LHP NPLs and 7 in the CdSe NPLs could be caused by the model used for obtaining the confinement energy of electrons in the CdSe NPLs. This model can not be applied to LHPs directly, since typical III–V and II–VI semiconductor possess an s-like CB and a p-like VB, while for LHPs this is inverted. Thus, to describe the difference, a complex framework, which includes electron-hole correlations, might be necessary.[112]

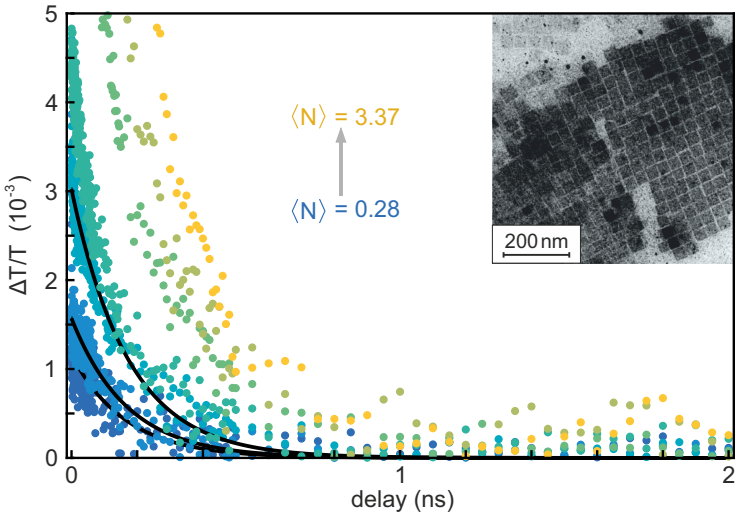

Figure 6.9: Laterally Larger 2 ML Nanoplatelets. Excitonic decay curves extracted from DT spectra of 2 ML NPLs with an edge length of around 35 nm with the monomolecular decay at later times exponentially fitted and subtracted. These first measurements on laterally larger NPLs point towards an EEA lifetime increase with thickness but an improved control over the synthesis is necessary for a detailed study.

Since the lateral size of the NPLs is very similar for all investigated NPL thicknesses, the volume of the NPLs scales almost linearly with thickness. Even if the exact exponent in the power law might be affected by the measurement noise in Figure 6.7, the system clearly does not follow the “universal

volume scaling law". As the $Cs_{n-1}Pb_nBr_{3n+1}$ NPLs consitute the second system besides the CdSe NPLs, which deviates from the "universal volume scaling law", it is very likely that the law only applies to isotropically confined nanocrystals in a certain confinement regime in all material systems. To unravel the full dependence of EEA on nanocrystal shape and size, it is, thus, paramount to control all dimensions of a nanocrystal and investigate the resulting EEA lifetimes. Accordingly, a variation of the lateral size of the NPLs would be highly desirable but remained rather elusive during the course of this thesis. Laterally larger 2 ML NPLs have been synthesized but synthetic difficulties including instability and reproducibility prohibited a detailed study thus far. Figure 6.9 depicts excitonic decay curves obtained from 2 ML NPLs with an edge length of around 35 nm with the monomolecular decay at later times subtracted to isolate the EEA process. The corresponding τ_2 lifetime is clearly longer than the 7 ps measured for the 2 ML NPLs with an edge length of 14 nm. A detailed analysis, however, is yet prohibited, due to stability issues during measurement. In a previous study on 5 ML LHP NPLs, however, a linear dependence of the EEA lifetime on the NPL area was observed.[113]

6.4 Summary and Discussion

This study investigates the thickness dependence of EEA in $Cs_{n-1}Pb_nBr_{3n+1}$ NPLs. As a first step, Poisson statistics are applied to establish a relationship between the excitation density I_{ex} and the on average generated excitons per NPL $\langle N \rangle$. In addition, the obtained proportionality constant connecting those quantities can further be utilized for calculating the average absorption cross section of a single NPL in all samples. Subsequently, the lifetime of two excitons in one NPL, τ_2, representing EEA in general, is determined for all thicknesses up to 6 ML. Interestingly, the thickness dependence of τ_2 can be described by a power law with an exponent of 5.3, a clear deviation from the linear dependence on volume predicted by the "universal volume scaling law".

The results illustrate the need for an investigation of EEA in a nanocrystal system with a precise individual size control in all nanocrystal dimensions. The NPL morphology is of special interest in such a study, as the thickness predominantly affects quantum confinement and, thus, quantities like the exciton binding energy, while the lateral size mainly affects the collision frequency of the two excitons.

A full description of EEA in nanocrystals is of importance in the search for suppression techniques vital for realizing high excitation density applications in these systems. In particular, stimulated emission and ultimately lasing are otherwise difficult to realize.

7

Energy Transfer

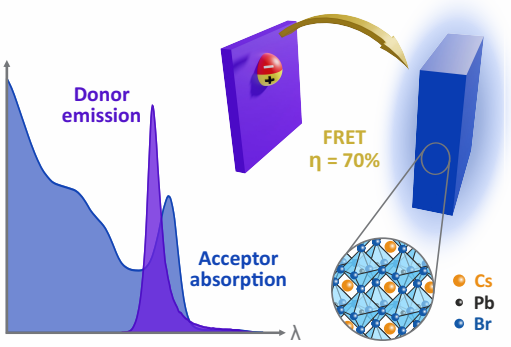

This chapter investigates the Förster resonance energy transfer (FRET) process of excitons between 2 ML and 3 ML $Cs_{n-1}Pb_nBr_{3n+1}$ NPLs. Forming stable heterostructures of LHPs with different band gaps, a prerequisite for FRET, is often prohibited by halide ion migration. Thus, tuning the band gap through NPL thickness instead of halide ion exchange is an interesting alternative for realizing such structures. Furthermore, stacking of the NPLs, an inherent property in thin films of this crystal shape, can even enhance the dipole-dipole interaction between adjacent crystals. As a result, the determined FRET rate reaches up to 0.99 ns^{-1} for high acceptor concentrations, which results in a FRET efficiency of nearly 70 %. Ultimately, NPLs with a number of different thicknesses could be utilized in energy cascade nanostructures for directed energy transfer. The results and all figures presented in this chapter have been published in ACS Energy Letters in 2020 [93].

7.1 Mixing of Dispersions

Most applications utilizing nanocrystals have to contain them in dense layers and do not only rely on the properties of the individual nanocrystals but also on their interplay. It is, thus, of interest, how an exciton behaves in such a layer. In particular, excitonic transfer processes within the inhomogeneous energy landscape, caused by inhomogeneities in the size distribution of the nanocrystals, are of interest. In many nanocrystal systems these processes can be assigned to FRET and cause the diffusion of excitons within the nanocrystal layer.

In fundamentals Section 2.3 the importance of the spectral overlap between the PL of the FRET donor and the absorption of the FRET acceptor was already introduced. Therefore, to study FRET between two specific predefined species, NPLs with different band gaps are employed as donor and acceptor instead of just an inhomogeneously broadened ensemble. More specifically, we turn to 2 ML and 3 ML NPLs, since the strong quantum confinement causes a large enough shift of the PL emission between those thicknesses. Furthermore, these very thin NPLs tend to be more homogeneous than the thicker ones. While the PL and absorption spectra of all NPLs have already been depicted and discussed in this thesis, both quantities are presented again but, here, on the same wavelength-axis in Figure 7.1. This illustrates the strong spectral overlap between the emission of the 2 ML NPLs and the absorption of the 3 ML NPLs. The opposite overlap between the emission of the 3 ML NPLs and the absorption of the 2 ML NPLs, on the other hand, is negligible rendering the 2 ML NPLs the clear FRET donor in this combination. Accordingly, from hereon the terms donor or acceptor refer to 2 ML and 3 ML NPLs, respectively.

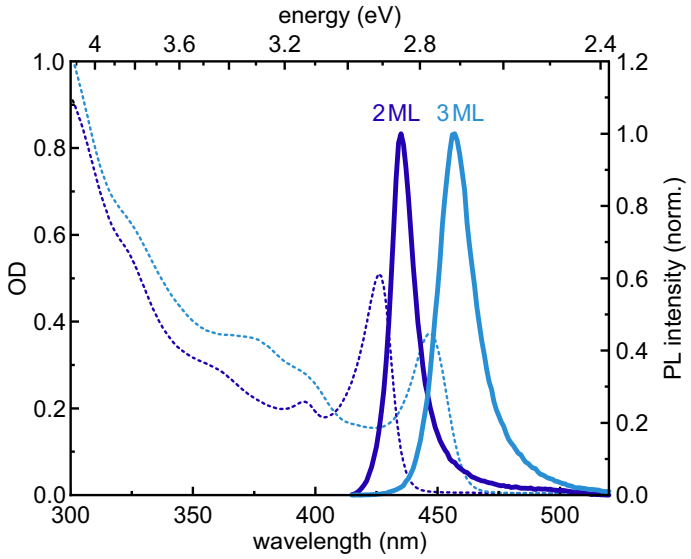

Figure 7.1: Photoluminescence and Absorption Spectra. 2 ML and 3 ML NPL PL (solid lines) and absorption spectra (dashed lines) confirm a sufficient spectral overlap of the 2 ML NPL emission and the 3 ML NPL absorption.

To be able to produce mixtures with fixed molar ratios between the two NPL species, the NPL concentration in the two samples has to be determined first. To that end, the absorption cross section at 400 nm deduced in the last chapter for all thicknesses is employed (see Figure 6.5). In order to calculate the NPL concentration, the OD at 400 nm of the dispersion has to be measured and inserted into Equation 6.3 in combination with the optical path length of the cuvette. This procedure results

in concentrations of $c_{2\,\mathrm{ML}} = 1.2 \cdot 10^{14}\,\mathrm{cm}^{-3}$ and $c_{3\,\mathrm{ML}} = 2.47 \cdot 10^{14}\,\mathrm{cm}^{-3}$ for the 2 ML and 3 ML NPLs, respectively.

In respect to the concentrations, mixtures of the two NPL species are prepared. They are labeled according to the mixing ratio of acceptor and donor, A:D, so that A:D = 1 corresponds to a mixture with the same amount of NPLs of both species in a fixed volume. An absorption spectrum of each mixture is acquired and plotted in Figure 7.2 (colored curves). In addition, the absorption curves of the pure dispersions (top and bottom curve) are summed up with a weighting according to the respective A:D ratio and plotted (black curves). Since the absorptive properties of the mixtures should represent a simple superposition of the individual absorption spectra, this is a convenient way to check if the mixing works. Any changes in the PL can then indeed be attributed to transfer processes instead of structural changes in the NPLs caused by further growth of the individual nanoplatelets for example.

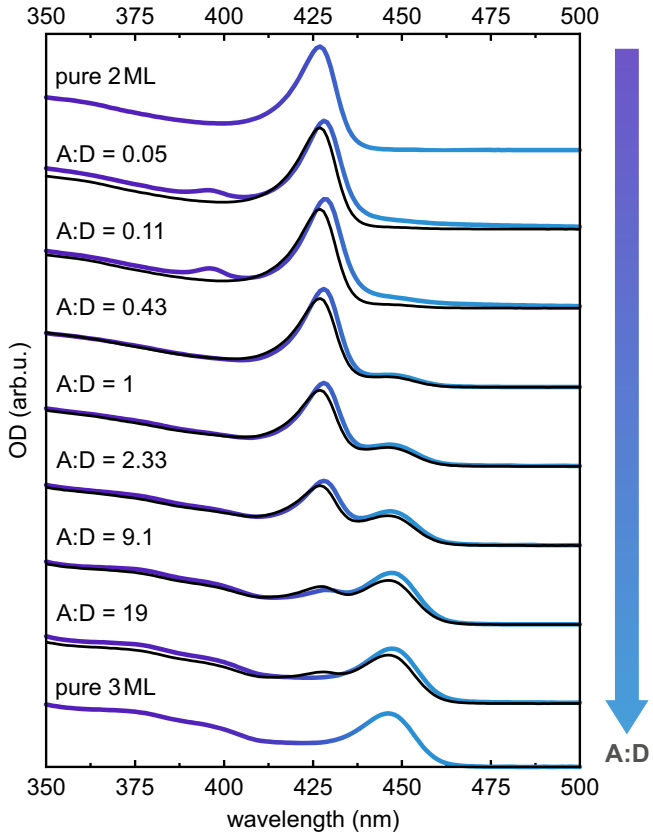

Figure 7.2: Absorption Spectra of Mixed Dispersions. The two NPL species are mixed and absorption spectra are acquired (colored curves). Furthermore, absorption spectra are calculated through a weighted addition of the pure dispersion spectra according to the mixing ratio (black curves) and display good agreement to the measured ones.

In addition to the absorption spectra, PL spectra of the dispersions are also acquired and plotted in Figure 7.3 (colored curves). Again, the simple superposition of the PL spectra of the pure dispersions is calculated according to the respective mixing ratio and added to the figure (black curves). By fitting the 2 ML PL peak of the calculated spectrum to the one of the respective measured spectrum, a clear deviation in the 3 ML emission intensity arises. Either the emission of the 2 ML NPLs is weaker or the emission of the 3 ML NPLs is stronger (or both) than it would be expected from the mixing ratio.

Since the correct mixing was verified by the absorption spectra, the deviation in the PL spectra has to be attributed to a process occurring after absorption of the incident photons. As the PL ratio is shifted towards the emission of the 3 ML NPLs, a transfer process seems to be taking place. Due to the large

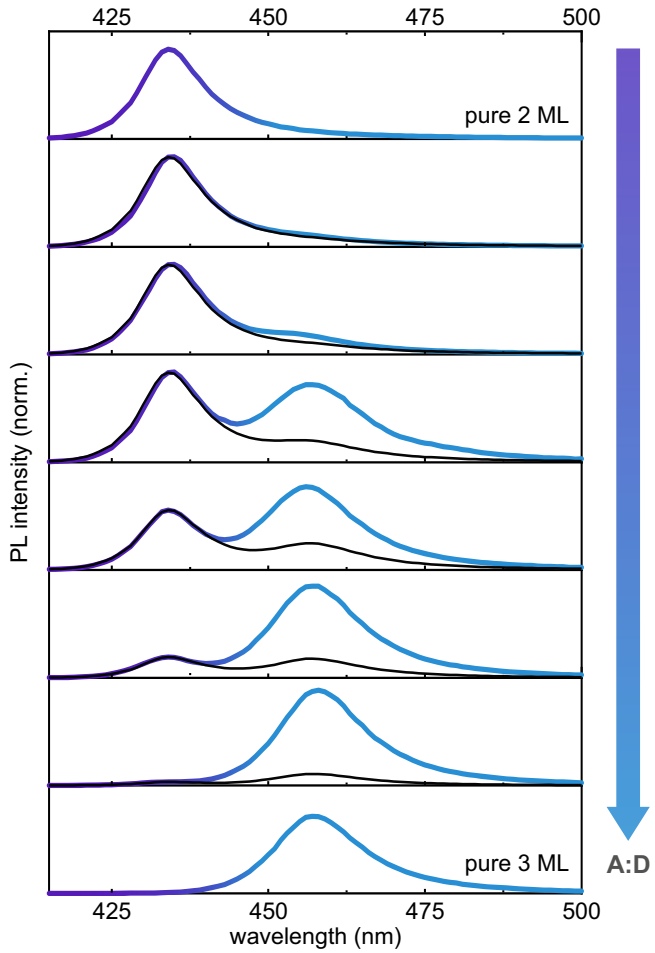

Figure 7.3: Photoluminescence Spectra of Mixed Dispersions. The PL spectrum of all mixtures is plotted normalized in respect to the maximum of the emitted PL (colored curves). Furthermore, a simple superposition of the PL of the pure dispersions according to the mixing ratio is calculated and fitted to the 2 ML NPL PL peak (black curves).

average distance between the NPLs in such a dispersion (in the last section 200 nm were determined for the 2 ML NPLs), FRET is rather unlikely to play a role. Instead the transfer should be of radiative nature in such a dispersion with the 3 ML NPLs reabsorbing photons emitted by the 2 ML NPLs. To check this hypothesis, TR-PL curves of both species are acquired. To that end, spectral filters have to be installed in the beam path of the TCSPC setup introduced in Subsection 3.2.3, which isolate the PL signal stemming from either the 2 ML or 3 ML NPLs (see Figure 7.4).

The isolated PL of the acceptor and donor species is then temporally resolved and plotted for a number of different mixing ratios in Figure 7.5 a and Figure 7.5 b, respectively. While the donor lifetime is nearly constant with mixing ratio, the acceptor lifetime increases slightly for increasing donor concentrations. This is a clear sign of the already proposed reabsorption process, since a feeding of the 3 ML NPLs with additional excitations originating from 2 ML NPL PL leads to an increase in lifetime. If the transfer process were of non-radiative nature, however, the donor lifetime would be decreased by the process in addition to the increase in acceptor lifetime.

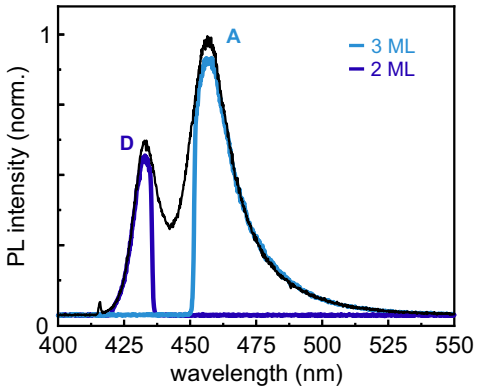

Figure 7.4: Spectral Filters. By installing optical filters, the respective PL signal of the 2 ML (purple curve) or 3 ML (blue curve) NPLs can be isolated quite well with negligible contribution of the other species.

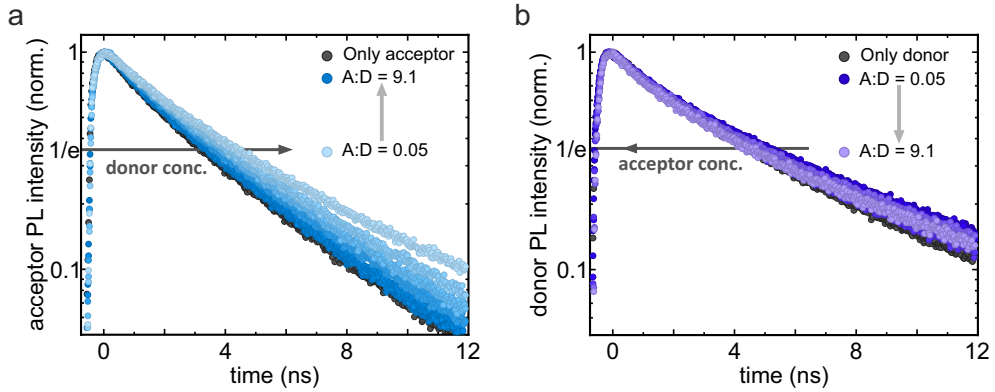

Figure 7.5: Time-Resolved Photoluminescence of Mixed Dispersions. TR-PL curves of the **a)** acceptor NPLs as well as the **b)** donor NPLs for different mixing ratios. Whereas the acceptor lifetime slightly increases for higher donor concentrations, the donor lifetime is rather unaffected by the mixing ratio.

7.2 Donor-Acceptor Heterolayers

In the last section it was shown that the mixtures of 2 ML and 3 ML NPLs are stable but no FRET occurs in the mixed dispersions due to the large distances between the NPLs. As a next step, thin films comprising donor and acceptor NPLs are prepared. While it was demonstrated that the two NPL species are stable in mixture long enough to acquire clean absorption and emission spectra, the mixtures are still a highly dynamical system. Therefore, to prevent any transformations of the NPLs, fresh mixtures were prepared and immediately drop-cast onto silicon substrates, as the NPLs are significantly more stable against transformations in a dried film. Again, PL spectra are acquired for a number of different mixing ratios and displayed in Figure 7.6.

The steady-state PL spectra of the mixed thin films display a trend similar to the PL spectra of the mixed dispersions. Compared to the mixing ratio the PL emission is shifted towards an increased emission of the 3 ML NPLs. Especially for high 2 ML NPL concentrations this effect is very pronounced. As for the dispersions, this points towards an energy transfer process from the 2 ML to the 3 ML NPLs, the nature of which has to be determined by TR-PL spectroscopy. Analogous to the investigation of the dispersions, TR-PL traces are acquired individually from both NPL species by spectrally filtering the signal, which reaches the SPAD. The resulting TR-PL curves of the acceptor and donor NPL species are depicted in Figure 7.7 a and Figure 7.7 b, respectively.

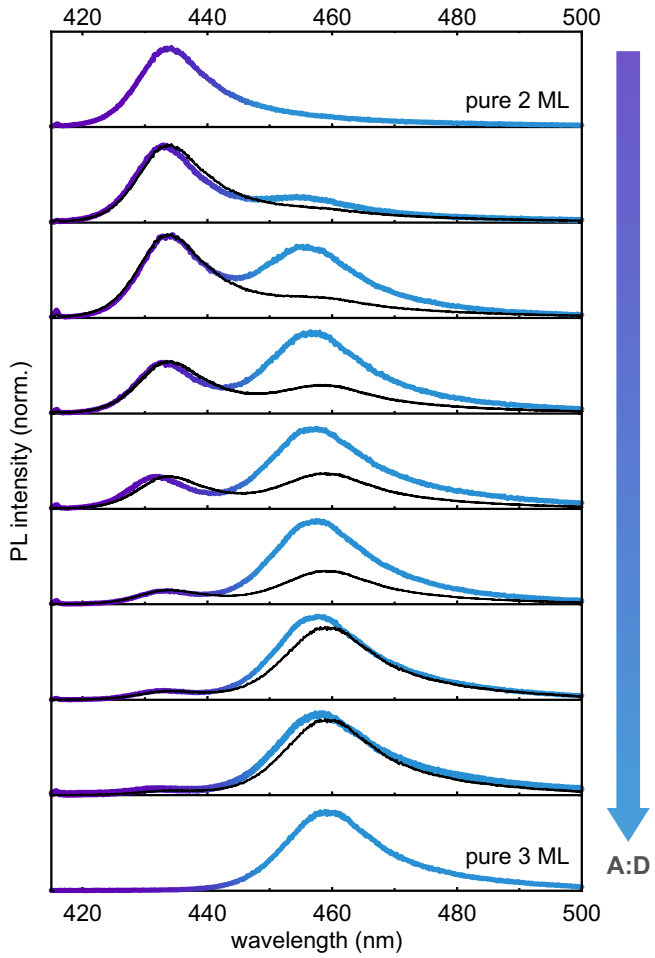

Figure 7.6: Photoluminescence Spectra of Heterolayers. Thin films comprised of 2 ML and 3 ML NPLs are prepared by drop-casting mixed dispersions onto silicon substrates. The PL spectrum of each film is acquired and plotted normalized to the maximum of the emitted PL (colored curves). A behavior analogous to the PL of the dispersions is observed, as the ratio between the PL of the two species is shifted towards the 3 ML NPLs in respect to the mixing ratio (black curves). The effect increases with higher donor concentrations.

The resulting TR-PL curves are of a multi-exponential nature, probably due to differences in the dielectric surrounding or slight inhomogeneities in the donor and acceptor NPL ensembles. Still, instead of a scientifically not fully motivated multi-exponential fit, the time at which the PL signal drops to 1/e of its initial value is simply extracted and serves as the respective lifetime for each decay in the following. For the pure acceptor and the pure donor films, lifetimes of $\tau_A = 1.45$ ns and $\tau_D = 2.26$ ns are determined. Typically, smaller nanocrystals possess shorter PL lifetimes.[71] The here inverted donor and acceptor lifetimes, however, can be be explained by the exciton fine structure, as discussed in Chapter 4.

In the mixed films, the acceptor lifetime increases up to $\tau_A = 5.36$ ns, as progressively more donor is added. The same trend has been observed in the dispersions and is a clear sign for an energy transfer process from the 2 ML to the 3 ML NPLs, since the feeding of the acceptors slows their overall decay. A delayed onset of the acceptor emission is, however, not observed, likely because both species are excited initially. Analogous to the dispersions, the change in the acceptor lifetime does not define the nature of the transfer process. To determine whether it is of radiative or non-radiative nature, the donor lifetime has to be taken into account.

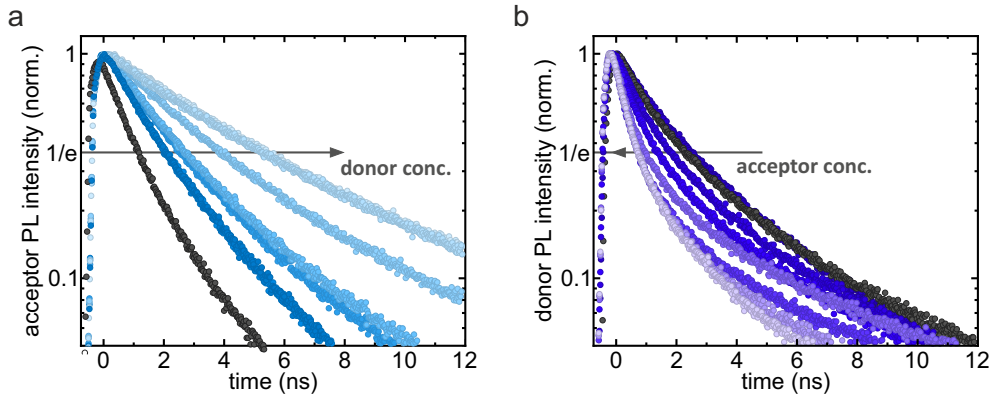

Figure 7.7: Time-Resolved Photoluminescence of Heterolayers. TR-PL curves of both species in the mixed thin films are acquired individually by spectral filtering. The **a)** 3 ML/acceptor PL and the **b)** 2 ML/donor PL are, as for the dispersions, plotted for different mixing ratios. The acceptor lifetime increases with higher donor concentrations, while the donor lifetime decreases with higher acceptor concentrations.

In contrast to the dispersion measurements, the donor lifetime is affected by the acceptor concentration in the thin film. With increasing acceptor concentration, it decreases down to $\tau_D = 0.7$ ns. Thus, an additional pathway must be present, as a simple reabsorption of donor photons would not change the donor lifetime. As previously observed for CdSe NPL films, this non-radiative pathway is very likely due to FRET.[114,115] Simple charge transfer of single electrons or holes is rather unlikely, since the exciton binding energies are above 200 meV in both samples (see fundamentals Figure 2.20) and the distance between neighboring NPLs above 2 nm, as shown by the TEM images in methods Figure 3.1. Furthermore, the efficient and bright PL of the acceptor suggests that the electron-hole pairs transfer to the same NPL, as occurs during a FRET transfer processes of an exciton.

In fundamentals Section 2.3 on energy transfer, the interplay between the decay rate of the pure donor k_D and the FRET rate k_{FRET}, which becomes progressively faster with increasing acceptor concentration, as more and more acceptor NPLs surround every donor NPL, was introduced. Both quantities, k_{FRET} and η_{FRET}, can also be expressed very conveniently in terms of the pure donor lifetime τ_D and the donor lifetime in mixture τ_{DA}:

$$k_{FRET} = \frac{1}{\tau_{DA}} - \frac{1}{\tau_D} \qquad \eta_{FRET} = 1 - \frac{\tau_{DA}}{\tau_D} \tag{7.1}$$

The FRET rate k_{FRET} and the FRET efficiency η_{FRET} are calculated according to Equation 7.1 and depicted in Figure 7.8 for each A:D mixing ratio. The lifetimes τ_D and τ_{DA} are extracted from the curves in Figure 7.7 b. The dependence of the k_{FRET} and η_{FRET} on the A:D ratio displays the expected trend highlighted by the dashed blue curved. With an increasing A:D ratio, the average amount of acceptor NPLs in the vicinity of a donor NPL increases, which in turn increases the rate and efficiency of exciton tranfer away from the donor NPLs. From a certain A:D ratio upwards, however, nearly all donor NPLs are already completely surrounded by acceptor NPLs and the two values saturate, as expected. More specifically, an A:D ratio of 0.11 results in $k_{FRET} = 0.12\,ns^{-1}$ and $\eta_{FRET} = 22\,\%$, and an A:D ratio of 20 boosts these values up to $k_{FRET} = 0.99\,ns^{-1}$ and $\eta_{FRET} = 69\,\%$. While the efficiency is already quite high, it might be further improved by controlling the ordering in the film in terms of a controlled stacking of the NPLs, instead of a simple drop-cast with no control over the arrangement of the NPLs. Additionally, a decreased length of the passivating ligands, which would result in a shorter spacing between the NPLs in a stack, could further facilitate the process. Nonetheless, FRET proves

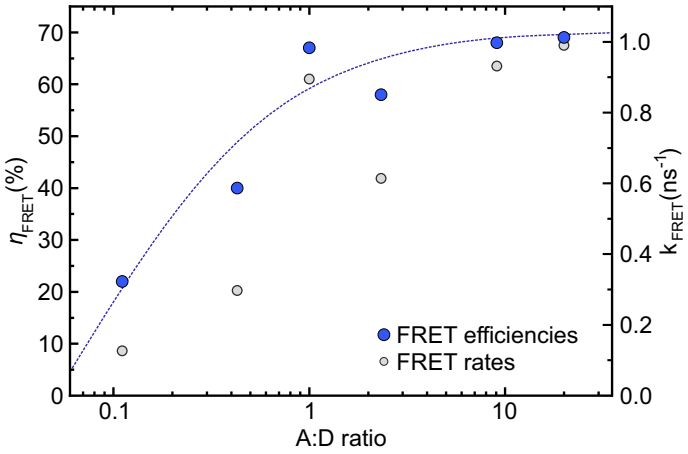

Figure 7.8: Förster Resonance Energy Transfer Rate and Efficiency. The FRET rate k_{FRET} (gray circles) as well as the FRET efficiency η_{FRET} (blue circles) are extracted from the TR-PL curves in Figure 7.7 b according to Equation 7.1 for each A:D mixing ratio. The dashed blue line is added as a guide to the eye to illustrate the expected saturation behavior of both values once all donor NPLs are completely surrounded with acceptor NPLs at high acceptor concentrations.

to be an alternative process to optical excitation for an efficient generation of excitons in LHP NPL films. Furthermore, this is the first such demonstration of FRET between two defined LHP nanocrystal species.

7.3 Summary and Discussion

This study tackled the issue of non-radiative excitation of LHP nanocrystals via energy transfer, which has not been investigated yet between two defined species. The reason for this lies in the need for the formation of a heterolayer containing two different nanocrystal species with different band gap energies, one acting as the donor and one as the acceptor. An important tuning mechanism of the band gap of LHP nanocrystals is the exchange of the halide ions between iodide, bromide, or chloride. Such a heterostructure, however, suffers from halide ion exchange and especially the mixing of the dispersions would result in every nanocrystal containing both halide species.[73,116] The second mechanism to tune the band gap lies in quantum confinement, or, in other words, the size of the nanocrystals. In that regard, NPLs are an optimal candidate, as the very strong thickness-confinement of 2 ML and 3 ML NPLs causes a large enough shift of the band gap, while the similarity in lateral size still allows for a highly ordered film.

In this study, the spectral overlap of the 2 ML NPL emission and the 3 ML NPL absorption is confirmed via absorption and PL spectroscopy of both species. Then, mixed dispersions with different ratios are prepared and their absorption and PL spectra are acquired. While the superposition of the absorption spectra of the pure species resemble the mixing ratio, the weight is shifted towards the 3 ML NPLs in the PL emission spectra. To identify which type of transfer causes this shift, TR-PL measurements are conducted. An increased acceptor lifetime in combination with an unaffected donor lifetime reveal the radiative nature of the transfer.

Next, films are drop-casted from the mixed dispersions and their PL spectra acquired. Again, an increased 3 ML NPL emission relative to the mixing ratio points towards a transfer process. In the films, however, the increase in acceptor lifetime is accompanied by a decrease in donor lifetime. This

decrease stems from an additional channel for excitons to transfer out of the 2 ML NPLs, namely FRET. By analyzing the donor lifetimes, the FRET rates and efficiencies are determined for each mixture and reach values of $k_{\mathrm{FRET}} = 0.99\,\mathrm{ns}^{-1}$ and $\eta_{\mathrm{FRET}} = 69\,\%$ for an A:D ratio of 20.

Since this type of system is hard to realize through halide ion exchange, size-controllable LHP nanocrystals and, in particular, NPLs are a promising candidate to achieve a directed flow of excitons in a cascaded energy-transfer structure. Also, positioning the NPLs on top of a wider band gap material containing long-lived excitons could result in an efficient non-radiative injection of excitons into the NPLs.

8

Conclusion and Outlook

As a detailed summary of each project can be found at the end of each chapter, this part is kept rather concise and the focus lies on giving an outlook on future research in the field.

Chapter 4 revealed that the lowest state of the excitonic fine structure of the $Cs_{n-1}Pb_nBr_{3n+1}$ NPLs is a dark or optically inactive state, which is split 32.3 meV from the lowest bright state in the thinnest NPLs. By theoretically describing the thickness dependence of this splitting, a general understanding of how the NPL thickness affects the exciton fine structure splitting is gained, which could help to predict the behavior of other anisotropically confined systems. Chapter 5 quantified the exciton-phonon coupling responsible for the thermal broadening of the spectral linewidth. Here, the 2 ML NPLs demonstrated a unique behavior compared to the other NPLs with an increased LO phonon energy and a stronger coupling of excitons to this phonon mode. This result might be connected to an inversion of the bright in-plane and out-of-plane polarized exciton levels predicted by the model in Chapter 4, which would shift the mean occupation of those levels at finite temperatures. Third, the thickness dependence of exciton-exciton-annihilation was determined to obey a power law according to $\tau_2 \propto d^{5.3}$ (d being the NPL thickness) in Chapter 6. This dependence represented a clear deviation from the "universal volume scaling law" and underpinned the need for investigating such properties not only in cubic or spherical nanocrystals but also in anisotropically shaped size-tunable nanocrystals. Last, in Chapter 7, energy transfer in the form of FRET-mediated exciton transfer, with an efficiency up to 69 % was observed from 2 ML to 3 ML NPLs. Such alternative non-optical excitation pathways, which circumvent the lack of conductivity of some of the nanocrystal layers, could help in realizing lighting applications.

In the introduction of this thesis, it was stated that this work not only aims to answer some questions connected to the material under investigation, $Cs_{n-1}Pb_nBr_{3n+1}$ NPLs, but also to provide a contribution to the large field of confined semiconductors in general. Notably, the novel effective mass model developed to describe the exciton fine structure in this system can easily be applied to other anisotropically confined systems. This can, on the one hand, help in identifying sought-after materials in which the lowest excitonic level is bright. On the other hand, systems with a large splitting induced by

quantum confinement between a lowest dark level and the first bright level might be identified. Such a material is often characterized by very long-lived excitons, especially at low temperature, a relevant property for some semiconductor applications not related to lighting.[117] Importantly, the bright-dark splitting of 32.3 meV determined for the 2 ML NPLs is even the largest such splitting reported to date in any semiconductor nanocrystal system. A conundrum, namely, that the 2 ML NPLs often exhibit a slower PL decay at room temperature than the 3 ML NPLs, which contrasts many previous findings for nanocrystals in general, is also lifted by this large splitting, since excitons spend a significant amount of time in the dark state even at room temperature. As mentioned in the first paragraph, also the results on exciton-phonon interaction suggest that the fine structure affects the PL emission up to room temperature. Hopefully, all of these findings combined can contribute in navigating through the sheer endless parameter-space of possible nanocrystal shapes and compositions towards an optimum for specific applications.

Lastly, the $Cs_{n-1}Pb_nBr_{3n+1}$ NPLs shall be addressed in terms of their own unique potential. With a flexible and cheap room temperature synthesis resulting in blue emitters displaying high PLQYs, many requirements of optical applications are already fulfilled. Additionally, the results of Chapter 5 revealed that the thermal contribution to the PL linewidth of 2 ML NPLs is exceptionally low. Thus, further improvements of their already good homogeneity could result in one of the narrowest (at room temperature) blue emitters available, an important prerequisit for pure color in lighting and display applications. Naturally, the obstacles of low stability and conductivity, which impede commercialization, are predominantly of chemical nature and could both be connected to the ligands attached to the NPLs as well as the residual ligands present in a thin film comprised of the NPLs. More tightly bound and maybe even shorter ligands could improve stability, while also allowing for eliminating free ligands from the solution and, in turn, increase the homogeneity and the conductivity of thin films through smaller distances between the individual crystals. In the context of efficient and, thus, energy-saving devices, which includes efficient manufacturing processes, material research into these colloidal NPLs should be continued.

References

[1] R. Rossetti, S. Nakahara, and Louis E. Brus. "Quantum size effects in the redox potentials, resonance Raman spectra, and electronic spectra of CdS crystallites in aqueous solution." In: *The Journal of Chemical Physics* 79.2 (1983), pp. 1086–1088. DOI: 10.1063/1.445834 (cited on page 1).

[2] Louis E. Brus. "Electron–electron and electron-hole interactions in small semiconductor crystallites: The size dependence of the lowest excited electronic state." In: *The Journal of Chemical Physics* 80.9 (1984), pp. 4403–4409. DOI: 10.1063/1.447218 (cited on page 1).

[3] Alexander L. Efros and Alexei L. Efros. "Interband absorption of light in a semiconductor sphere." In: *Soviet Physics Semiconductors* 16.7 (1982), pp. 772–775 (cited on pages 1, 2).

[4] Katherine Bourzac. "Quantum dots go on display." In: *Nature* 493.7432 (2013), p. 283. DOI: 10.1038/493283a (cited on page 1).

[5] Akihiro Kojima, Kenjiro Teshima, Yasuo Shirai, and Tsutomu Miyasaka. "Organometal halide perovskites as visible-light sensitizers for photovoltaic cells." In: *Journal of the American Chemical Society* 131.17 (2009), pp. 6050–6051. DOI: 10.1021/ja809598r (cited on page 1).

[6] Constantinos C. Stoumpos and Mercouri G. Kanatzidis. "The renaissance of halide perovskites and their evolution as emerging semiconductors." In: *Accounts of Chemical Research* 48.10 (2015), pp. 2791–2802. DOI: 10.1021/acs.accounts.5b00229 (cited on page 1).

[7] Loredana Protesescu, Sergii Yakunin, Maryna I. Bodnarchuk, Franziska Krieg, Riccarda Caputo, Christopher H. Hendon, Ruo Xi Yang, Aron Walsh, and Maksym V. Kovalenko. "Nanocrystals of cesium lead halide perovskites ($CsPbX_3$, X= Cl, Br, and I): novel optoelectronic materials showing bright emission with wide color gamut." In: *Nano letters* 15.6 (2015), pp. 3692–3696. DOI: 10.1021/nl5048779 (cited on pages 1, 28, 30, 71).

[8] Jasmina A. Sichert, Yu Tong, Niklas Mutz, Mathias Vollmer, Stefan Fischer, Karolina Z. Milowska, Ramon García Cortadella, Bert Nickel, Carlos Cardenas-Daw, Jacek K. Stolarczyk, Alexander S. Urban, and Jochen Feldmann. "Quantum size effect in organometal halide perovskite nanoplatelets." In: *Nano Letters* 15.10 (2015), pp. 6521–6527. DOI: 10.1021/acs.nanolett.5b02985 (cited on pages 1, 28).

[9] Verena A. Hintermayr, Alexander F. Richter, Florian Ehrat, Markus Döblinger, Willem Vanderlinden, Jasmina A. Sichert, Yu Tong, Lakshminarayana Polavarapu, Jochen Feldmann, and Alexander S. Urban. "Tuning the optical properties of perovskite nanoplatelets through composition and thickness by ligand-assisted exfoliation." In: *Advanced Materials* 28.43 (2016), pp. 9478–9485. DOI: 10.1002/adma.201602897 (cited on pages 1, 30).

[10] Bernhard J. Bohn, Yu Tong, Moritz Gramlich, May Ling Lai, Markus Döblinger, Kun Wang, Robert L. Z. Hoye, Peter Müller-Buschbaum, Samuel D. Stranks, Alexander S. Urban, Lakshminarayana Polavarapu, and Jochen Feldmann. "Boosting tunable blue luminescence of halide perovskite nanoplatelets through postsynthetic surface trap repair." In: *Nano Letters* 18.8 (2018), pp. 5231–5238. DOI: 10.1021/acs.nanolett.8b02190 (cited on pages 1, 11, 28, 30, 31, 34, 38, 66, 72).

[11] Charles Kittel. *Introduction to Solid State Physics*. Vol. 8. Wiley New York, 2004. DOI: 10.1119/1.1974177 (cited on pages 4–7, 21).

[12] Neil W. Ashcroft and N. David Mermin. *Solid State Physics*. Saunders College Publishing, 1976. DOI: 10.1002/piuz.19780090109 (cited on pages 4–6).

[13] Peter Y. Yu and Manuel Cardona. *Fundamentals of Semiconductors: Physics and Materials Properties*. Springer, 2010. DOI: 10.1007/978-3-642-00710-1 (cited on pages 5, 8, 12, 16).

[14] Erwin Schrödinger. "Quantisierung als Eigenwertproblem." In: *Annalen der Physik* 385.13 (1926), pp. 437–490. DOI: 10.1002/andp.19263851302 (cited on page 5).

[15] Felix Bloch. "Über die Quantenmechanik der Elektronen in Kristallgittern." In: *Zeitschrift für Physik* 52.7-8 (1929), pp. 555–600. DOI: 10.1007/BF01339455 (cited on page 5).

[16] Wahyu Setyawan and Stefano Curtarolo. "High-throughput electronic band structure calculations: Challenges and tools." In: *Computational Materials Science* 49.2 (2010), pp. 299–312. DOI: 10.1016/j.commatsci.2010.05.010 (cited on page 5).

[17] Claus F. Klingshirn. *Semiconductor Optics*. Springer Science & Business Media, 2012. DOI: 10.1007/978-3-642-28362-8 (cited on pages 6, 8, 13).

[18] Mark Fox. *Optical Properties of Solids*. Oxford University Press, 2002. DOI: 10.1119/1.1691372 (cited on pages 6, 7, 10, 16).

[19] Enrico Fermi. "Eine statistische Methode zur Bestimmung einiger Eigenschaften des Atoms und ihre Anwendung auf die Theorie des periodischen Systems der Elemente." In: *Zeitschrift für Physik* 48.1-2 (1928), pp. 73–79. DOI: 10.1007/BF01351576 (cited on page 7).

[20] Paul A. M. Dirac. "On the theory of quantum mechanics." In: *Proceedings of the Royal Society of London. Series A, Containing Papers of a Mathematical and Physical Character* 112.762 (1926), pp. 661–677. DOI: 10.1098/rspa.1926.0133 (cited on page 7).

[21] Marius Grundmann. *Physics of Semiconductors*. Springer, 2016. DOI: 10.1007/978-3-319-23880-7 (cited on pages 7, 9, 17, 18).

[22] Jenya Tilchin, Dmitry N. Dirin, Georgy I. Maikov, Aldona Sashchiuk, Maksym V. Kovalenko, and Efrat Lifshitz. "Hydrogen-like wannier–mott excitons in single crystal of methylammonium lead bromide perovskite." In: *ACS Nano* 10.6 (2016), pp. 6363–6371. DOI: 10.1021/acsnano.6b02734 (cited on page 8).

[23] María C. Gélvez-Rueda, Eline M. Hutter, Duyen H. Cao, Nicolas Renaud, Constantinos C. Stoumpos, Joseph T. Hupp, Tom J. Savenije, Mercouri G. Kanatzidis, and Ferdinand C. Grozema. "Interconversion between free charges and bound excitons in 2D hybrid lead halide perovskites." In: *The Journal of Physical Chemistry C* 121.47 (2017), pp. 26566–26574. DOI: 10.1021/acs.jpcc.7b10705 (cited on page 9).

[24] Karl W. Böer and Udo W. Pohl. *Semiconductor Physics*. Springer, 2018. DOI: 10.1007/978-3-319-69150-3 (cited on page 9).

[25] David J. Griffiths and Darrell F. Schroeter. *Introduction to Quantum Mechanics*. Cambridge University Press, 2018. DOI: 10.1017/9781316995433 (cited on page 10).

[26] Kenichiro Tanaka and Takashi Kondo. "Bandgap and exciton binding energies in lead-iodide-based natural quantum-well crystals." In: *Science and Technology of Advanced Materials* 4.6 (2003), pp. 599–604. DOI: 10.1016/j.stam.2003.09.019 (cited on page 11).

[27] Tilmann D. Märk and Gordon H. Dunn. *Electron Impact Ionization*. Springer Science & Business Media, 2013. DOI: 10.1007/978-3-7091-4028-4 (cited on page 13).

[28] Henry Kressel. *Semiconductor Lasers and Heterojunction LEDs*. Elsevier, 2012. DOI: 10.1016/b978-0-12-426250-8.x5001-5 (cited on page 13).

[29] Paul Adrien Maurice Dirac. "The quantum theory of the emission and absorption of radiation." In: *Proceedings of the Royal Society of London. Series A, Containing Papers of a Mathematical and Physical Character* 114.767 (1927), pp. 243–265. DOI: 10.1098/rspa.1927.0039 (cited on page 13).

[30] Aurora Manzi, Yu Tong, Julius Feucht, En-Ping Yao, Lakshminarayana Polavarapu, Alexander S. Urban, and Jochen Feldmann. "Resonantly enhanced multiple exciton generation through below-band-gap multi-photon absorption in perovskite nanocrystals." In: *Nature Communications* 9.1 (2018), pp. 1–6. DOI: 10.1038/s41467-018-03965-8 (cited on page 14).

[31] Jagdeep Shah. *Ultrafast Spectroscopy of Semiconductors and Semiconductor Nanostructures*. Springer Science & Business Media, 2010. DOI: 10.1007/978-3-662-03770-6 (cited on page 15).

[32] Michael A. Becker, Roman Vaxenburg, Georgian Nedelcu, Peter C. Sercel, Andrew Shabaev, Michael J. Mehl, John G. Michopoulos, Samuel G. Lambrakos, Noam Bernstein, John L. Lyons, Thilo Stöferle, Rainer F. Mahrt, Maksym V. Kovalenko, David J. Norris, Gabriele Raino, and Alexander L. Efros. "Bright triplet excitons in caesium lead halide perovskites." In: *Nature* 553.7687 (2018), pp. 189–193. DOI: 10.1038/nature25147 (cited on pages 16, 50, 67).

[33] Victor I. Klimov, Alexander A. Mikhailovsky, D.W. McBranch, Catherine A. Leatherdale, and Moungi G. Bawendi. "Quantization of multiparticle Auger rates in semiconductor quantum dots." In: *Science* 287.5455 (2000), pp. 1011–1013. DOI: 10.1126/science.287.5455.1011 (cited on pages 19, 20, 81, 82, 86).

[34] Werner Heisenberg. "Über den anschaulichen Inhalt der quantentheoretischen Kinematik und Mechanik." In: *Zeitschrift für Physik* 43.3 (1927), pp. 172–198. DOI: 10.1007/BF01397280 (cited on page 21).

[35] S. Rudin, T.L. Reinecke, and B. Segall. "Temperature-dependent exciton linewidths in semiconductors." In: *Physical Review B* 42.17 (1990), pp. 11218–11231. DOI: 10.1103/PhysRevB.42.11218 (cited on page 22).

[36] Woldemar Voigt. "Über das Gesetz der Intensitätsverteilung innerhalb der Linien eines Gasspektrums." In: *Sitzungsberichte der K. B. Akad. d. Wiss.* 1912,25 (1912) (cited on page 22).

[37] Guy Allan and Christophe Delerue. "Energy transfer between semiconductor nanocrystals: Validity of Förster's theory." In: *Physical Review B* 75.19 (2007), p. 195311. DOI: 10.1103/PhysRevB.75.195311 (cited on page 23).

[38] Theodor Förster. "Zwischenmolekulare Energiewanderung und Fluoreszenz." In: *Annalen der Physik* 437.1-2 (1948), pp. 55–75. DOI: 10.1002/andp.19484370105 (cited on page 23).

[39] Cherie R. Kagan, Christopher B. Murray, Manoj Nirmal, and Moungi G. Bawendi. "Electronic energy transfer in CdSe quantum dot solids." In: *Physical Review Letters* 76.9 (1996), p. 1517 (cited on page 23).

[40] Andrey L. Rogach, Thomas A. Klar, John M. Lupton, Andries Meijerink, and Jochen Feldmann. "Energy transfer with semiconductor nanocrystals." In: *Journal of Materials Chemistry* 19.9 (2009), pp. 1208–1221. DOI: 10.1039/B812884G (cited on page 23).

[41] Kenta Furuta, Minoru Fujii, Hiroshi Sugimoto, and Kenji Imakita. "Energy transfer in silicon nanocrystal solids made from all-inorganic colloidal silicon nanocrystals." In: *The Journal of Physical Chemistry Letters* 6.14 (2015), pp. 2761–2766. DOI: 10.1021/acs.jpclett.5b01067 (cited on page 23).

[42] Martin A. Green, Anita Ho-Baillie, and Henry J. Snaith. "The emergence of perovskite solar cells." In: *Nature Photonics* 8.7 (2014), pp. 506–514. DOI: 10.1038/nphoton.2014.134 (cited on page 24).

[43] Victor M. Goldschmidt. "Die Gesetze der Krystallochemie." In: *Naturwissenschaften* 14.21 (1926), pp. 477–485. DOI: 10.1007/BF01507527 (cited on page 24).

[44] Chonghea Li, Xionggang Lu, Weizhong Ding, Liming Feng, Yonghui Gao, and Ziming Guo. "Formability of ABX_3 (X = F, Cl, Br, I) halide perovskites." In: *Acta Crystallographica Section B: Structural Science* 64.6 (2008), pp. 702–707. DOI: 10.1107/S0108768108032734 (cited on page 25).

[45] Shunsuke Hirotsu, Jimpei Harada, Masashi Iizumi, and Kazuo Gesi. "Structural phase transitions in $CsPbBr_3$." In: *Journal of the Physical Society of Japan* 37.5 (1974), pp. 1393–1398. DOI: 10.1143/JPSJ.37.1393 (cited on pages 25, 48).

[46] William Shockley and Hans J. Queisser. "Detailed balance limit of efficiency of p-n junction solar cells." In: *Journal of Applied Physics* 32.3 (1961), pp. 510–519. DOI: 10.1063/1.1736034 (cited on page 25).

[47] Jacky Even, Laurent Pedesseau, and Claudine Katan. "Analysis of multivalley and multibandgap absorption and enhancement of free carriers related to exciton screening in hybrid perovskites." In: *The Journal of Physical Chemistry C* 118.22 (2014), pp. 11566–11572. DOI: 10.1021/jp503337a (cited on page 25).

[48] Jacky Even, Laurent Pedesseau, Claudine Katan, Mikaël Kepenekian, Jean-Sébastien Lauret, Daniel Sapori, and Emmanuelle Deleporte. "Solid-state physics perspective on hybrid perovskite semiconductors." In: *The Journal of Physical Chemistry C* 119.19 (2015), pp. 10161–10177. DOI: 10.1021/acs.jpcc.5b00695 (cited on page 25).

[49] Laura M. Herz. "Charge-carrier dynamics in organic-inorganic metal halide perovskites." In: *Annual Review of Physical Chemistry* 67.1 (2016), pp. 65–89. DOI: 10.1146/annurev-physchem-040215-112222 (cited on pages 25, 27).

[50] Jacky Even, Laurent Pedesseau, Jean-Marc Jancu, and Claudine Katan. "Importance of spin–orbit coupling in hybrid organic/inorganic perovskites for photovoltaic applications." In: *The Journal of Physical Chemistry Letters* 4.17 (2013), pp. 2999–3005. DOI: 10.1021/jz401532q (cited on page 26).

[51] Constantinos C. Stoumpos, Christos D. Malliakas, and Mercouri G. Kanatzidis. "Semiconducting tin and lead iodide perovskites with organic cations: phase transitions, high mobilities, and near-infrared photoluminescent properties." In: *Inorganic Chemistry* 52.15 (2013), pp. 9019–9038. DOI: 10.1021/ic401215x (cited on page 26).

[52] J. Bardeen and W. Shockley. "Deformation potentials and mobilities in non-polar crystals." In: *Physical Review* 80.1 (1950), p. 72. DOI: 10.1103/PhysRev.80.72 (cited on page 26).

[53] Jarvist M. Frost, Keith T. Butler, Federico Brivio, Christopher H. Hendon, Mark Van Schilfgaarde, and Aron Walsh. "Atomistic origins of high-performance in hybrid halide perovskite solar cells." In: *Nano Letters* 14.5 (2014), pp. 2584–2590. DOI: 10.1021/nl500390f (cited on page 26).

[54] Michael M. Lee, Joël Teuscher, Tsutomu Miyasaka, Takurou N. Murakami, and Henry J. Snaith. "Efficient hybrid solar cells based on meso-superstructured organometal halide perovskites." In: *Science* 338.6107 (2012), pp. 643–647. DOI: 10.1126/science.1228604 (cited on page 26).

[55] Jun Hong Noh, Sang Hyuk Im, Jin Hyuck Heo, Tarak N. Mandal, and Sang Il Seok. "Chemical management for colorful, efficient, and stable inorganic–organic hybrid nanostructured solar cells." In: *Nano Letters* 13.4 (2013), pp. 1764–1769. DOI: 10.1021/nl400349b (cited on page 26).

[56] Junfeng Yan and Brian R. Saunders. "Third-generation solar cells: a review and comparison of polymer: fullerene, hybrid polymer and perovskite solar cells." In: *RSC Advances* 4.82 (2014), pp. 43286–43314. DOI: 10.1039/C4RA07064J (cited on page 27).

[57] Samuel D. Stranks, Giles E. Eperon, Giulia Grancini, Christopher Menelaou, Marcelo J.P. Alcocer, Tomas Leijtens, Laura M. Herz, Annamaria Petrozza, and Henry J Snaith. "Electron-hole diffusion lengths exceeding 1 micrometer in an organometal trihalide perovskite absorber." In: *Science* 342.6156 (2013), pp. 341–344. DOI: 10.1126/science.1243982 (cited on page 27).

[58] He Huang, Maryna I. Bodnarchuk, Stephen V. Kershaw, Maksym V. Kovalenko, and Andrey L. Rogach. "Lead halide perovskite nanocrystals in the research spotlight: stability and defect tolerance." In: *ACS Energy Letters* 2.9 (2017), pp. 2071–2083. DOI: 10.1021/acsenergylett.7b00547 (cited on page 27).

[59] Christian Wehrenfennig, Giles E. Eperon, Michael B. Johnston, Henry J. Snaith, and Laura M. Herz. "High charge carrier mobilities and lifetimes in organolead trihalide perovskites." In: *Advanced Materials* 26.10 (2014), pp. 1584–1589. DOI: 10.1002/adma.201305172 (cited on page 27).

[60] Himchan Cho, Young-Hoon Kim, Christoph Wolf, Hyeon-Dong Lee, and Tae-Woo Lee. "Improving the stability of metal halide perovskite materials and light-emitting diodes." In: *Advanced Materials* 30.42 (2018), p. 1704587. DOI: 10.1002/adma.201704587 (cited on page 27).

[61] Luis K. Ono, Yabing Qi, and Shengzhong Frank Liu. "Progress toward stable lead halide perovskite solar cells." In: *Joule* 2.10 (2018), pp. 1961–1990. DOI: 10.1016/j.joule.2018.07.007 (cited on page 27).

[62] Daniel J. Slotcavage, Hemamala I. Karunadasa, and Michael D. McGehee. "Light-induced phase segregation in halide-perovskite absorbers." In: *ACS Energy Letters* 1.6 (2016), pp. 1199–1205. DOI: 10.1021/acsenergylett.6b00495 (cited on page 27).

[63] Yu Tong, Bernhard J. Bohn, Eva Bladt, Kun Wang, Peter Müller-Buschbaum, Sara Bals, Alexander S. Urban, Lakshminarayana Polavarapu, and Jochen Feldmann. "From precursor powders to $CsPbX_3$ perovskite nanowires: One-pot synthesis, growth mechanism, and oriented self-assembly." In: *Angewandte Chemie* 56.44 (2017), pp. 13887–13892. DOI: 10.1002/anie.201707224 (cited on page 28).

[64] S.N. Ruddlesden and P. Popper. "New compounds of the K_2NiF_4 type." In: *Acta Crystallographica* 10.8 (1957), pp. 538–539. DOI: 10.1107/S0365110X57001929 (cited on page 28).

[65] S.N. Ruddlesden and P. Popper. "The compound $Sr_3Ti_2O_7$ and its structure." In: *Acta Crystallographica* 11.1 (1958), pp. 54–55. DOI: 10.1107/S0365110X58000128 (cited on page 28).

[66] Junzhi Ye, Mahdi Malekshahi Byranvand, Clara Otero Martínez, Robert L.Z. Hoye, Michael Saliba, and Lakshminarayana Polavarapu. "Defect Passivation in Lead-Halide Perovskite Nanocrystals and Thin Films: Toward Efficient LEDs and Solar cells." In: *Angewandte Chemie* 60.40 (2021), pp. 21636–21660. DOI: 10.1002/anie.202102360 (cited on page 28).

[67] Roger J. Elliott. "Intensity of optical absorption by excitons." In: *Physical Review* 108.6 (1957), p. 1384. DOI: 10.1103/PhysRev.108.1384 (cited on page 29).

[68] Ali Naeem, Francesco Masia, Sotirios Christodoulou, Iwan Moreels, Paola Borri, and Wolfgang Langbein. "Giant exciton oscillator strength and radiatively limited dephasing in two-dimensional platelets." In: *Physical Review B* 91.12 (2015), p. 121302. DOI: 10.1103/PhysRevB.91.121302 (cited on page 29).

[69] Justinas Butkus, Parth Vashishtha, Kai Chen, Joseph K. Gallaher, Shyamal KK Prasad, Dani Z. Metin, Geoffry Laufersky, Nicola Gaston, Jonathan E. Halpert, and Justin M. Hodgkiss. "The evolution of quantum confinement in $CsPbBr_3$ perovskite nanocrystals." In: *Chemistry of Materials* 29.8 (2017), pp. 3644–3652. DOI: 10.1021/acs.chemmater.7b00478 (cited on page 30).

[70] Verena A. Hintermayr, Lakshminarayana Polavarapu, Alexander S. Urban, and Jochen Feldmann. "Accelerated carrier relaxation through reduced coulomb screening in two-dimensional halide perovskite nanoplatelets." In: *ACS Nano* 12.10 (2018), pp. 10151–10158. DOI: 10.1021/acsnano.8b05029 (cited on pages 30, 58, 81, 84).

[71] J. Feldmann, G. Peter, E.O. Göbel, P. Dawson, K. Moore, C. Foxon, and R.J. Elliott. "Linewidth dependence of radiative exciton lifetimes in quantum wells." In: *Physical Review Letters* 59.20 (1987), p. 2337. DOI: 10.1103/PhysRevLett.59.2337 (cited on pages 30, 66, 94).

[72] Thomas Morgenstern, Carola Lampe, Tassilo Naujoks, Matthew Jurow, Yi Liu, Alexander S. Urban, and Wolfgang Brütting. "Elucidating the performance limits of perovskite nanocrystal light emitting diodes." In: *Journal of Luminescence* 220 (2020), p. 116939. DOI: 10.1016/j.jlumin.2019.116939 (cited on pages 32, 35).

[73] Verena A. Hintermayr, Carola Lampe, Maximilian Löw, Janina Roemer, Willem Vanderlinden, Moritz Gramlich, Anton X. Böhm, Cornelia Sattler, Bert Nickel, Theobald Lohmüller, and Alexander S. Urban. "Polymer nanoreactors shield perovskite nanocrystals from degradation." In: *Nano Letters* 19.8 (2019), pp. 4928–4933. DOI: 10.1021/acs.nanolett.9b00982 (cited on pages 32, 96).

[74] Franziska Krieg, Stefan T. Ochsenbein, Sergii Yakunin, Stephanie Ten Brinck, Philipp Aellen, Adrian Süess, Baptiste Clerc, Dominic Guggisberg, Olga Nazarenko, Yevhen Shynkarenko, Sudhir Kumar, Chih-Jen Shih, Ivan Infante, and Maksym V. Kovalenko. "Colloidal $CsPbX_3$ (X= Cl, Br, I) nanocrystals 2.0: Zwitterionic capping ligands for improved durability and stability." In: *ACS Energy Letters* 3.3 (2018), pp. 641–646. DOI: 10.1021/acsenergylett.8b00035 (cited on page 32).

[75] Yu Tong, Eva Bladt, Meltem F. Aygüler, Aurora Manzi, Karolina Z. Milowska, Verena A. Hintermayr, Pablo Docampo, Sara Bals, Alexander S. Urban, Lakshminarayana Polavarapu, and Jochen Feldmann. "Highly luminescent cesium lead halide perovskite nanocrystals with tunable composition and thickness by ultrasonication." In: *Angewandte Chemie* 55.44 (2016), pp. 13887–13892. DOI: 10.1002/anie.201605909 (cited on page 35).

[76] Jonathan Mooney and Patanjali Kambhampati. "Get the basics right: Jacobian conversion of wavelength and energy scales for quantitative analysis of emission spectra." In: *The Journal of Physical Chemistry Letters* 4.19 (2013), pp. 3316–3318. DOI: 10.1021/jz401508t (cited on page 41).

[77] Moritz Gramlich, Michael W. Swift, Carola Lampe, John L. Lyons, Markus Döblinger, Alexander L. Efros, Peter C. Sercel, and Alexander S. Urban. "Dark and Bright Excitons in Halide Perovskite Nanoplatelets." In: *Advanced Science* 9.5 (2022), p. 2103013. DOI: 10.1002/advs.202103013 (cited on pages 47, 51–53, 63).

[78] Alexander L. Efros. "Luminescence polarization of CdSe microcrystals." In: *Physical Review B* 46.12 (1992), p. 7448. DOI: 10.1103/PhysRevB.46.7448 (cited on pages 50, 58).

[79] Gilbert N. Lewis and M. Kasha. "Phosphorescence and the triplet state." In: *Journal of the American Chemical Society* 66.12 (1944), pp. 2100–2116. DOI: 10.1021/ja01240a030 (cited on page 50).

[80] Peter C. Sercel, John L. Lyons, Darshana Wickramaratne, Roman Vaxenburg, Noam Bernstein, and Alexander L. Efros. "Exciton fine structure in perovskite nanocrystals." In: *Nano Letters* 19.6 (2019), pp. 4068–4077. DOI: 10.1021/acs.nanolett.9b01467 (cited on pages 50, 51, 53).

[81] Elena V. Shornikova, Louis Biadala, Dmitri R. Yakovlev, Victor F. Sapega, Yuri G. Kusrayev, Anatolie A. Mitioglu, Mariana V. Ballottin, Peter C.M. Christianen, Vasilii V. Belykh, Mikhail V. Kochiev, Nikolai N. Sibeldin, Aleksandr A. Golovatenko, Anna V. Rodina, Nikolay A. Gippius, Alexis Kuntzmann, Ye Jiang, Michel Nasilowski, Benoit Dubertret, and Manfred Bayer. "Addressing the exciton fine structure in colloidal nanocrystals: the case of CdSe nanoplatelets." In: *Nanoscale* 10.2 (2018), pp. 646–656. DOI: 10.1039/C7NR07206F (cited on pages 50, 57, 61, 62).

[82] Natalia S. Rytova. "Screened potential of a point charge in a thin film." In: *Vestnik of Moskow University / arXiv:1806.00976* (1967) (cited on page 51).

[83] Leonid V. Keldysh. "Coulomb interaction in thin semiconductor and semimetal films." In: *Soviet Journal of Experimental and Theoretical Physics Letters* 29 (1979), p. 658 (cited on page 51).

[84] Yasushi Nagamune, Shojiro Takeyama, and Noboru Miura. "Exciton spectra and anisotropic Zeeman effect in PbI 2 at high magnetic fields up to 40 T." In: *Physical Review B* 43.15 (1991), p. 12401. DOI: 10.1103/PhysRevB.43.12401 (cited on page 51).

[85] Peter C. Sercel, Zeev Valy Vardeny, and Alexander L. Efros. "Circular dichroism in non-chiral metal halide perovskites." In: *Nanoscale* 12.35 (2020), pp. 18067–18078. DOI: 10.1039/D0NR05232A (cited on page 52).

[86] Vasilii V. Belykh, Dmitri R. Yakovlev, Mikhail M. Glazov, Philipp S. Grigoryev, Mujtaba Hussain, Janina Rautert, Dmitry N. Dirin, Maksym V. Kovalenko, and Manfred Bayer. "Coherent spin dynamics of electrons and holes in $CsPbBr_3$ perovskite crystals." In: *Nature Communications* 10.1 (2019), pp. 1–6. DOI: 10.1038/s41467-019-08625-z (cited on page 53).

[87] Peter C. Sercel, John L. Lyons, Noam Bernstein, and Alexander L. Efros. "Quasicubic model for metal halide perovskite nanocrystals." In: *The Journal of Chemical Physics* 151.23 (2019), p. 234106. DOI: 10.1063/1.5127528 (cited on page 53).

[88] Zhuo Yang, Alessandro Surrente, Krzysztof Galkowski, Atsuhiko Miyata, Oliver Portugall, Rebecca J. Sutton, Amir A. Haghighirad, Henry J. Snaith, Duncan K. Maude, Paulina Plochocka, and Robin J. Nicholas. "Impact of the halide cage on the electronic properties of fully inorganic cesium lead halide perovskites." In: *ACS Energy Letters* 2.7 (2017), pp. 1621–1627. DOI: 10.1021/acsenergylett.7b00416 (cited on page 53).

[89] John R. Rumble. *Physical Constants of Organic Compounds, in CRC handbook of chemistry and physics*. CRC Press, 2017 (cited on page 53).

[90] Rim Ben Aich, Samia Ben Radhia, Kais Boujdaria, Maria A. Chamarro, and Christophe Testelin. "Multiband k· p model for tetragonal crystals: application to hybrid halide perovskite nanocrystals." In: *The Journal of Physical Chemistry Letters* 11.3 (2020), pp. 808–817. DOI: 10.1021/acs.jpclett.9b02179 (cited on page 53).

[91] Watcharaphol Paritmongkol, Eric R. Powers, Nabeel S. Dahod, and William A. Tisdale. "Two origins of broadband emission in multilayered 2D lead iodide perovskites." In: *The Journal of Physical Chemistry Letters* 11.20 (2020), pp. 8565–8572. DOI: 10.1021/acs.jpclett.0c02214 (cited on pages 60, 61, 72, 75).

[92] Louis Biadala, Yann Louyer, Philippe Tamarat, and Brahim Lounis. "Direct observation of the two lowest exciton zero-phonon lines in single CdSe/ZnS nanocrystals." In: *Physical Review Letters* 103.3 (2009), p. 037404. DOI: 10.1103/PhysRevLett.103.037404 (cited on pages 61, 62).

[93] Andreas Singldinger, Moritz Gramlich, Christoph Gruber, Carola Lampe, and Alexander S. Urban. "Nonradiative energy transfer between thickness-controlled halide perovskite nanoplatelets." In: *ACS Energy Letters* 5.5 (2020), pp. 1380–1385. DOI: 10.1021/acsenergylett.0c00471 (cited on pages 66, 89).

[94] Moritz Gramlich, Carola Lampe, Jan Drewniok, and Alexander S. Urban. "How Exciton–Phonon Coupling Impacts Photoluminescence in Halide Perovskite Nanoplatelets." In: *The Journal of Physical Chemistry Letters* 12.46 (2021), pp. 11371–11377. DOI: 10.1021/acs.jpclett.1c03437 (cited on page 69).

[95] Adam D. Wright, Carla Verdi, Rebecca L. Milot, Giles E. Eperon, Miguel A. Pérez-Osorio, Henry J. Snaith, Feliciano Giustino, Michael B. Johnston, and Laura M. Herz. "Electron-phonon coupling in hybrid lead halide perovskites." In: *Nature Communications* 7.1 (2016), pp. 1–9. DOI: 10.1038/ncomms11755 (cited on pages 72, 73).

[96] Oscar Hsu-Cheng Cheng, Tian Qiao, Matthew Sheldon, and Dong Hee Son. "Size-and temperature-dependent photoluminescence spectra of strongly confined $CsPbBr_3$ quantum dots." In: *Nanoscale* 12.24 (2020), pp. 13113–13118. DOI: 10.1039/D0NR02711A (cited on pages 72, 73).

[97] Rinku Saran, Amelie Heuer-Jungemann, Antonios G. Kanaras, and Richard J. Curry. "Giant bandgap renormalization and exciton–phonon scattering in perovskite nanocrystals." In: *Advanced Optical Materials* 5.17 (2017), p. 1700231. DOI: 10.1002/adom.201700231 (cited on page 72).

[98] Kewei Wu, Ashok Bera, Chun Ma, Yuanmin Du, Yang Yang, Liang Li, and Tom Wu. "Temperature-dependent excitonic photoluminescence of hybrid organometal halide perovskite films." In: *Physical Chemistry Chemical Physics* 16.41 (2014), pp. 22476–22481. DOI: 10.1039/C4CP03573A (cited on page 72).

[99] Limeng Ni, Uyen Huynh, Alexandre Cheminal, Tudor H. Thomas, Ravichandran Shivanna, Ture F. Hinrichsen, Shahab Ahmad, Aditya Sadhanala, and Akshay Rao. "Real-time observation of exciton-phonon coupling dynamics in self-assembled hybrid perovskite quantum wells." In: *ACS Nano* 11.11 (2017), pp. 10834–10843. DOI: 10.1021/acsnano.7b03984 (cited on page 72).

[100] Benjamin T. Diroll, Hua Zhou, and Richard D. Schaller. "Low-temperature absorption, photoluminescence, and lifetime of $CsPbX_3$ (X= Cl, Br, I) nanocrystals." In: *Advanced Functional Materials* 28.30 (2018), p. 1800945. DOI: 10.1002/adfm.201800945 (cited on page 73).

[101] Jayprakash Bhosale, Anant K. Ramdas, Arnold Burger, Alfonso Muñoz, Aldo H. Romero, Manuel Cardona, Rudolf Lauck, and Reinhard K. Kremer. "Temperature dependence of band gaps in semiconductors: Electron-phonon interaction." In: *Physical Review B* 86.19 (2012), p. 195208. DOI: 10.1103/PhysRevB.86.195208 (cited on page 75).

[102] Chonglong Yu, Zhuo Chen, Jian J. Wang, William Pfenninger, Nemanja Vockic, John T. Kenney, and Kai Shum. "Temperature dependence of the band gap of perovskite semiconductor compound $CsSnI_3$." In: *Journal of Applied Physics* 110.6 (2011), p. 063526. DOI: 10.1063/1.3638699 (cited on page 75).

[103] Ke Wei, Zhongjie Xu, Runze Chen, Xin Zheng, Xiangai Cheng, and Tian Jiang. "Temperature-dependent excitonic photoluminescence excited by two-photon absorption in perovskite $CsPbBr_3$ quantum dots." In: *Optics Letters* 41.16 (2016), pp. 3821–3824. DOI: 10.1364/OL.41.003821 (cited on page 75).

[104] Shuai Wang, Jiaqi Ma, Wancai Li, Jun Wang, Haizhen Wang, Hongzhi Shen, Junze Li, Jiaqi Wang, Hongmei Luo, and Dehui Li. "Temperature-dependent band gap in two-dimensional perovskites: Thermal expansion interaction and electron–phonon interaction." In: *The Journal of Physical Chemistry Letters* 10.10 (2019), pp. 2546–2553. DOI: 10.1021/acsnano.7b03984 (cited on page 75).

[105] Moritz Gramlich, Bernhard J. Bohn, Yu Tong, Lakshminarayana Polavarapu, Jochen Feldmann, and Alexander S. Urban. "Thickness-dependence of exciton–exciton annihilation in halide perovskite nanoplatelets." In: *The Journal of Physical Chemistry Letters* 11.13 (2020), pp. 5361–5366. DOI: 10.1021/acs.jpclett.0c01291 (cited on page 79).

[106] Aydan Yeltik, Savas Delikanli, Murat Olutas, Yusuf Kelestemur, Burak Guzelturk, and Hilmi V. Demir. "Experimental determination of the absorption cross-section and molar extinction coefficient of colloidal CdSe nanoplatelets." In: *The Journal of Physical Chemistry C* 119.47 (2015), pp. 26768–26775. DOI: 10.1021/acs.jpcc.5b09275 (cited on page 84).

[107] Richard D. Schaller and Victor I. Klimov. "High efficiency carrier multiplication in PbSe nanocrystals: implications for solar energy conversion." In: *Physical Review Letters* 92.18 (2004), p. 186601. DOI: 10.1103/PhysRevLett.92.186601 (cited on page 86).

[108] Yulu Li, Tao Ding, Xiao Luo, Zongwei Chen, Xue Liu, Xin Lu, and Kaifeng Wu. "Biexciton Auger recombination in mono-dispersed, quantum-confined CsPbBr3 perovskite nanocrystals obeys universal volume-scaling." In: *Nano Research* 12.3 (2019), pp. 619–623. DOI: 10.1007/s12274-018-2266-7 (cited on page 86).

[109] Juan A. Castaneda, Gabriel Nagamine, Emre Yassitepe, Luiz G. Bonato, Oleksandr Voznyy, Sjoerd Hoogland, Ana F. Nogueira, Edward H. Sargent, Carlos H. Brito Cruz, and Lazaro A. Padilha. "Efficient biexciton interaction in perovskite quantum dots under weak and strong confinement." In: *ACS Nano* 10.9 (2016), pp. 8603–8609. DOI: 10.1021/acsnano.6b03908 (cited on page 86).

[110] Giles E. Eperon, Erin Jedlicka, and David S. Ginger. "Biexciton Auger recombination differs in hybrid and inorganic halide perovskite quantum dots." In: *The Journal of Physical Chemistry Letters* 9.1 (2018), pp. 104–109. DOI: 10.1021/acs.jpclett.7b02805 (cited on page 86).

[111] Qiuyang Li and Tianquan Lian. "Area-and thickness-dependent biexciton Auger recombination in colloidal CdSe nanoplatelets: breaking the "Universal Volume Scaling Law"." In: *Nano Letters* 17.5 (2017), pp. 3152–3158. DOI: 10.1021/acs.nanolett.7b00587 (cited on page 87).

[112] John P. Philbin and Eran Rabani. "Electron–hole correlations govern Auger recombination in nanostructures." In: *Nano Letters* 18.12 (2018), pp. 7889–7895. DOI: 10.1021/acs.nanolett.8b03715 (cited on page 87).

[113] Qiuyang Li, Yawei Yang, Wenxiu Que, and Tianquan Lian. "Size- and morphology-dependent Auger recombination in $CsPbBr_3$ perovskite two-dimensional nanoplatelets and one-dimensional nanorods." In: *Nano Letters* 19.8 (2019), pp. 5620–5627. DOI: 10.1021/acs.nanolett.9b02145 (cited on page 88).

[114] Burak Guzelturk, Murat Olutas, Savas Delikanli, Yusuf Kelestemur, Onur Erdem, and Hilmi Volkan Demir. "Nonradiative energy transfer in colloidal CdSe nanoplatelet films." In: *Nanoscale* 7.6 (2015), pp. 2545–2551. DOI: 10.1039/C4NR06003B (cited on page 95).

[115] Clare E. Rowland, Igor Fedin, Hui Zhang, Stephen K. Gray, Alexander O. Govorov, Dmitri V. Talapin, and Richard D. Schaller. "Picosecond energy transfer and multiexciton transfer outpaces Auger recombination in binary CdSe nanoplatelet solids." In: *Nature Materials* 14.5 (2015), pp. 484–489. DOI: 10.1038/nmat4231 (cited on page 95).

[116] Francisco Palazon, Quinten A. Akkerman, Mirko Prato, and Liberato Manna. "X-ray lithography on perovskite nanocrystals films: from patterning with anion-exchange reactions to enhanced stability in air and water." In: *ACS Nano* 10.1 (2016), pp. 1224–1230. DOI: 10.1021/acsnano.5b06536 (cited on page 96).

[117] Daniel Rossi, Xiaohan Liu, Yangjin Lee, Mohit Khurana, Joseph Puthenpurayil, Kwanpyo Kim, Alexey V. Akimov, Jinwoo Cheon, and Dong Hee Son. "Intense Dark Exciton Emission from Strongly Quantum-Confined $CsPbBr_3$ Nanocrystals." In: *Nano Letters* 20.10 (2020), pp. 7321–7326. DOI: 10.1021/acs.nanolett.0c02714 (cited on page 100).

List of Figures

2.1 Cubic Crystal . . . 4
2.2 Brillouin zone . . . 5
2.3 Band Gap . . . 6
2.4 Wannier-Mott Exciton . . . 8
2.5 Confined Exciton . . . 11
2.6 Density of States . . . 11
2.7 Excitonic Absorption . . . 14
2.8 Inter- and Intraband Processes . . . 14
2.9 Carrier Cooling . . . 15
2.10 Radiative Recombination . . . 16
2.11 Trap-Assisted Recombination . . . 18
2.12 Auger Recombination . . . 19
2.13 Exciton-Exciton Annihilation . . . 19
2.14 Poisson Statistics . . . 20
2.15 Phonon Dispersions . . . 22
2.16 Perovskite Crystal Structure . . . 24
2.17 Band Structure $MAPbI_3$ . . . 25
2.18 Thickness-Tunability of Nanoplatelets . . . 28
2.19 Photoluminescence of $Cs_{n-1}Pb_nBr_{3n+1}$ Nanoplatelets . . . 30
2.20 Absorption Spectra of $Cs_{n-1}Pb_nBr_{3n+1}$ Nanoplatelets . . . 31
2.21 Enhancement of the Nanoplatelets . . . 31

3.1 Electron Microscopy Images . . . 36
3.2 Absorption and Photoluminescence of Dispersions . . . 37
3.3 Micro-Photoluminescence Setup . . . 39
3.4 Optical Excitation Pathway . . . 40
3.5 Optical Detection Pathway . . . 41
3.6 Time-Resolved Single Photon Counting . . . 42
3.7 Transient Absorption Spectrometer . . . 44

4.1 Low-Temperature Photoluminescence of 2 ML Nanoplatelets . . . 48
4.2 Double Gaussian Fit . . . 49
4.3 Photoluminescence Spectra and Decay . . . 50
4.4 Important Quantities within the Model . . . 53
4.5 Temperature-Resolved Photoluminescence Spectra . . . 54
4.6 5 ML and 6 ML Photoluminescence Spectra . . . 55
4.7 Thickness-Dependent Spectral Shift . . . 55
4.8 Thickness Dependence of the Exciton Fine Structure Splitting . . . 57
4.9 Time-Resolved Photoluminescence of 4 ML Nanoplatelets . . . 59
4.10 Temperature-Dependent Photoluminescence Decay of all Nanoplatelets . . . 60
4.11 Self Trapped Excitons in 2 ML NPLs . . . 61
4.12 Splitting of the Bright States . . . 62
4.13 Two-Level Model Fits . . . 63
4.14 Three-Level Model Fits . . . 64

4.15 Theoretical Temperature-Resolved Photoluminescence Spectra 65

5.1 Room Temperature and Low-Temperature Photoluminescence Spectra 70
5.2 Thermal Photoluminescence Shift 71
5.3 Thermal Photoluminescence Broadening 71
5.4 Photoluminescence Broadening Contributions at 300 K 72
5.5 Temperature Dependence of Full-Width Half-Maximum 73
5.6 Fröhlich Interaction 74
5.7 Temperature Dependence of Peak Position 75
5.8 3 ML NPLs in Polymer Matrix 76
5.9 Thermal Expansion Interaction and Exciton-Phonon Interaction 77
5.10 Reproducibility of Temperature-Dependent Photoluminescence Spectra 78

6.1 Differential Transmission Spectra 80
6.2 Decay of the Exciton Population 81
6.3 Monomolecular Decay 82
6.4 Determination of $\langle N \rangle$ 83
6.5 Absorption Cross Section 84
6.6 Higher-Order Processes 85
6.7 Decay of an Exciton Pair 86
6.8 Thickness-Dependence of τ_2 87
6.9 Laterally Larger 2 ML Nanoplatelets 87

7.1 Photoluminescence and Absorption Spectra 90
7.2 Absorption Spectra of Mixed Dispersions 91
7.3 Photoluminescence Spectra of Mixed Dispersions 92
7.4 Spectral Filters 93
7.5 Time-Resolved Photoluminescence of Mixed Dispersions 93
7.6 Photoluminescence Spectra of Heterolayers 94
7.7 Time-Resolved Photoluminescence of Heterolayers 95
7.8 Förster Resonance Energy Transfer Rate and Efficiency 96

List of Tables

3.1 Chemicals 34
3.2 Precursor Ratios 35
3.3 Size Analysis 36

4.1 Material Parameters 53
4.2 Temperature Interval of the Photoluminescence Shift 56
4.3 Three-Level Model Fit Parameters 64

List of Abbreviations

A:D	Acceptor to Donor Ratio
BGR	Band Gap Renormalization
CB	Conduction Band
CBM	Conduction Band Minimum
CCD	Charge-Coupled Device
DFT	Density-Functional Theory
DOS	Density of States
DT	Differential Transmission
DTS	Differential Transmission Spectroscopy
EEA	Exciton-Exciton Annihilation
FA	Formamidinium
FRET	Förster Resonance Energy Transfer
FWHM	Full-Width at Half-Maximum)
GIWAXS	Grazing Incidence Wide Angle X-Ray Scattering)
HAADF	High-Angle Annular Dark Field
HE	Heavy Electrons
JDOS	Joint Density of States
LE	Light Electrons
LHP	Lead Halide Perovskite
LO	Longitudinal Optical
LP	Longpass
LR	Long-Range
LT	Longitudinal-Transverse
MA	Methylammonium
ML	Mononlayer
NPL	Nanoplatelet
OD	Optical Density
PL	Photoluminescence
PLQY	Photoluminescence Quantum Yield
SHG	Second Harmonic Generation
SO	Split-Off (band)
SR	Short-Range
SPAD	Single-Photon Avalanche Diode)
STE	Self-Trapped Exciton)
STEM	Scanning Transmission Electron Microscopy)
TAS	Transient Absorption Spectroscopy
TCSPC	Time-Correlated Single Photon Counting
TEM	Transmission Electron Microscopy
TR-PL	Time-Resolved Photoluminescence
UV	Ultraviolet
VB	Valence Band
VBM	Valence Band Maximum

Acknowledgments

Prof. Dr. Alexander Urban, I want to thank you for trusting me with the position as your first PhD student. It is impossible to list all the things I have learned from you. Through your patience and genuine passion for teaching others, you helped me and guided me in so many areas of expertise and I cannot stress enough, how grateful I am for that. Due to the work environment you create, I enjoyed every day in your group. Even non-scientific tasks, from working on the website (and the real logo) to moving to the new building and installing cryostats, were always fun and collaborative efforts. I consider you as a mentor and friend and look forward to many more superbowls and matches in the Allianz Arena together with you.

Nearly equally as important, I want to thank **Carola Lampe**. Without her there would have been not only no samples to measure but also no order in our calendar. For those reasons (especially the samples), this work would not have been possible without her. I further want to thank **Michael Lichtenegger** for the fun atmosphere we had in the office and for his dedication in his position as "Getränkebeauftragter", as the beer fridge was never empty. In addition, I also want to thank **Andreas Singldinger**, one of the few pre-Königinstraße guys. We always had a good time when building the setups from scratch and he is also a fierce competitor in office basketball (not a "ball of shame" candidate). Those three were also invaluable in proof-reading this thesis.

In terms of sample preparation, I also want to thank **Nina Henke**, who like Caro never refused to answer stupid questions about the magic that happens in the chemistry lab. I further want to thank **Ulrich Leo**, in particular for the LAN parties he organized without which this wouldn't be a real physics group. Here, I also want to mention **Stefan Martin**, **Andreas Bornschlegl**, **Michele Greiner**, **Hyowon Jeong**, **Markus Schoger**, **Andreas Rank**, **Juri Crimmann**, **Connor Heimig** and all other group members over the years. All of you contributed to the fun and collaborative work atmosphere which made me come to the office with a smile every day.

A special thanks goes to **Jan Drewniok**. I have never seen someone work so hard, while keeping such a positive attitude. I am sure we will still have a few "Feierabendbiere" in the future.

Moreover, I want to thank my collaborators **Prof. Dr. Alexander Efros**, **Prof. Dr. Peter Sercel**, **Dr. Michael Swift** and **Dr. John Lyons**. Their contribution to the theoretical part of the research in this thesis was crucial.

I further want to thank **Dr. Bernhard Bohn**. I have learned so much from him and probably would not have started this project, if it was not for him encouraging and convincing me (with the help of a burger and a few beers). I am very grateful for that, as I can now say in retrospect that taking on this project was the best decision.

Another person this thesis would not have been possible without is **Sophie**. You always have my back and motivate me and I am so grateful for that. Thanks, for always being there for me.

The same goes for my brother **Basti**, my grandparents, as well as for **Eike** and **Alex "Schelle"**. Without friends and family to share good times after work, everything in life would be much harder and in some ways pointless.

Last but most definitely not least, I want to thank my parents **Doris** and **Günther**. You provided me with everything during my life and I am grateful for it all. I could literally not ask for any better support and this thesis is dedicated to you!